Effects of Finite Orbit Width on Neoclassical Transport in High-Temperature Helical Plasmas

Seikichi Matsuoka

DOCTOR OF PHILOSOPHY

Department of Fusion Science
School of Physical Science
The Graduate University for Advanced Studies

March, 2011

Abstract

Improving confinement of the particle and energy transport is an important task to realize a nuclear fusion reactor in toroidal magnetic devices and a great effort has been devoted theoretically and experimentally to achieve this aim. Neoclassical (NC) transport theory has been studied in detail, since it describes a diffusive transport phenomenon caused by particle collisional interactions in a torus configuration, and thus, determines a irreducible minimum transport level depending on the magnetic geometry. In helical/stellarator devices which have the three-dimensional magnetic structure, neoclassical transport has a character of increasing with $T_{\rm a}^{7/2}$ in low collisionality regime, where $T_{\rm a}$ is the temperature of species a $=$ e, i. In addition to this, the radial electric field ($E_{\rm r}$), which in general reduce both neoclassical and anomalous transport, is determined by the ambipolar condition of neoclassical particle transport in helical devices.

The plasmas of $T_{\rm i} > 5$ keV are successfully obtained in the recent LHD experiments. Neoclassical transport analyses are performed for such plasmas. We confirm that when $T_{\rm i}$ increases, the NC transport flux is reduced by two orders of magnitude compared to that without $E_{\rm r}$ due to the existence of the ambipolar radial electric field. The parameter survey calculations on $T_{\rm i}$ and $n_{\rm e}$ are also carried out to consider the NC transport flux dependence on the plasma parameter. With these calculations, it is shown that NC ion thermal diffusivity is reduced to small level as that of electron even for plasmas with the fusion reactor relevant parameter if $T_{\rm e} \simeq T_{\rm i}$ is numerically retained. It is found that the radial electric field in high $T_{\rm i}$ plasmas with high $T_{\rm e}$ has a significant impact on the reduction of the NC transport. This fact provides us the opportunity to reconsider the NC transport more rigorously in high $T_{\rm e}$ plasmas.

Neoclassical transport in an asymmetric magnetic field has been estimated and calculated by using numerical simulations based on *local* assumptions, which neglect the particle drift, or the deviation from a certain magnetic surface. Although it has been pointed out that the finite orbit width effect for ions plays an important role in neoclas-

sical transport theory in recent studies, it has been considered that such conventional local assumptions have been valid for electrons. This is because the deviation from the magnetic surface on which the electron is located initially has been considered to be small enough. On the other hand, very high T_e plasmas exceeding $T_e \simeq 20$ keV at the plasma core region followed by electron internal transport barrier formation of the steep T_e gradient have been achieved in recent experiments in LHD. These plasmas are called Core Electron-Root Confinement, CERC, since they are accompanied by the formation of the strong positive radial electric field, or the electron root. The high electron temperature makes helically-trapped electrons drift away from the initial magnetic surface. As a result, local assumptions of the neoclassical transport may be broken even for electrons in CERC plasmas.

This effect of electron drift, however, has not been considered seriously so far and it is quite unclear whether the local treatment is valid or not. In this thesis, the electron finite orbit width effect on neoclassical transport is investigated in detail by using non-local δf Monte Carlo simulation code, FORTEC-3D, which is newly extended to apply to electrons in this work. It is found that the electron finite drift makes qualitative difference between the local treatment and the non-local treatment in neoclassical transport calculations.

This thesis is organized as follows. First, we performed NC transport analysis based on the local treatment for high T_i plasmas. With these calculations, the electron-root E_r is obtained in high T_i plasmas numerically considering T_e is high at the same time. This suggests that the non-local electron drift plays an important role in the E_r formation.

Second, FORTEC-3D, which solves the drift kinetic equation without the local assumptions is newly extended to apply to electrons including electron-ion collisions. Precise benchmark calculations are carried out with DCOM/NNW and GSRAKE code, which are both widely used local neoclassical transport simulation codes. By numerical calculations, it is found that the electron ∇B and curvature drifts change the particle and energy flux due to the particle poloidal precession and collisionless detrapping process in high T_e and the low collisionality regime, while results in low T_e and high collisionality regime reproduce the similar transport dependence on E_r obtained by DCOM/NNW and GSRAKE. The changes of NC transport in the low collisionality regime appear as the reduction of the peak value and/or shift of peak position in flux dependence on the radial electric field. Non-local effect is confirmed by fully taking the particle drift and its orbit into account in neoclassical transport calculations by FORTEC-3D.

Third, the extended FORTEC-3D for electrons is applied to a CERC plasma obtained in the LHD experiment. Such non-local electron transport analysis for the LHD experimental discharge is performed for the first time in this study. The radial electric field is analyzed in two ways: (1) the electron particle flux is calculated by FORTEC-3D with the fixed radial electric field for given plasma profiles and the steady state radial electric field is determined so as to satisfy the ambipolar condition of the electron particle flux obtained by FORTEC-3D and the ion particle flux by DCOM/NNW. (2) Time evolution of the radial electric field is followed as an initial value problem with given plasma profiles using ion-particle-flux-radial-electric-field table made by DCOM/NNW. The ambipolar radial electric field is obtained as its steady state solution. This separate procedure for electron and ion is adopted in order to reduce the calculational burden since simultaneously calculating the NC transport for both species waste too much computational resources. It is shown that the resultant E_{r} differs from that obtained by DCOM/NNW in the core region, while it agrees with ion-root E_{r} evaluated by DCOM/NNW in the edge region.

In this study, the importance of the electron finite orbit width effect in determining the neoclassical transport flux and its influence on the radial electric formation in high temperature helical plasmas is investigated by directly the the drift kinetic equation including the finite orbit width effect of electrons. With this approach, we provide a sufficient and reasonable basis on how the electron drift affects the neoclassical transport and the resultant radial electric field. This enables one to analyze the neoclassical transport property with a desirable accuracy, and thus, leads ones to obtain more detailed physical insight to the plasma physics involving the transport and the radial electric field.

Acknowledgement

First of all, I would like to thank Dr. Masayuki Yokoyama, who gave me an opportunity to study plasma physics, with his helpful support throughout my doctor course. Fruitful discussions with him has led me to this work. He has given me freedom to my work and encouraged me all the time.

I also would like to acknowledge Dr. Shinsuke Satake for his valuable suggestion of this study. He has always guided me in many aspects in this work. I have received much inspiration and kind support from him. He is also acknowledged for providing me a numerical code, FORTEC-3D, for the basis of this thesis.

I express my gratitude for Prof. Hideo Sugama to help me understand plasma physics including neoclassical transport theory. A seminar on collisional transport with him has helped me establish a firm foundation for the physical view on the neoclassical transport in plasmas. I also thank Dr. Ryutaro Kanno for his useful discussions and beneficial comments on my work. He has constantly encouraged me during the whole period of my Ph.D course.

I am grateful to Mr. Hisamichi Funaba for his help to analyze the LHD experimental data. The LHD experiment Group is acknowledged for allowing me to use experimental data obtained in the LHD experiments. I wish to thank Dr. Osamu Yamagishi for having the valuable seminar about drift wave turbulence. Dr. Arimitsu Wakasa and Dr. Sadayoshi Murakami in Kyoto Univ. are also acknowledged for providing the numerical results by DCOM/NNW. I thank Prof. Atsushi Fukuyama in Kyoto Univ. for his continuous support to my work. Dr. Gakushi Kawamura, Dr. Akinobu Matsuyama, Dr. Masanori Nunami, Dr. Ryuichi Ishizaki, Dr. Katsuji Ichiguchi, Dr. Ryousuke Seki, Prof. Katsumi Ida, and Dr. Hiromi Takahashi are also acknowledged for their friendliness and advice which gives me a lot of suggestions for my thesis. I also would like to thank Dr. C. D. Beidler for providing me GSRAKE code. Motoki Nakata (Ph.D. candidate), Kunihiro Ogawa (Ph.D. candidate), Kinya Saito, and Akiyoshi Murakami who encourage me all the time in my student time are also acknowledged.

At last, I express my sincere thanks to my parents, family and friends for their kind encouragement and support that help me to complete my work.

"All's well, that ends well"

– William Shakespeare, All's Well that Ends Well

Contents

Chapter 1

Introduction

1.1 Background

Improving the plasma confinement in toroidal magnetic confinement devices is one of the key issue to realize fusion energy, and a great effort theoretically and experimentally has been devoted to achieve this aim. The plasma density, temperature, the confinement time, *etc.* have been increased year by year in many experiments. It is of great importance to study the plasma transport to explore the favorable character/state of the plasma confinement to improve such the plasma parameters.

In plasma confinement devices, rotational transformation of magnetic field is required. This rotational transformation is made of the superposition of the poloidal magnetic field with toroidal (axisymmetric) magnetic field. In tokamaks [1], while the toroidal magnetic field is induced by the external current, the plasma current (the current inside the plasma) is necessary to introduce the poloidal magnetic field and thus the rotational transformation. The plasma current sometimes leads to disruptive phenomena which poses various problems in the plasma stability. On the other hand, in helical and stellarator devices [2], magnetic field, which essentially have the three-dimensional structure, is formed by external coils and thus no plasma current is required to make the rotational transformation, therefore they have advantage in disruption free. This is the favorable character of helical devices considering feasibility of the fusion energy since reactors in the future should be able to operate in the steady state for a long time without a disruptive phenomena induced by any instabilities. The Large Helical Device (LHD) [3] in National Institute for Fusion Science (NIFS) is the largest Helical confinement device based on the Helical concept.

Theoretically, transport phenomena in toroidal magnetic field are usually referred to as classical [4], neoclassical (NC) [5–8] and anomalous transport [9]. Neoclassical transport is caused by collisional processes of charged particles in toroidal magnetic field, thus, it becomes an irreducible minimum for toroidal magnetic confinement devices, while classical one is simply caused by collisions in the straight magnetic field. Anomalous one refers to the turbulent transport. It mainly arises from two kinds of the turbulence existing in plasmas: one is a microscopic turbulence caused by short wave length fluctuations of the density, potential, *etc.* [10], which is described by the gyrokinetic theory [11, 12], and another is the MHD turbulence [13] which is caused by the MHD, or macroscopic, instabilities disturbing the magnetic field structure.

Although an experimental observation of the radial diffusion usually exceeds the neoclassical transport estimation [14, 15], neoclassical transport theory have attracted much attention since many phenomena in plasma transport such as parallel flow/current [16–18] and the radial electric field [19] are well accounted for by the neoclassical transport theory. In addition to this, the neoclassical diffusion increases in proportion to $1/\nu_{\mathrm{a}}$, or $T_{\mathrm{a}}^{7/2}$ in helical plasmas [20, 21], where ν_{a} and T_{a} denote the collision frequency and the temperature of species a. It is also noted that, the radial electric field, E_{r}, which plays an important role in reducing both the neoclassical and anomalous particle/energy flux through its shear [22] and the $\boldsymbol{E} \times \boldsymbol{B}$ drift [23, 24], is determined by the ambipolar condition of the neoclassical particle flux [19, 25, 26].

Neoclassical transport theory is often considered to be well established, however, there exists a large gap between theory and experimental fact. For example, a transitional behavior of E_{r}, which appears following the formation of internal transport barrier in the plasma temperature [15], is one of the remaining problems to be solved. Also the accurate evaluation of the bootstrap current is the most important part to the steady state operation in tokamak plasmas [27, 28]. The flow distribution in plasmas should be determined with taking the neoclassical viscosity into account [29]. Such flow distribution is of importance since the flow relates to the stability [17] and the resultant plasma performance.

Among topics above mentioned, we focus on the radial electric field property and neoclassical transport in this thesis. Since E_{r} in the plasma plays an important role in the formation of the transport barrier in helical plasmas and H-mode in tokamaks [30–32], which are examples of the improved confinement, the evaluation of the radial electric field and understanding its behavior are the key issue in the plasma transport study. Especially in helical devices, E_{r} is determined by the ambipolar condition of

neoclassical particle flux and neoclassical particle flux is influenced by E_r through the $\boldsymbol{E} \times \boldsymbol{B}$ drift which reduces neoclassical transport in many cases. Thus determining the neoclassical transport and radial electric field self-consistently and evaluate the reduction of the neoclassical transport still remain an important part in the plasma transport in helical devices.

1.2 Motivation

To analyze the ambipolar in the high temperature plasmas, we carry out neoclassical calculations based on the conventional method to high T_i plasmas obtained in the LHD experiments, which is discussed in more detail in Chapter 3. It aims to investigate more favorable way to improve the plasma performance in LHD. There, we perform parameter survey calculations on T_e, T_i, and n_e. As a result, high T_e, namely $T_e \simeq T_i$, is preferable in order to realize the electron-root (large positive) radial electric field which makes ,in general, the transport smaller than the ion-root (weak negative) one [33, 34].

This fact that high T_e plays an important role to accomplish the improved confinement even in high T_i plasmas leads us to draw an attention to high T_e plasmas in LHD experiments called *core electron-root confinement* (CERC) [15, 23, 35, 36]. The characteristics of typical CERC plasmas are as follows. High T_e with the steep T_e gradient called electron internal transport barrier (eITB) are observed in the plasma core region. It is accompanied by the transitional behavior of E_r from the ion-root to the electron-root radial electric field at a radial position of the formation of the transport barrier [15, 37], which results in the large shear of E_r there. It is worth considering whether the conventional neoclassical transport theory is applicable for high T_e plasmas such as CERC. This is described in detail below in this section. It is noted that the transition of E_r itself is an interesting topic since it seems to offer a chance to clarify a bifurcation phenomenon which exists not only in plasma physics but also in the wide range of physics. Although the formation of eITB and its relation to E_r shear have been investigated theoretically and numerically from the point of view of the plasma turbulence [38, 39], an accurate evaluation of the radial electric field from neoclassical transport theory still needs to be done to investigate the physical mechanisms of the E_r transition.

To understand this, it is necessary to reconsider the conventional neoclassical transport analyses especially for electrons because of high T_e and its steep gradient in CERC plasmas. So far, conventional neoclassical transport calculations are based on the local

assumptions which regards the radial deviation of particles from the particular magnetic surface as small enough compared to the scale length [40–43], that is, $\Delta r/L \ll 1$, where Δr denotes the typical radial orbit size of a particle, and L is the typical scale length in the radial direction such as the density gradient, the temperature gradient, the minor radius. It is noted that in the helical magnetic field there are several types of particles due to the three dimensional magnetic field geometry, *e.g.* helically-trapped particles, superbanana particles, passing particles, *etc.* [2, 44] This local assumption enables ones to estimate the neoclassical diffusion of particles and heat from the *local* plasma parameters since plasma particles are assumed not to drift radially so that the collisional processes are not also influenced by the parameters in radially different magnetic surfaces. In remainder of this thesis, we call this treatment *local*, or *conventional* neoclassical theory.

In recent years, many authors have made great efforts to evaluate the neoclassical transport including ion finite orbit width (FOW) neglected in the local neoclassical theory [45–48]. It is called *non-local*, or *global* treatment of the neoclassical transport theory since it involves the effect of the particle radial drift. Since ion banana width is much larger than that of electron by $\sqrt{m_\mathrm{i}/m_\mathrm{e}}$, electron finite orbit width effect has been neglected so far even in these works. In other words, it is considered that electrons finite radial drift would not take effect on the transport properties in contrast to ion. However, this may be invalid in high T_e plasmas in helical devices for two reasons below: (1) the radial deviation of helically-trapped electrons, Δh increases in proportion to $T_\mathrm{e}/\nu_\mathrm{ei} \propto T_\mathrm{e}^{5/2}$ [44], thus regarding Δh as small enough may be violated in CERC plasmas (2) the steep gradient of T_e indicates the small L_T, so that $\Delta h/L_\mathrm{T} \ll 1$ may not be applicable, where L_T denotes the scale length of the temperature gradient. Therefore, neoclassical transport simulations including the electron finite orbit width effect is required for the rigorous evaluation of the electron neoclassical transport and the ambipolar E_r in high T_e plasmas and it is also required to investigate whether the electron FOW affect neoclassical transport simulations.

1.3 Overview of this thesis

In neoclassical transport theory, many calculations based on conventional or local assumptions have been performed as mentioned in the previous section, and those calculations have offered theoretical basis on experiments which aims to improve the plasma confinement and obtain high T_i and high T_e plasmas. It is found that high T_e has a

favorable character to realize the improved confinement for high T_i plasmas by electron-root E_r in LHD. As noted before, however, the local neoclassical treatment can become inappropriate in high T_e plasmas, and numerical simulations including the effect of the rigorous particle orbit are required to evaluate the neoclassical particle and energy flux and to investigate physical mechanisms dominated by the neoclassical transport.

The purpose of this thesis is to present the adequate basis for the effect of the electron orbit on the neoclassical transport and the resulting E_r utilizing direct numerical calculations based on the first principle of drift kinetic equation. The effect of the electron finite orbit width on the neoclassical transport in helical devices is also investigated. This enables us to investigate the E_r behavior in more detail and contributes to the understandings of the transport property in helical systems. For this purpose, we extend FORTEC-3D code [45] to be applicable to the electron neoclassical transport. FORTEC-3D code solves drift kinetic equation based on δf Monte-Carlo method [49, 50] with less approximations than conventional neoclassical calculation codes. The feature of FORTEC-3D is as follows. Electron orbits for many marker particles are followed including their exact drift in arbitrary magnetic field in FORTEC-3D. The ambipolar radial electric field can be also self-consistently obtained with the electron neoclassical transport as the solution of an initial value problem with the combination of the ion particle flux data base obtained by other numerical results.

The remainder of this thesis is organized as follows. Drift kinetic equation, which is the basis of NC transport theory for both local and non-local treatment, is described in detail in Chapter 2. Particle orbit in helical devices and the difference between local and non-local approach is also discussed in this chapter. In Chapter 3, high T_i plasmas in LHD are analyzed by GSRAKE code [51, 52], which solves the ripple-averaged drift kinetic equation. It is noted that the non-local term in GSRAKE is turned off in calculations of this theis, thus it can be said that GSRAKE is based on the local assumption. The Neoclassical ambipolar E_r comes to have electron root when T_e is increased artificially as $T_\mathrm{e} \simeq T_\mathrm{i}$ and improved confinement results from the transport suppression by electron-root E_r. These results lead us to investigate the effect of electron drift which increases in high T_e plasmas. In Chapter 4, we extend FORTEC-3D to apply the electron transport. δf Monte-Carlo method, which is used as the numerical scheme to solve drift kinetic equation in FORTEC-3D code is also described in this chapter. Benchmark calculations among the extended FORTEC-3D for electrons, GSRAKE, and DCOM/NNW [42, 43] are carried out. It is noted that DCOM/NNW solves drift kinetic equation by δf Monte-Carlo method using mono-energy particles based on the

local assumptions. The results of FORTEC-3D calculation for low temperature case, which is the case that the electron FOW effect less affects the electron neoclassical transport because of the small orbit size, show a good agreement with both GSRAKE and DCOM/NNW, that is, a similar curve of E_{r} dependence for electron particle flux as those by GSRAKE and DCOM/NNW are properly reproduced for this case. On the other hand, for low collisional plasmas, qualitative difference between local and non-local treatment arises. It is shown with detailed discussion that this results from the electron radial drift and its finite orbit width effect. Chapter 5 is devoted to the application of new FORTEC-3D for electrons to analyze E_{r} for LHD experimental plasmas. It includes the analyses of both steady state E_{r} and time-dependent one. In Chapter 6, concluding remarks and the future direction of this work are presented. Summary is followed in this chapter.

Chapter 2

Drift Kinetic Equation and Neoclassical Transport

2.1 Drift kinetic equation

Neoclassical transport theory has been established based on drift kinetic equation [5,8, 53]. It involves the averaging procedure over fast gyro motion of plasma particles and removes gyro-angle dependence from a particle distribution function $f_{\rm a}(\boldsymbol{r}, \boldsymbol{v}, t)$, where $\boldsymbol{r}$ and $\boldsymbol{v}$ denotes a-th particle's position and velocity, respectively. The kinetic equation is usually written using the guiding-center variables $(\boldsymbol{R}, \mathcal{E}, \mu, \theta)$ instead of the phase space coordinates of a real particle $(\boldsymbol{r}, \boldsymbol{v})$ as

$$\frac{\partial f_{\rm a}}{\partial t} + \dot{\boldsymbol{R}} \cdot \nabla f_{\rm a} + \dot{\mathcal{E}} \frac{\partial f_{\rm a}}{\partial \mathcal{E}} + \dot{\mu} \frac{\partial f_{\rm a}}{\partial \mu} + \dot{\theta} \frac{\partial f_{\rm a}}{\partial \theta} = C_{\rm a}(f_{\rm a}), \tag{2.1}$$

where $C_{\rm a}(f_{\rm a}) \equiv \sum_{\rm b} C_{\rm ab}(f_{\rm a}, f_{\rm b})$ denotes a collision operator for $f_{\rm a}$ and $f_{\rm a} = f_{\rm a}(\boldsymbol{R}, \mathcal{E}, \mu, \theta, t)$ is the distribution function represented in the guiding-center coordinates. It is noted that μ denotes the magnetic moment, $\mu \equiv m_{\rm a} v_\perp^2 / 2B$, the term proportional to $\dot{\theta}$ describes the gyro motion of particles and $\mathcal{E}$ is the energy defined as

$$\mathcal{E} \equiv \frac{m_{\rm a} v^2}{2} + Z_{\rm a} e \Phi. \tag{2.2}$$

To remove the gyro-angle dependence from the kinetic equation, the small parameter $\delta \equiv \rho_{\rm a}/L \ll 1$ is introduced, where L denotes the scale length characterizing the plasma and the thermal gyroradius $\rho_{\rm a}$ and gyrofrequency $\Omega_{\rm a}$ defined as

$$\rho_{\rm a} \equiv \frac{v_{\rm th,a}}{\Omega_{\rm a}} = \frac{m_{\rm a} v_{\rm th,a}}{e_{\rm a} B} \tag{2.3}$$

$$\Omega{\rm a} \equiv \frac{e_{\rm a} B}{m_{\rm a}} \tag{2.4}$$

are used. Eq. (2.1) is averaged over gyro-angle and only the terms concerning the guiding-center variables only remain. As a result, the drift kinetic equation is thus derived as follows,

$$\frac{\partial \bar{f}_{\rm a}}{\partial t} + \boldsymbol{v}_{\rm gc} \cdot \nabla \bar{f}_{\rm a} + \dot{\mathcal{E}} \frac{\partial \bar{f}_{\rm a}}{\partial \mathcal{E}} = \overline{C_{\rm a}(f_{\rm a})}, \tag{2.5}$$

where we assumes the magnetic moment is conserved, or $\dot{\mu} = 0$ and the overbar refers to the gyro-angle average. $\boldsymbol{v}_{\rm gc}$ is the guiding center drift velocity given by

$$\begin{aligned} \boldsymbol{v}_{\rm gc} &= \boldsymbol{b} v_{\parallel} + \boldsymbol{v}_d \\ &= \boldsymbol{b} v_{\parallel} + \boldsymbol{v}_{\rm E} + \boldsymbol{v}_{\nabla B} + \boldsymbol{v}_{\rm curv} \\ &= \boldsymbol{b} v_{\parallel} + \frac{\boldsymbol{E} \times \boldsymbol{B}}{B^2} + \frac{v_{\perp}^2}{2\Omega_{\rm a}} \boldsymbol{b} \times \nabla \ln B + \frac{v_{\parallel}^2}{\Omega_{\rm a}} \boldsymbol{b} \times \boldsymbol{\kappa}, \end{aligned} \tag{2.6}$$

where the third and the forth terms on the right-hand side in Eq. (2.6) correspond to the ∇B and the curvature drift velocities, respectively with the curvature $\boldsymbol{\kappa}$ defined as

$$\boldsymbol{\kappa} \equiv \boldsymbol{b} \cdot \nabla \boldsymbol{b}. \tag{2.7}$$

Eq. (2.5) is the so-called drift kinetic equation and an alternative form of Eq. (2.5) is obtained by using the kinetic energy $K \equiv \frac{m_{\rm a} v^2}{2}$ instead of the energy $\mathcal{E}$ for the later use as

$$\frac{\partial f}{\partial t} + \boldsymbol{v}_{\rm gc} \cdot \nabla f + \dot{K} \frac{\partial f}{\partial K} = C(f), \tag{2.8}$$

where we have omitted the overbar and subscript a for simplicity.

2.2 Local and non-local approach in neoclassical transport theory

The neoclassical transport coefficients are calculated from the steady-state solution of the drift kinetic equation (2.8). The guiding-center coordinates used in Eq. (2.8) is usually written in Boozer coordinates (Ψ, θ, ζ) [54] since the strength of the magnetic field is only required for the drift equation of motion for each particles, where Ψ denotes the label magnetic surface (usually the toroidal magnetic flux in asymmetric toroidal plasmas such as LHD), θ the poloidal angle, and ζ the toroidal angle, respectively. This choice of Boozer coordinates enables one to easily solve the drift kinetic equation. In Boozer coordinates, the magnetic field is written as,

$$\boldsymbol{B} = \nabla \Psi \times \theta + \iota \nabla \zeta \times \Psi. \tag{2.9}$$

To solve the equation, the distribution function f is assumed to be described as the linear combination of a local Maxwellian part and the remainder, $f = f_{\rm M} + \delta f$, where

$$f_{\rm M} = n(\Psi)\left(\frac{m}{2\pi T(\Psi)}\right)^{3/2}\exp\left(-\frac{mv^2}{2T(\Psi)}\right). \tag{2.10}$$

We assume that the plasma density and the temperature depend only on the magnetic surface Ψ, that is, $n = n(\Psi)$ and $T = T(\Psi)$. For simplicity we consider that the plasma has no mean flow velocity $\boldsymbol{V} = 0$. Substituting above expression of the distribution function into Eq. (2.8), one can obtain the following equation to the leading order as

$$\boldsymbol{b}v_{\parallel}\cdot\nabla f_{\rm M} = C(f_{\rm M}). \tag{2.11}$$

It is immediately found that the Maxwellian distribution function $f_{\rm M}$ is the solution of the leading order equation of Eq. (2.11). Then to the first order of $\mathrm{O}(\delta)$, one obtains

$$\frac{\partial\delta f}{\partial t} + \boldsymbol{b}v_{\parallel}\cdot\nabla\delta f + \dot{K}\frac{\partial\delta f}{\partial K} = \boldsymbol{v}_{\rm d}\cdot\nabla f_{\rm M} + \dot{K}\frac{\partial f_{\rm M}}{\partial K} + C(\delta f). \tag{2.12}$$

Solving the equation (2.12) to obtain δf, and then calculating the neoclassical particle and energy flux as

$$\boldsymbol{\Gamma}(\Psi) \equiv \langle\int \boldsymbol{v}\delta f d^3v,\rangle \tag{2.13}$$

$$\boldsymbol{Q}(\Psi) \equiv \langle\int \frac{mv^2}{2}\boldsymbol{v}\delta f d^3\rangle \tag{2.14}$$

is the main concern in neoclassical transport theory, where $\langle\cdot\rangle$ denotes the flux surface average defined as

$$\langle A\rangle \equiv \int d\theta d\zeta\sqrt{g_{\rm B}}A/\int d\theta d\zeta\sqrt{g_{\rm B}}. \tag{2.15}$$

In the definition above we use the Jacobian of Boozer coordinates, $\sqrt{g_{\rm B}}$.

2.2.1 Finite orbit width effect

Solving Eq. (2.12) analytically for an arbitrary three-dimensional magnetic field is difficult task. Therefore, δf and resultant neoclassical transport are usually calculated numerically especially for helical/stellarator devices. To implement calculations, δf Monte-Carlo method [49,50] has been widely used as an efficient tool. δf Monte-Carlo method of evaluating the transport coefficients such as the diffusion coefficient and the thermal diffusivity needs to solve the particle drift motion. Before We discuss the formalism of δf Monte-Carlo method in detail in Chapter 4, the drift equation of

motion for particles in Boozer coordinates [55–58] is described in the present subsection. Also in this subsection, we discuss the finite orbit width of particles, which is the main concern in this thesis.

We first introduce the guiding-center Hamiltonian as follows;

$$H(\theta, \zeta, p_\theta, p_\zeta, t) = \frac{m v_\parallel^2}{2} + \mu B + e_{\rm a}\Phi(\Psi), \tag{2.16}$$

where, the electrostatic potential depending only on the magnetic surface is assumed. In the guiding-center Hamiltonian representation above, p_θ and p_ζ denote the canonical momenta conjugate to θ and ζ, represented as

$$p_\theta = m\frac{I v_\parallel}{B} + e\Psi \tag{2.17}$$

$$p_\zeta = = m\frac{g v_\parallel}{B} + e\chi. \tag{2.18}$$

Here, $\chi = \chi(\Psi)$ denotes the poloidal magnetic flux and $g(\Psi) = B_\zeta$ and $I(\Psi) = B_\theta$ correspond to the poloidal and the toroidal current, respectively. Using the guiding-center Hamiltonian (2.16), one can obtain following Hamilton's canonical equations for the guiding-center drift motion:

$$\dot{\theta} = \frac{\partial H}{\partial p_\theta} \tag{2.19}$$

$$\dot{\zeta} = \frac{\partial H}{\partial p_\zeta} \tag{2.20}$$

$$\dot{p_\theta} = -\frac{\partial H}{\partial \theta} \tag{2.21}$$

$$\dot{p_\zeta} = -\frac{\partial H}{\partial \zeta}. \tag{2.22}$$

Here, the phase-space coordinates are chosen as $(\Psi, \theta, \zeta, \rho_\parallel, \mu)$ to obtain the drift equation of motion according to the description in the literature. Noted that $\rho_\parallel$ is defined as $\rho_\parallel \equiv \frac{m v_\parallel}{eB}$. The drift equation of motion in the guiding-center coordinates $(\Psi, \theta, \zeta, \rho_\parallel, \mu)$ is thus derived as

$$\dot{\Psi} = \frac{\delta}{\gamma}\left(I\frac{\partial B}{\partial \zeta} - g\frac{\partial B}{\partial \theta}\right), \tag{2.23}$$

$$\dot{\theta} = \left[\delta\frac{\partial B}{\partial \Psi} + e\frac{d\phi}{d\Psi}\right]\frac{\partial \Psi}{\partial p_\theta} + \frac{e^2B^2}{m}\rho_\parallel\frac{\partial \rho_\parallel}{\partial p_\theta}, \tag{2.24}$$

$$\dot{\zeta} = \left[\delta\frac{\partial B}{\partial \Psi} + e\frac{d\phi}{d\Psi}\right]\frac{\partial \Psi}{\partial p_\zeta} + \frac{e^2B^2}{m}\rho_\parallel\frac{\partial \rho_\parallel}{\partial p_\zeta}, \tag{2.25}$$

$$\dot{\rho_\parallel} = -\frac{\delta}{\gamma}\left[\left(\rho_\parallel\frac{dg}{d\Psi} - \iota\right)\frac{\partial B}{\partial \theta} - \left(\rho_\parallel\frac{dI}{d\Psi} + 1\right)\frac{\partial B}{\partial \zeta}\right], \tag{2.26}$$

$$\dot{\mu} = 0, \tag{2.27}$$

where

$$\gamma \equiv -eI\left(\rho_{\parallel}\frac{dg}{d\Psi}-\iota\right)+eg\left(\rho_{\parallel}\frac{dI}{d\Psi}+1\right) \tag{2.28}$$

$$\delta \equiv \mu+\frac{e^2\rho_{\parallel}^2}{m}B \tag{2.29}$$

have been used. It is noted that δ in this subsection must be distinguished from that used as the small parameter in the preceding description. The derivatives of Ψ and $\rho_{\parallel}$ with respect to the canonical momenta p_θ and p_ζ are derived from the transformation from $(\theta,\zeta,p_\theta,p_\zeta)$ to $(\Psi,\theta,\zeta,\rho_{\parallel})$

$$\frac{\partial\Psi}{\partial p_\theta} = \frac{g}{\gamma}, \tag{2.30}$$

$$\frac{\partial\rho_{\parallel}}{\partial p_\theta} = -\frac{1}{\gamma}\left(\rho_{\parallel}\frac{dg}{d\Psi}-\iota\right), \tag{2.31}$$

$$\frac{\partial\Psi}{\partial p_\zeta} = -\frac{I}{\gamma}, \tag{2.32}$$

$$\frac{\partial\rho_{\parallel}}{\partial p_\zeta} = \frac{1}{\gamma}\left(\rho_{\parallel}\frac{dI}{d\Psi}+1\right). \tag{2.33}$$

The equation for the kinetic energy $K=\frac{e^2B^2}{2m}\rho_{\parallel}^2+\mu B$ is then obtained as,

$$\begin{aligned}\dot{K} &= \frac{e^2B^2}{m}\rho_{\parallel}\dot{\rho}_{\parallel}+\frac{e^2B}{m}\rho_{\parallel}^2B\dot{B}+\dot{\mu}B\\ &= \frac{e^2B^2}{m}\rho_{\parallel}\dot{\rho}_{\parallel}+\left(\mu+\frac{e^2B}{m}\rho_{\parallel}\right)\dot{B}\\ &= \frac{e^2B^2}{m}\rho_{\parallel}\dot{\rho}_{\parallel}+\delta\left(\dot{\boldsymbol{R}}\cdot\nabla\right)B.\end{aligned} \tag{2.34}$$

Thus, the following equation is immediately obtained using Eq. (2.23) - (2.26) as

$$\dot{K}=-e\frac{d\phi}{d\Psi}\dot{\Psi}. \tag{2.35}$$

As described in chapter 1, finite orbit width effects are caused by the deviation of the guiding center from a magnetic flux surface Ψ due to the drift motion. The effects are represented as $\dot{\Psi}$ in the equations of drift motion derived above. Also noted that in the equation of the kinetic energy $\dot{K}$ involves the finite orbit width effect since it includes the term $\dot{\Psi}$. This is clearly understood from the fact that Eq. (2.35) can be rewritten as

$$\dot{K}=e\boldsymbol{v}_{\rm d}\cdot\boldsymbol{E}_{\rm r}. \tag{2.36}$$

Later in this thesis, we calculate the electron neoclassical transport with the finite orbit width effects according to the drift equations of motion shown in this section.

2.2.2 Local treatment

Neoclassical transport has been conventionally calculated assuming that the finite orbit width effect is negligibly small compared to the typical scale length of the plasma. This *local*, or *conventional* neoclassical transport theory has been recognized as the standard procedure for calculating the neoclassical diffusion coefficients.

In the local neoclassical theory, the drift motion of the guiding-center of particles is solely located at a single magnetic surface, that is, the second order term,

$$\dot{\Psi}\frac{\partial \delta f}{\partial \Psi} \tag{2.37}$$

is neglected, but

$$\dot{\Psi}\frac{\partial f_{\mathrm{M}}}{\partial \Psi} \tag{2.38}$$

is kept since it involves the term of order $\mathrm{O}(\delta)$. As a result,

$$\dot{K} \simeq 0. \tag{2.39}$$

is also assumed in the local neoclassical theory. The local treatment has several advantages in the practical numerical calculation of neoclassical diffusion coefficients to reduce the computational resources. It can regard the particle kinetic energy as a numerical parameter since it does not change due to the local assumptions during the calculations.

For example, DCOM/NNW code [42, 43] adopts such local assumptions above. DCOM/NNW calculates the neoclassical diffusion coefficients based on δf Monte-Carlo method. In DCOM/NNW, test particles have the fixed energy and are assumed to localized at their initial magnetic surfaces. Then the diffusion coefficients at each local magnetic surface are evaluated as a function of the kinetic energy used in the calculation. Then, the energy dependent coefficients which are obtained in this way are integrated over the kinetic energy as

$$D_j = \int D(K) K^j \exp(-\frac{K}{T}) dK \tag{2.40}$$

to evaluate the neoclassical diffusion coefficients corresponding to the thermal forces such as ∇n, ∇T, *etc.*. It is noted that $D(K)$ denotes the energy dependent diffusion coefficient and D_j is the neoclassical diffusion coefficient for $j = 1, 2, 3$. If we use only the pitch-angle collision operator as the collision term of drift kinetic equation, there remains only three phase-space variables, namely, $(\theta, \zeta, \xi \equiv \frac{v_{\parallel}}{v})$ instead of the full five-dimensional phase-space of the drift kinetic equation.

GSRAKE [51, 52] is another numerical code of the local neoclassical transport. GSRAKE is based on the ripple-averaged drift kinetic equation and it directly solves the equation. Non-local terms arising from the particle curvature and ∇B drifts are retained in the ripple-averaged drift kinetic equation in GSRAKE. However, since such terms are turned off in calculations in this thesis, GSRAKE is referred to as a local neoclassical transport code here. More detailed discussion on the ripple-averaged drift kinetic equation and GSRAKE is presented in Chapter 3.

The local assumptions discussed above are valid when the particle does not deviate largely from the initial surface. When $\boldsymbol{E} \times \boldsymbol{B}$ drift velocity dominates over other drift velocities such as ∇B and the curvature drifts, this assumption is usually satisfied since $v_{\mathrm{d}} \simeq v_{\boldsymbol{E}\times\boldsymbol{B}}$ and $v_{\boldsymbol{E}\times\boldsymbol{B}}$ is almost in the poloidal direction in many devices. However, it is often broken in both axisymmetric and asymmetric plasmas due to the particles which experience the large drift, such as *potato* particles in tokamaks, and *helically-trapped* particles in helical/stellarator devices. These particles have been considered to be important when calculating neoclassical transport and much efforts have been made to include FOW effect in neoclassical transport calculation in recent years [45–48]. While the finite orbit width effects have been treated exclusively for ion species, those for electron species must be paid attention in asymmetric magnetic field because of the helically-trapped electrons in high T_{e} plasmas as pointed out in Chapter 1.

2.3 Analytical calculation of neoclassical transport

The guiding center orbits in magnetic confinement devices are in general classified into either trapped or untrapped (passing) particles depending on the pitch angle of each particle [59]. The neoclassical transport strongly depends on the guiding center orbits [20], thus it is important to understand the orbits, or the drift motion of the guiding center, in plasmas. The radial electric field also makes influence on the neoclassical transport in helical plasmas. In this section, we briefly review analytical calculations of neoclassical transport in helical plasmas especially in low-collisional regime since we are mainly interested in the neoclassical transport in high temperature plasmas. It enables ones to understand the relation between the neoclassical transport and the particle orbit through the collision frequency, the radial electric field, the poloidal rotation, *etc.*

2.3.1 Guiding center orbit

Plasma particles are basically classified into two classes of particles, namely, trapped and passing particles. In axisymmetric tokamaks trapped ones are known as the banana particles located on the outboard side in the poloidal cross section except at the core region where other trapped states such as potato appear [60]. It is noted that in axisymmetric tokamaks the magnetic field B becomes stronger on the inboard side than in the outboard side due to the toroidicity. This is understood as the magnetic field in axisymmetric tokamaks can be written as $B/B_0 = 1-\epsilon_{\rm t}\cos\theta$, where B_0 denotes some reference strength of the magnetic field and $\epsilon_{\rm t}$ is the toroidicity, respectively. The banana particles are trapped, or reflected at a certain point where a particle with a given kinetic energy K and magnetic moment μ cannot enter a inboard side since the magnetic field is so strong that $\mu B > K$ and thus $v_\parallel^2 = 2(K-\mu B)/m < 0$. Therefore, if K and μ of the particle satisfy the relation of $\mu B_{\rm max} < K$, it moves freely along the field line and is the passing particle. In contrast, if $\mu B_{\rm max} > K$, the particle is referred to as trapped, or banana particle.

In helical devices, the situation is more complex since the magnetic field strength depends not only on the poloidal angle but also the toroidal angle due to the helicity. The magnetic field strength in helical devices can be written as follows,

$$\frac{B}{B_0} = 1 - \epsilon_{\rm t}\cos\theta - \epsilon_{\rm h}\cos(l\theta - N\zeta) \tag{2.41}$$

in the simplest form, where l and N are the number of the pole and helical pitch, respectively, and $\epsilon_{\rm h}$ denotes the helicity. Thus, it can be said that the magnetic field in helical devices is composed of the superposition of the helicity, or the helical ripple in addition to the toroidal field component as shown in Fig.2.1.

In Fig.2.1, typical particles in helical magnetic field are schematically described. The passing particle can travel without trapped any magnetic field along the field line. The trapped particles and are further classified into two different types of particles, that is, blocked one and (helically) trapped one. The former one can pass through one or more helical ripple but are trapped by the magnetic field well of toroidicity. On the other hand, the latter particle is trapped by the single helical ripple, so that they are called helically-, or ripple-trapped particles hereafter.

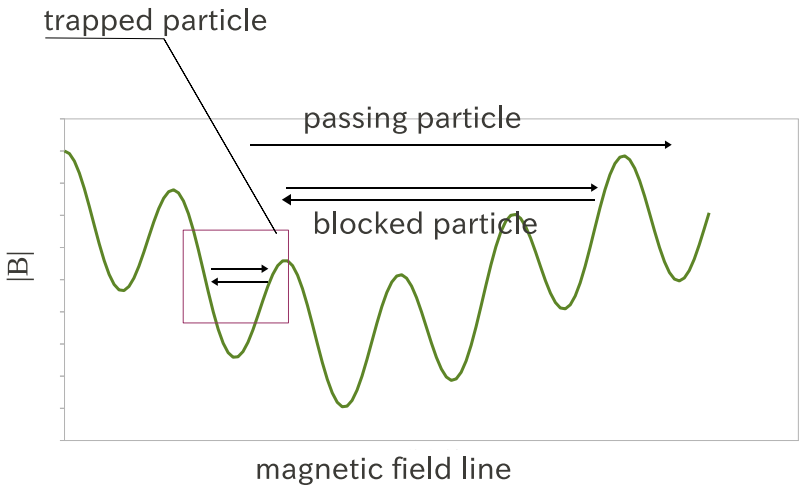

Figure 2.1: Schematic view of typical particles which exist in the helical magnetic field.

2.3.2 Neoclassical transport in helical devices

Neoclassical transport depends on the collision frequency of a plasma since particles change their orbits due to collisions. Here we concentrate on the neoclassical transport in the $1/\nu$ regime since our main concern is the high temperature and the low collisional plasma in the helical magnetic field. In $1/\nu$ regime we are interested in the helically-trapped particle mainly contribute to the collisional diffusion due to its large radial drift. Passing particles have less significant impact on the transport process.

To study the neoclassical transport in the helical magnetic field, the bounce-averaged drift kinetic equation has been widely used [20,61–63]. The drift kinetic equation (2.5) can be further simplified by integrating over the fast motion along the field line. This is valid when the magnetic field line moves mainly in the toroidal direction within one helical period due to the small rotational transform, that is, $N/\iota \gg l$, where ι denotes the rotational transform of the magnetic field. The (toroidal) bounce average is defined as,

$$\langle X \rangle_b \equiv \frac{1}{\tau_\zeta} \oint \frac{d\zeta}{\dot{\zeta}} X, \tag{2.42}$$

for passing particles, and,

$$\langle X \rangle_b \equiv \frac{1}{\tau_\zeta} \int_0^{2\pi/M} \frac{d\zeta}{\dot{\zeta}} X, \tag{2.43}$$

for trapped particles, where X is an arbitrary function and τ_ζ denotes the toroidal bounce time for helically-trapped particles and the transit time to pass a single helical ripple for passing ones. One can omit the toroidal-angle variable from the drift kinetic

equation with the bounce-averaging procedure, thus the bounce-averaged drift kinetic equation only retains the particle motion in the poloidal and the radial direction in the real space.

The first order bounce-averaged drift kinetic equation is given as follows.

$$\dot{\theta}\frac{\partial f_1}{\partial \theta} + \dot{r}\frac{\partial f_{\rm M}}{\partial r} = C(f_1), \tag{2.44}$$

where we use the $(r, \theta, \zeta, \mathcal{E}, \mu)$ coordinates instead of $(\Psi, \theta, \zeta, K, \mu)$ used in Sec. 2.1. It is noted that the collision term in this equation is also bounce-averaged. The bounce-averaged drift velocities of the particles are written as,

$$\dot{r} = r\omega_{\rm t}\sin\theta \tag{2.45}$$

$$\dot{\theta} = \omega_{\rm t}\cos\theta + \omega_{\rm h} + \omega_{\rm E} \tag{2.46}$$

where

$$\omega_{\rm t} = \epsilon_{\rm t}\frac{\mu B_0}{eBr^2} \tag{2.47}$$

$$\omega_{\rm h} = \frac{\partial \epsilon_{\rm h}}{\partial r}\frac{\mu B_0}{eBr}\left(\frac{2E(k)}{K(k)} - 1\right) \tag{2.48}$$

$$\omega_{\rm E} = -\frac{E_{\rm r}}{Br}, \tag{2.49}$$

are used. It is noted that $E_{\rm r}$ denotes the radial electric field, $K(k)$ and $E(k)$ are the complete elliptic integral of the first and the second kind, respectively, and k is the so-called pitch angle parameter defined as,

$$k^2 \equiv \frac{\mathcal{E} - e\Phi - \mu B_0(1 + \epsilon_{\rm t}\cos\theta - \epsilon_{\rm h})}{2\mu B_0 \epsilon_{\rm h}}. \tag{2.50}$$

These drift velocities are formally obtained by considering the second adiabatic invariance, J, and more detailed description is presented in Appendix A. The term denoted by $\omega_{\rm t}$ represents the motion arising from the toroidicity, and $\omega_{\rm h}$ from the helicity, and $\omega_{\rm E}$ from the radial electric field, respectively. In many helical devices, the $\omega_{\rm t}$ term is negligible due to the smallness of the smallness of the toroidicity compared to the helicity. The poloidal rotation, $\dot{\theta}$ vanishes when the term of $\omega_{\rm h}$ and $\omega_{\rm E}$ is balanced, namely, $\omega_{\rm h} = \omega_{\rm E}$ This is called the poloidal resonance [64]. The neoclassical transport increases since helically-trapped particles, which cause the large neoclassical diffusion due to their large radial drift, remain trapped for a long time when it occurs.

Our main concern is to solve the equation (2.44) for helically-trapped particles in the $1/\nu$ regime. If the poloidal rotation is mainly caused by the helicity, we can assume

that $\dot{\theta} \simeq \omega_{\rm h}$. This corresponds to the situation that no radial electric field exists and the toroidicity is smaller than the helicity. In the $1/\nu$ regime, the effective collision frequency is estimated as $\nu_{\rm eff} \simeq \nu/\epsilon_{\rm h}$. In this case, we can reduce the bounce-averaged drift kinetic equation (2.44) to,

$$\omega_{\rm h}\frac{\partial f_1}{\partial \theta} + r\omega_{\rm t}\sin\theta\frac{\partial f_{\rm M}}{\partial r} = -\nu_{\rm eff} f_1. \tag{2.51}$$

Writing $f_1 = f_+\cos\theta + f_-\sin\theta$, one obtains,

$$\begin{aligned} \omega_{\rm h} f_- + \nu_{\rm eff} f_+ &= 0 \\ -\omega_{\rm h} f_+ + \nu_{\rm eff} f_- &= -r\omega_{\rm t}\frac{\partial f_{\rm M}}{\partial r}. \end{aligned}$$

The solution is

$$f_- = -\frac{\nu_{\rm eff}}{\nu_{\rm eff}^2 + \omega_{\rm h}^2} r\omega_{\rm t}\frac{\partial f_{\rm M}}{\partial r}. \tag{2.52}$$

Thus, the particle flux is

$$\begin{aligned} \langle nV_{\rm r}\rangle &= \langle \int \dot{r} f_1 d^3v\rangle \\ &= -\frac{1}{2}\int \frac{\nu_{\rm eff}}{\nu_{\rm eff}^2 + \omega_{\rm h}^2}(r\omega_{\rm t})^2\frac{\partial f_{\rm M}}{\partial r}d^3v. \end{aligned} \tag{2.53}$$

If the effective collision frequency is $\nu_{\rm eff} > \omega_{\rm h}$, $\omega_{\rm h}$ is neglected in Eq. (2.53). Then, the diffusion coefficient in the $1/\nu$ regime becomes

$$D_{\rm h} \simeq \frac{\epsilon_{\rm h}^{3/2}\epsilon_{\rm t}^2}{\nu}\left(\frac{T}{eBr}\right)^2. \tag{2.54}$$

It is noted that we use $d^3v = 2\pi dv_\perp dv_\parallel$ and the parallel velocity for helically-trapped particles is estimated as $v_\parallel \simeq \sqrt{\epsilon_{\rm h}}v_\perp$. It is clearly seen that the diffusion coefficient is in proportion to $T^{7/2}$.

Chapter 3

Local Neoclassical Transport Analysis

3.1 Introduction

The ion transport is one of the the central issues in the plasma transport study since the ion particle and temperature need to be confined for a long time to realize the fusion reactor. The analysis of the ion heat transport in LHD has been recently initiated by using the available measured ion temperature profile [65]. It is considered that the anomalous transport due to the plasma turbulence exceeds the neoclassical one in both tokamak and helical devices. However, the quantitative evaluation of the ion neoclassical transport for experimental plasmas is still important since the neoclassical transport determines the minimum transport in toroidal devices. It is also emphasized that the neoclassical transport increases in the high temperature (low collisional) plasma due to the increase in the transport of helically-trapped particles in helical devices known as the ripple transport (see *e.g.*, [20]).

Determining the radial profile of the radial electric field is one of the principal tasks in the plasma transport study. It has been considered that both the anomalous and neoclassical transport are reduced by the radial electric field through the shear, direction, and the strength of the radial electric field. In axisymmetric devices, the particle flux is so called intrinsic ambipolar, and the radial electric field cannot be determined by the neoclassical transport flux. Fortunately, in helical plasmas, the radial electric field is determined by the ambipolar condition of the neoclassical transport [26]. The neoclassical particle flux of electrons and ions, which are both dependent on the ra-

dial electric field, are balanced in the steady state, that is, $\Gamma_{\rm e}(\rho, E_{\rm r}) = \Gamma_{\rm i}(\rho, E_{\rm r})$ are achieved, where where $\Gamma_{\rm e}$ and $\Gamma_{\rm i}$ are electron and ion particle fluxes, respectively and ρ and $E_{\rm r}$ are the radial position and the radial electric field.

The ambipolar electric field is called the electron root when it has the positive value, while it is called the ion root when the negative value [15,66]. The electron-root $E_{\rm r}$ comes to have the larger $|E_{\rm r}|$ than the ion-root one in many cases, and it results in the larger $\boldsymbol{E} \times \boldsymbol{B}$ drift in the plasma. As a result, the electron-root $E_{\rm r}$ generally reduces the neoclassical transport much more than the ion-root one since the $\boldsymbol{E} \times \boldsymbol{B}$ drift suppresses the radial diffusion of particles. The ambipolar radial electric field can have multiple roots in the steady state for the solution of the ambipolar condition. In that case, it is necessary to solve the time evolution of the radial electric field with the neoclassical transport to determine whether the electron-root or the ion-root is realized. We provide the procedure to solve the time evolution of the radial electric field and indeed calculate the resultant ambipolar $E_{\rm r}$ later in Chapter 5 for such case. In this chapter, however, we only evaluate the steady-state neoclassical transport, thus it is beyond the scope to determine the realizable ambipolar electric field.

In Chapter 2, we have briefly described the neoclassical transport analytically. For the practical evaluation of the neoclassical transport for helical plasmas, a numerical calculation is required due to the complexity of the magnetic field configuration. In this chapter, numerical calculations based on the local assumptions are carried out by using GSRAKE code [51,52]. The local assumptions are conventionally adopted as the basis of the neoclassical transport analysis in the wide range of the plasma transport study. The finite orbit width effect, which is neglected in the neoclassical transport calculations in GSRAKE, is discussed later in Chapter 4 and 5 in detail.

High ion temperature plasmas have been successfully demonstrated in the recent LHD experiments [65]. The power increase of the perpendicular neutral beam injections has mainly contributed to make this realize. The ion temperature have exceeded 5 keV at $n_{\rm e} > 1 \times 10^{19}$ m^{-3} and also achieved 3 keV at $n_{\rm e} > 3 \times 10^{19}$ m^{-3} (see Fig. 3.1). It is noted that the observed plasma parameters shown in this figure are based on experimental results in FY2006. The neoclassical transport analyses have been conducted for these high-$T_{\rm i}$ plasmas. Systematic parameter survey calculations are carried out with numerically varying $T_{\rm i}$, $T_{\rm e}$, and $n_{\rm e}$ based on a particular discharge to investigate the parameter dependence of the neoclassical ion diffusivity in the reactor-relevant plasma parameter.

In Section 3.2, the feature of GSRAKE code is briefly described. GSRAKE is

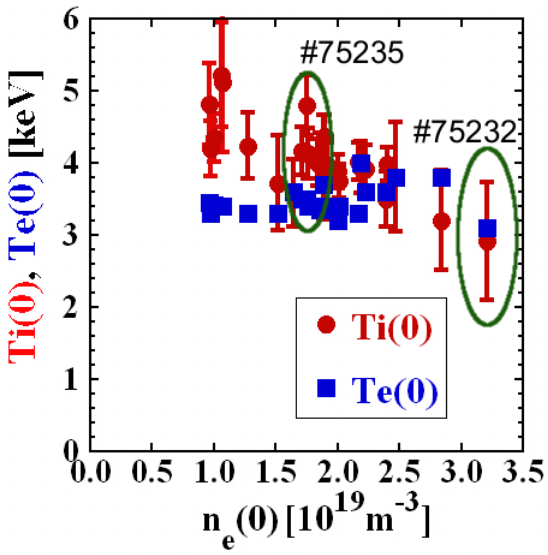

Figure 3.1: The ion and electron temperature with the electron density at the center of the plasma. Those are observed in the high ion temperature experiments in LHD in FY2006.

based on the ripple averaged drift kinetic equation and it has the advantage that it can evaluate the neoclassical transport diffusivity with less computational resources. In Section 3.3, neoclassical transport analyses for the high-$T_{\rm i}$ discharge obtained in the LHD experiments are shown. Numerical results of the parameter survey calculations are described in Sec. 3.4. It aims to examine the neoclassical transport of the plasma in the reactor-relevant regime. It is shown that the neoclassical ion thermal diffusivity is reduced with the existence of the ambipolar $E_{\rm r}$ even for the reactor-relevant parameters such as $n_{\rm e} \simeq 1 \times 10^{20}$ m^{-3} and $T_{\rm i} \simeq T_{\rm e} \simeq 10$ keV. Finally, summary of this chapter is given in Sec. 3.5. The effect of the high electron temperature, which leads us to reconsider the electron finite orbit width effect on the neoclassical transport calculation in helical plasmas, is also discussed.

3.2 General solution of the ripple-averaged drift kinetic equation (GSRAKE)

Ripple averaged drift kinetic equation and its numerical solver, GSRAKE is widely used to calculate the neoclassical transport in helical devices so far. In GSRAKE code, it divides the distribution function into three portions of particles; locally-trapped, locally reflected but not trapped, and locally-passing ones. The average of drift kinetic equation is performed over the magnetic ripple in *ripple-averaged* drift kinetic equation. It enables ones to avoid the problem which arises in the *bounce-averaged* drift kinetic equation due to the non-localized (locally reflected but not trapped) particles since the bounce average is performed over the bounce motion of particles which are trapped in a single magnetic ripple.

In ripple-averaged drift kinetic equation, the characteristic time to average the drift kinetic equation is chosen as that which is required to traverse the a single (local) magnetic ripple instead of the bounce time of particles. Thus, the interaction between localized and non-localized particles can be described since the time is determined whether or not particles actually bounce off the ripple. In this section, we briefly review the feature of GSRAKE code.

GSRAKE calculated the neoclassical transport based on local assumptions. The radial drift of the plasma particle is neglected in the local assumptions since it is small enough compared to the plasma scale size, that is, $\Delta r/L \equiv \delta \ll 1$ is assumed, where Δr is the typical radial orbit size of the particle and L is the plasma scale size of the temperature, the density, the minor radius, *etc.* The word, *local*, comes from the fact that the plasma particles are located in a single magnetic surface in the transport time scale of $\partial/\partial t \simeq \delta^2\nu$, where ν denotes the collision frequency. It is noted that ∇B and the curvature drifts are included in original GSRAKE, however, the terms are turned off in the practical applications in this thesis. Thus, it can be said that only $\boldsymbol{E}\times\boldsymbol{B}$ drift is considered in GSRAKE. This is consistent with the local assumptions neglecting the radial drift which is mainly caused by ∇B and the curvature drift.

GSRAKE has features as follows. Since it is based on the ripple-averaged drift kinetic equation which does not require any assumptions for the collision frequency, is can obtain a solution through the entire collisionality regime. It has the great advantage of requiring less computational resources to obtain the neoclassical transport diffusivity for both ions and electrons in helical plasmas than those directly solving drift kinetic

equation with the full particle orbit. It is noted that only the pitch angle collisions are considered and the energy scattering term is neglected in GSRAKE. The detailed discussion on the difference between local neoclassical transport calculation codes such as GSRAKE and that including the finite orbit width effect is presented in Chapter 4.

3.3 Neoclassical transport analysis of high T_i plasmas in LHD

GSRAKE is applied to high-T_i plasmas obtained in LHD experiments. GSRAKE code can calculate the neoclassical particle and energy flux for ions and electrons, and the ambipolar E_r from a given T_i, T_e, and n_e profiles and the LHD magnetic field configurations. The discharges of # 75235 at $t = 1.35$ s and # 75232 at $t = 1.37$ s are chosen for the analysis from the high-T_i experiments. The ion temperature of # 75235 is about 4.8 keV with $n_\mathrm{e} \simeq 1.8 \times 10^{19}$ m^{-3} at the core, and that of # 75232 is about 3 keV at $n_\mathrm{e} \simeq 3.2 \times 10^{19}$ m^{-3} (see Fig. 3.1). It is noted that the ion temperature of # 75232 is comparable to the electron one, while the ion temperature of # 75235 is much higher than the electron one.

The heating scenario for the discharge of # 75235 is shown in Fig. 3.2 (a). The low-energy ($\simeq$ 40 keV) perpendicular neutral beam (NBI4A and B) has been injected along with the ion cyclotron range of frequency (ICRF) from $t = 0.5$ s (just after the electron cyclotron heating (ECH) turned-off), with the superposition of the high-energy ($\simeq$ 180 keV) tangential NBI (NBI1-3) from $t = 1.1$ s. The NBI4 of LHD consists of 4 ion sources with the two-independently-operatable power supplies (4A and 4B). This flexibility is utilized to modulate one of power supplies (in this case, 4B) to modulate the injection to obtain the background signals for the measurement of the ion temperature. The maximum value of T_i has been observed at $t = 1.35$ s as shown in Fig. 3.2 (b), where the all four NBIs are injected. It is noted that although the NBI3-pulse unintentionally became off at $t = 1.3$ s, the heating effect can be considered to last until $t = 1.35$ s by considering the slowing-down time of injected particles. The electron temperature and density of # 75235 at $t = 1.35$ s are also shown in Fig. 3.2 (b) with the ion temperature. The ion temperature, the electron temperature, and the electron density are measured by charge exchange recombination spectroscopy (cxs), Thomson scattering system and FIR interferometer, respectively.

The plasma parameter used in GSRAKE calculations are shown in Fig. 3.3. In Fig.

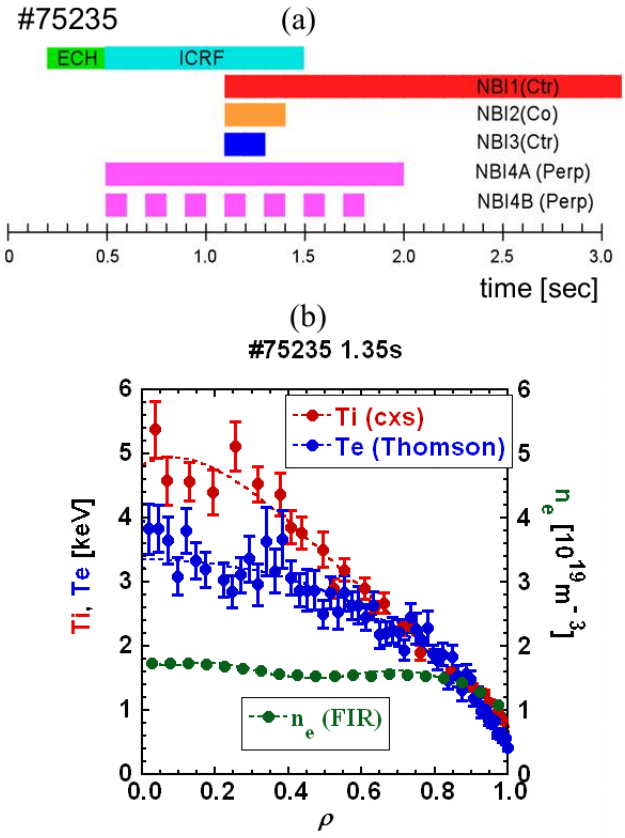

Figure 3.2: (a)The heating scenario of the discharge of # 75235 in the LHD experiment. (b) Measured plasma parameters of # 75235 at $t = 1.35$ s are shown. In this experiment, T_i, T_e and n_e are measured by charge exchange recombination spectroscopy (cxs), Thomson scattering system and FIR interferometer, respectively.

3.3 (b) and (d), the ion-ion collisionality normalized by the value at the plateau-banana boundary, $\nu_{\mathrm{i,p}} \equiv \nu_\mathrm{i}/[\epsilon_\mathrm{t}^{3/2}(v_{\mathrm{i,th}}/qR)]$ is shown, where ν_i denotes the ion-ion collisionality, $v_{\mathrm{i,th}}$ is the ion thermal velocity, ϵ_t, q, and R are the toroidicity, the safety factor, and the major radius, respectively. It can be seen in these figures that both discharges are in the low collisionality or $1/\nu$ regime in which the neoclassical transport increases in proportion to ν^{-1} without the radial electric field due to the helically-trapped particles.

The neoclassical transport is calculated by GSRAKE and numerical results for the discharge of # 75235 and # 75232 are shown in Figs. 3.4 (a) and (b), respectively. In these figures, the particle flux of the ion and the electron at $\rho = 0.2$ are shown as the function of the radial electric field. It is shown that the ion particle flux steeply increases around $E_\mathrm{r} = 0$. The increase is caused by the poloidal resonance [64] where

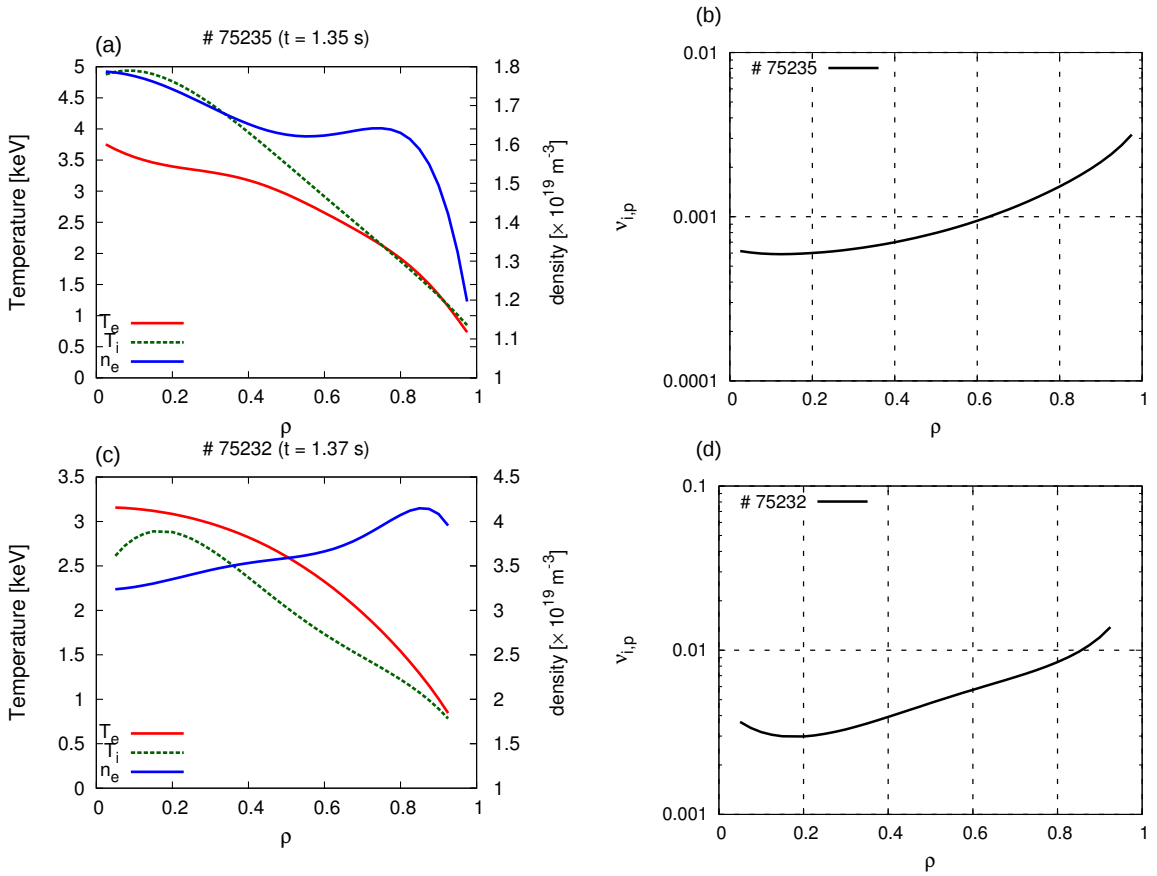

Figure 3.3: (a and c) The ion and electron temperature and the electron density, (b and d) the ion-ion collisionality normalized by the value at the plateau-banana boundary, of the discharge of # 75235 and # 75232. (a) and (b) represents those parameters for # 75235, and (c) and (d) for # 752322.

particles cannot move poloidally since $\boldsymbol{E} \times \boldsymbol{B}$ drift vanishes and no other poloidal drift is considered in the local neoclassical theory. On the other hand, the electron particle flux is not affected so much by the radial electric field as shown in the Figs. 3.4 (a) and (b). The realizable neoclassical particle flux is determined by the ambipolar condition. As a result the ion particle flux is reduced to the lower level of the electron particle flux with utilizing the ambipolar E_r and the large Γ_i at $E_\mathrm{r} = 0$ is not realized in the experiment.

The ambipolar radial electric field for both discharges are shown in Fig. 3.5 (a). The ion-root, or negative radial electric field is expected for both plasmas. The ion thermal diffusivity divided by $T_\mathrm{i}^{3/2}$ (so-called the Gyro-Bohm factor [67]), $\chi_{\mathrm{i,NC}}/T_\mathrm{i}^{3/2}$, for both discharges are shown in Fig. 3.5 (b). The thermal diffusivity without the radial electric field is also shown in the same figure for the reference purpose. From the

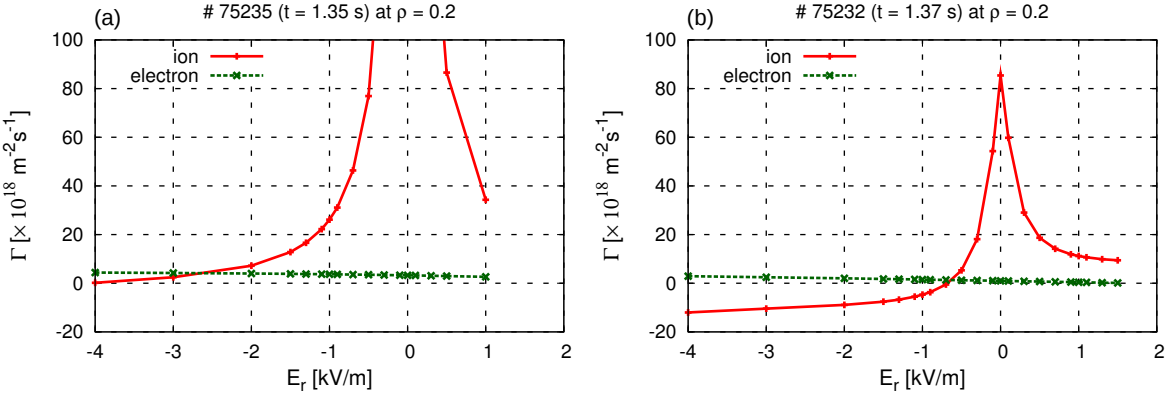

Figure 3.4: The particle flux of the ion and the electron at $\rho = 0.2$ as the function of $E_{\rm r}$. The results for (a) the discharge of # 75235, and (b) # 75232 are shown respectively. The intersection of $\Gamma_{\rm i}$ and $\Gamma_{\rm e}$ provides the ambipolar radial electric field. The ion particle flux at $E_{\rm r} = 0$ of # 75235 exceeds 1.45×10^{21} m^{-2}s^{-1}.

Fig. 3.5, it is clearly seen that the ion thermal diffusivity of # 75235 without the radial electric field is larger than that of # 75232 by about an order of magnitude. This is natural since the ion temperature of # 75235 is much higher (about two times higher) than that of # 75232 and both plasmas are in the $1/\nu$ regime. However, due to the existence of the radial electric field, the realizable ion thermal diffusivity of # 75235 is reduced to the same small level as that of # 75232. It is noted that the neoclassical particle diffusivity for the ion shows the similar result as that of the thermal diffusivity in this analysis. The results indicate that the neoclassical ion diffusivity is effectively reduced by the ambipolar radial electric field even in the high-$T_{\rm i}$ helical plasmas, and it does not show the increase followed by the increase in the ion temperature.

3.4 Numerical results of parameter survey calculations

In order to investigate the neoclassical transport properties towards reactor-relevant parameter regime, parameter survey calculations based on the discharge of # 75235 are performed. The ion temperature and the electron density of original # 75235 are widely varied numerically with keeping their profile shapes as shown in Fig. 3.6. It is noted that the values shown in Fig. 3.6 are those at the core. The ion temperature of # 75235 ($\simeq$ 4.8 keV at the core) is multiplied by 2, and the electron density of 75235 ($\simeq 1.8 \times 10^{19}$ m^{-3} at the core) is multiplied by 2, 5, and 6. The all cases are in the

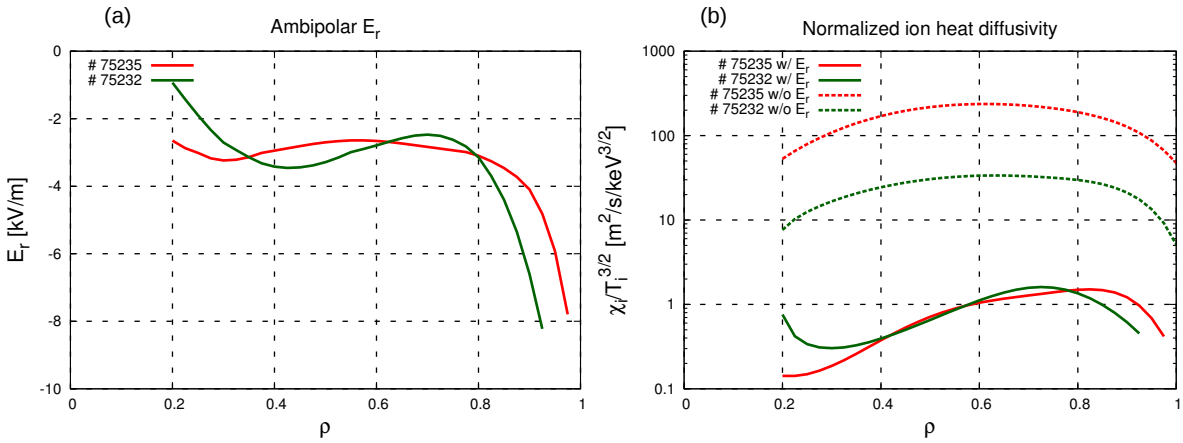

Figure 3.5: Radial profiles of (a) the ambipolar $E_{\rm r}$, and (b) the thermal diffusivity with or without the ambipolar $E_{\rm r}$ are shown for the discharge of # 75235 and # 75232, respectively.

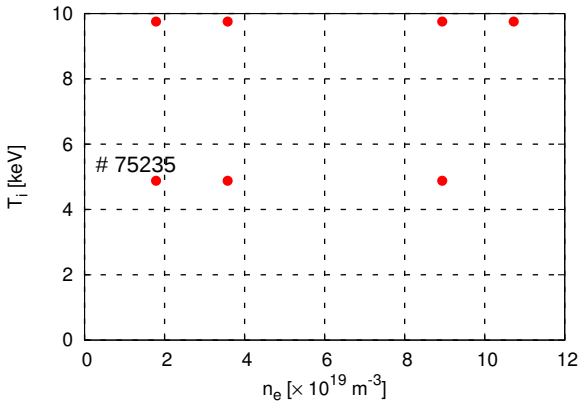

Figure 3.6: Range of the ion temperature and the electron density for the parameter survey calculations based on the discharge of # 75235.

$1/\nu$ regime. In these calculations, it is assumed that the same magnetic configuration equilibrium as that of original # 75235 is used for simplicity. It is known that the neoclassical transport tends to increase in LHD as the plasma beta increases [68]. Thus, it should be remarked that the following numerical results provide under-estimate value for the neoclassical transport.

The radial profiles of the ambipolar electric field and the ion thermal diffusivity (normalized by the Gyro-Bohm factor, $T_{\rm i}^{3/2}$) obtained by GSRAKE are shown in Figs. 3.7 (a) and (b), respectively. In this figure, the electron density is varied as the numerical parameter and both the ion and electron temperature is the same as the original # 75235. The ion-root $E_{\rm r}$ is obtained for all cases as shown in Fig. 3.7 (a). As shown

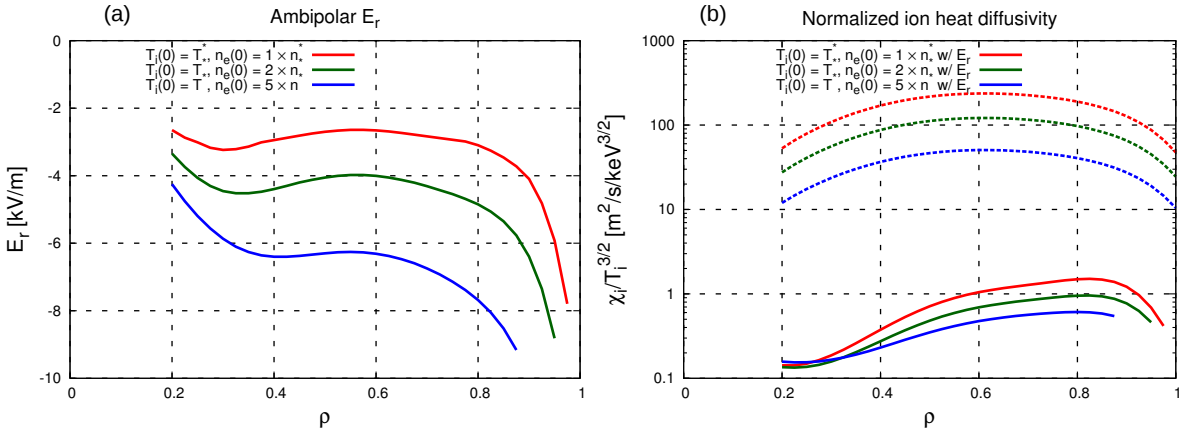

Figure 3.7: Radial profiles of (a) the ambipolar $E_{\rm r}$ and (b) the ion thermal diffusivity normalized by $T_{\rm i}^{3/2}$. In the figure (b), the dashed line represents the value at $E_{\rm r} = 0$ of the same plasma as that represented by the same color. The results correspond to the parameter survey calculations for the electron density with the fixed ion temperature. It is noted that $T^* \simeq 4.8$ keV and $n^* \simeq 1.8 \times 10^{19}$ m^{-3}, which are the values of the original # 75235, are used as abbreviations. In this calculations, the electron temperature is the same as that of the original # 75235.

in Fig. 3.7 (b), the ion thermal diffusivity without the radial electric field increases as the density and ion collisionality decreases. This is because the decrease in the ion collisionality results in the increase in the neoclassical thermal diffusivity in $1/\nu$ regime. However, with the ambipolar radial electric field taken into account, the ion thermal diffusivity for all cases becomes almost the same (small) level for all cases. It is concluded that although the neoclassical ion thermal diffusivity without $E_{\rm r}$ increases as the collisionality (density) decreases, it is reduced from those without the ambipolar $E_{\rm r}$ by one or two orders of magnitude due to the presence of the ambipolar $E_{\rm r}$.

Similar results are confirmed for the parameter survey calculations for the two-times ion temperature. As shown in Fig. 3.6, the ion temperature is doubled and electron density is varied for the calculations. As expected, even if the ion temperature (the ion collisionality) increases (decreases), the ion thermal diffusivity with the ambipolar radial electric field is reduced to almost the same level as that of the original # 75235. This is an encouraging result since, in contrast to the theoretical expectation of the increase in $1nu$ regime, the ion neoclassical transport in LHD does not increase due to the presence of the ambipolar $E_{\rm r}$ as the ion temperature increases up to 10 keV.

Next, we examine the ambipolar radial electric field and the ion thermal diffusivity numerically varying the electron temperature of the high-$T_{\rm i}$ plasma of # 75235. The

electron temperature of # 75235 is changed to become almost the same as the ion one of the plasma, *i.e.,* $T_e \simeq T_i$. Two kinds of parameter survey calculations for the electron density are carried out; (1) the ion temperature is the same as that of the original # 75235 with keeping $T_e \simeq T_i$ numerically, and (2) the ion temperature is doubled to reach 10 keV with $T_e \simeq T_i$, which aims to investigate the neoclassical transport in the reactor-relevant parameter regime.

The calculation results for the case (1) are shown in Fig. 3.8. The electron-root E_r in addition to the ion-root one which is predicted in the previous results in Fig. 3.7 comes to appear as a result of the high electron temperature as shown by the red circle case in Fig. 3.8 (a). This indicates that the multiple-root E_r exists for that plasma. The ambipolar E_r at one radial position corresponds to the electron-root one, unstable-root one, and the ion-root one from top to bottom in the figure, respectively. It is considered that the *unstable-root* E_r is in practice not realized in experiments since it is a thermodynamically unstable state. It is noted that only the ion-root E_r is obtained for two and five times higher density cases than that of the original # 75235. The ion thermal diffusivity for these plasmas is shown in Fig. 3.8 (b). When the multiple roots exist, the corresponding thermal diffusivity also has the multiple value, that is, $\chi_{i,NC}$ of the ion-root E_r, that of the unstable-root one, and that of the electron-root one, from top to bottom in the figure, respectively. It is clearly shown by the red circle in Fig. 3.8 that the ion thermal diffusivity corresponding to the electron-root E_r is further reduced by nearly one order of magnitude from that corresponding to the ion-root one.

Then, the similar calculations are performed for the case (2) and the results are shown in Fig. 3.9. In this case, it is confirmed that not only the ion-root but also the electron-root E_r is obtained for all plasmas as seen in Fig. 3.9 (a). It is emphasized that such electron-root E_r is predicted even for the two- or six-times higher density cases than that of the original # 75235. This is because that all plasmas in case (2) are in $1/\nu$ regime more deeply due to the higher ion temperature than that of case (1) plasmas. The calculated ion thermal diffusivity for these plasmas is shown in Fig. 3.9 (b). Similarly for the results of case (1), the ion thermal diffusivity of the electron-root E_r is effectively reduced by about one or two orders of magnitude from that of the ion-root one for each plasma. As a result, we can conclude from the case (1) and (2) calculations that the ion thermal diffusivity can be reduced effectively by the electron-root E_r and the electron-root radial electric field can appear due to the higher electron temperature even in the high-T_i plasmas.

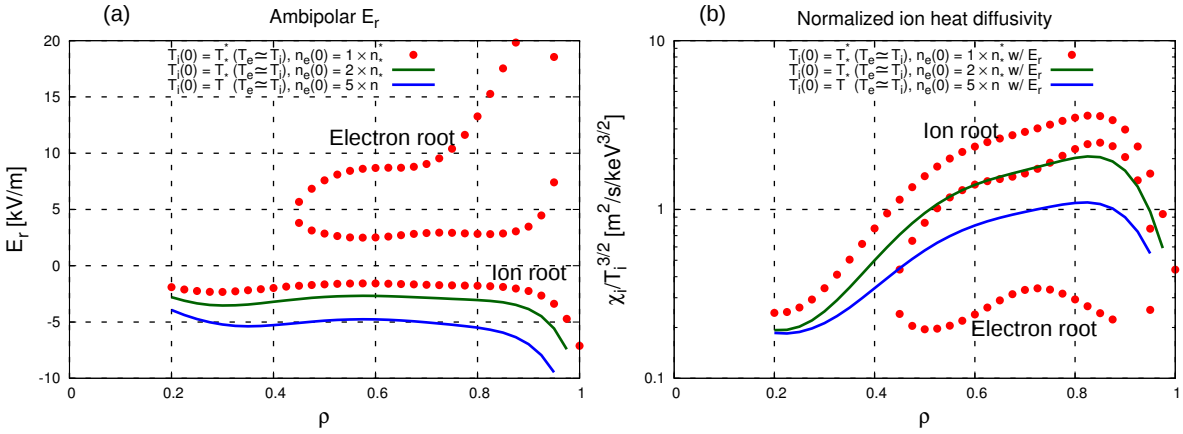

Figure 3.8: Radial profiles of (a) the ambipolar $E_{\rm r}$ and (b) the ion thermal diffusivity for the case (1) calculations. The ion temperature is the same as that of the original # 75235, while the electron temperature is set to be comparable to that of the ion in case (1) calculations. The electron density is changed numerically as in Fig. 3.7. In these figures, $T^* \simeq 4.8$ keV and $n^* \simeq 1.8 \times 10^{19}$ m^{-3} are used as the abbreviations.

3.5 Summary and discussion

In this chapter, the neoclassical transport is investigated for high-$T_{\rm i}$ plasmas observed in LHD. The neoclassical transport diffusivity and the ambipolar radial electric field are obtained by GSRAKE which solves the ripple-averaged drift kinetic equation based on local assumptions for the neoclassical transport theory. The local assumptions have been widely adopted in many numerical codes to calculate the neoclassical transport since it can calculate the neoclassical diffusivity with the plasmas parameters at a local (single) radial position. The local assumptions is based on the fact that the particle radial drift is small enough compared to the plasma scale size.

First, we apply GSRAKE to two plasma discharges of # 75235 at $t = 1.35$ s and # 75232 at $t = 1.37$ s observed in the high ion temperature experiments in LHD in FY2006. The ion temperature of # 75235 is about 4.8 keV while that of # 75232 is about 3 keV. It is demonstrated that with the ambipolar radial electric field the neoclassical ion thermal diffusivity is reduced from that without $E_{\rm r}$ by about one or two orders of magnitude for both plasmas. The ion-root $E_{\rm r}$ is predicted for these plasmas. The encouraging fact is that the ion thermal diffusivity of # 75235 remains small as that of # 75232 due to the ion-root $E_{\rm r}$ although the ion temperature of # 75235 is much higher than that of # 75232.

Next, the parameter survey calculations are carried out based on the discharge of

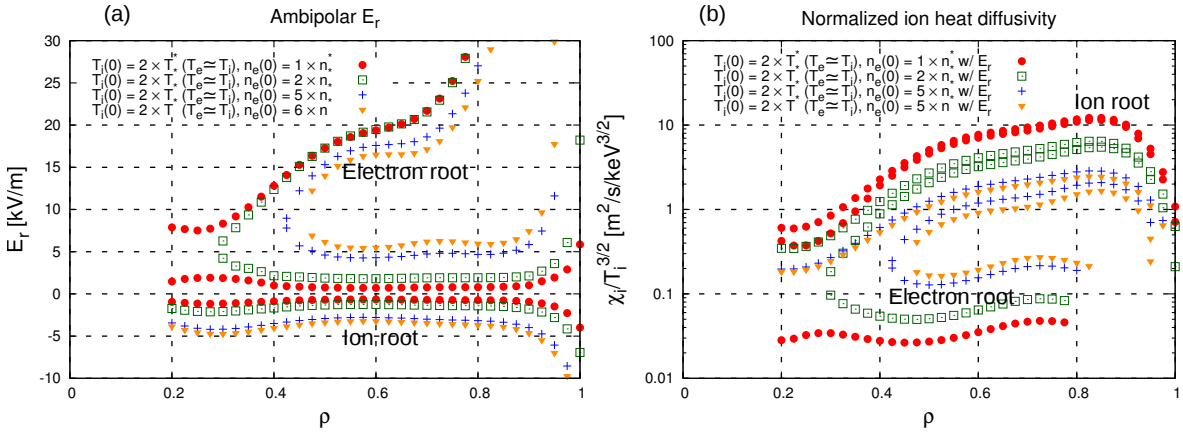

Figure 3.9: Radial profiles of (a) the ambipolar $E_{\rm r}$ and (b) the ion thermal diffusivity for the case (2) calculations. The ion temperature is doubled from that of the original # 75235, and the electron temperature is set to be comparable to that of the ion in case (2) calculations, that is, $T_{\rm e} \simeq T_{\rm i} \simeq 10$ keV. The electron density is changed numerically as in Fig. 3.7. In these figures, $T^* \simeq 4.8$ keV and $n^* \simeq 1.8 \times 10^{19}$ m^{-3} are used as the abbreviations.

75235 varying its $T_{\rm i}$, $T_{\rm e}$, and $n_{\rm e}$ numerically. This parameter survey calculations aim to examine the neoclassical transport diffusivity for the plasma in the reactor-relevant parameter regime. With those calculations, the electron-root $E_{\rm r}$ is predicted for plasmas with numerically increasing the *electron* temperature with the ion temperature to reach 10 keV, that is, $T_{\rm e} \simeq T_{\rm i} \simeq 10$ keV. It is also found in the parameter survey calculations for the electron density that this electron-root $E_{\rm r}$ is expected even for the plasma with the high electron density of $n_{\rm e} \simeq 10^{20}$ m^{-3}. The plasma of $T_{\rm e} \simeq T_{\rm i} \simeq 10$ keV and $n_{\rm e} \simeq 10^{20}$ m^{-3} is in the reactor-relevant parameter regime. The ion thermal diffusivity is reduced more effectively by the electron-root $E_{\rm r}$ than by the ion-root one. It is concluded that the electron-root $E_{\rm r}$ is predicted for a plasma with the high *electron* temperature with the high *ion* temperature, and it has an attractive feature for the reactor-relevant plasma from the viewpoint of reducing the ion neoclassical transport. With these results, we propose a more favorable heating scenario, the electron-root scenario, to achieve a higher-$T_{\rm i}$ plasma towards a reactor-relevant regime in the future.

Before proceeding to the following chapter, it is beneficial to discuss the importance of the *electron* neoclassical transport in high-$T_{\rm e}$ plasmas. In this chapter, we focus on the high-$T_{\rm i}$ plasmas and investigate their neoclassical transport by GSRAKE. As noted in Sec. 3.2, GSRAKE is based on the local assumptions. With the results in this chapter, the high electron temperature is found to be attractive to reduce the

neoclassical transport in high-$T_{\rm i}$ plasmas with the electron-root $E_{\rm r}$. This leads one to reconsider the *electron* neoclassical transport in high $T_{\rm e}$ plasmas more carefully since the high electron temperature poses a new problem of the electron finite orbit width effect which have not been paid attention so much. It is considered that the electron finite orbit width is much smaller than the ion one due to the small mass ratio, and thus, it does not affect the electron neoclassical transport. However, in high-$T_{\rm e}$ helical plasmas, helically-trapped electrons come to have the large radial drift. The electron finite orbit width effect on the electron neoclassical transport is the main issue in remains of this thesis.

Chapter 4

Numerical Solution of Drift Kinetic Equation

4.1 Introduction

In calculating electron neoclassical transport, its finite orbit width effect have been neglected since it has been considered that radial drift of electrons is much smaller than that of ions for which FOW has attracted much attention both in tokamaks and helical/stellarator devices recent years. In other words, electrons are located at a certain local magnetic surface, that is, the radial drift width of particle orbit is small enough to be neglected. Based on the small orbit width assumption, or local treatment, neoclassical transport calculations for electrons in LHD have been carried out using, for example, GSRAKE [51, 52] and DCOM/NNW [42, 43] codes. In the previous chapter, we analyze the neoclassical transport and the radial electric field in high ion temperature plasmas using GSRAKE code. However, the assumption of small orbit width adopted in these codes becomes inappropriate in high $T_{\rm e}$ helical plasmas due to the existence of helically-trapped electrons since the deviation of such particles, Δh, is proportional to $T_{\rm e}/\nu$.

As mentioned in chapter 1, high electron temperature plasmas ($T_{\rm e} \simeq 15$ keV [36]) have been obtained in recent experiments in LHD. Such plasmas are called CERC (*C*ore *E*lectron-*R*oot *C*onfinement) [23,35], since these plasmas have the strong positive radial electric field called electron root, and CERC plasmas also have the steep $T_{\rm e}$ gradient called *e*lectron *i*nternal *t*ransport *b*arrier (eITB). Moreover, the radial electric field ($E_{\rm r}$) shows a transition phenomenon from a small negative value (ion root) to the

electron root when eITB and then CERC plasma are formed [15, 37]. Due to the high temperature and the steep gradient of T_e in CERC plasmas, finite orbit width effect of electrons becomes important since Δh of electrons increases whereas the scale length of the temperature gradient decreases.

Δh is roughly estimated as follows [44];

$$\Delta h = \frac{v_d}{\nu_{eff}} = \frac{\epsilon_h}{\nu_{ei}} \frac{T_e}{eBR}, \tag{4.1}$$

where ν_{eff} is effective collisionality, ϵ_h is the helicity in the magnetic field, R is the major radius, and ν_{ei} is the electron-ion collision frequency. It is noted that the effect of E_r is not taken into account in this Δh estimation, that is, Δh is measured with $E_r = 0$. Since the drift width of a helically-trapped particle, Δh increases as $\propto T_e/\nu_{ei}$, it is uncertain whether the conventional neoclassical transport theory is rigorously valid for CERC plasmas because of its high T_e and low collisionality. The steep temperature gradient of a CERC plasma involves the small plasma scale length, thus it also may break down the local assumption of neoclassical transport theory, $\Delta h/L \ll 1$, where L denotes the typical scale length such as the plasma density, temperature, minor radius, *etc.*

Although the experimental radial transport level is much larger than that obtained by neoclassical theory due to the anomalous or turbulence transport, it has been shown that the anomalous transport is reduced by the E_r shear. The exact evaluation of neoclassical transport enables ones to determine more precisely the E_r profile and its shear through the ambipolar condition. Therefore, it is of great importance to establish the understanding of neoclassical transport including the finite orbit width in high temperature plasmas in order to estimate the reduction of the anomalous transport. It is also noted that the transitional behavior of E_r in CERC plasmas is physically an interesting topic itself, since it involves the temporally change of E_r from the ion root to the electron root which are both the stationary solution of the ambipolar condition. To clarify such behavior of E_r, it is necessary to evaluate E_r accurately.

For this purpose, FORTEC-3D code [45, 46], which numerically solves the drift kinetic equation including the finite orbit width effect of particles in three-dimensional magnetic configurations based on δf Monte-Carlo method [49, 50], is extended to be applicable to electron neoclassical transport calculations. Since the finite radial drift of a particle is included in FORTEC-3D, it can calculate the neoclassical transport non-locally with less approximations than other codes based on the local neoclassical transport theory. To implement the electron neoclassical transport calculation,

electron-ion collision term is added in FORTEC-3D.

The remainder of this chapter is organized as follows. In section 4.2, a basic formalism of δf Monte-Carlo method to solve the drift kinetic equation is discussed. A new electron-ion collision term, which is implemented in FORTEC-3D for electrons, is also described in this section. Section 4.3 is devoted to the brief comparison among FORTEC-3D, GSRAKE, and DCOM/NNW. The results obtained by latter two numerical codes are adopted as reference values of local neoclassical treatment in later sections. Then, numerical results for various plasmas for benchmarking purposes are presented in section 4.4. With this calculations, verification and validation of our new FORTEC-3D for electrons are obtained. At first, the total mode number dependence of magnetic field Fourier spectrum for FORTEC-3D simulation is investigated in this section. This result provides the basis of our simulations for the number of Fourier spectrum in following numerical calculations. Next, benchmark calculations among FORTEC-3D, GSRAKE, and DCOM/NNW are also given for the low T_{e} and relatively high collision frequency plasma in this section. It is shown in this subsection that the considerable agreement of the electron neoclassical transport with GSRAKE and DCOM/NNW calculations are obtained by FORTEC-3D simulations for this parameter regime. In section 4.5, the neoclassical transport flux is calculated for two cases both in low collisionality regime; (1) plasma with low temperature and low density and (2) plasma with high temperature. These two cases have the similar low collisionalities, although it is shown that flux dependence on E_{r} differs from each other due to the difference of the temperature. It is also shown that the low collisionality for both cases affects qualitatively the electron neoclassical transport due to the electron motion. Summary and discussion are given in Sec. 4.6 with concluding remarks.

4.2 Basic formalism in FORTEC-3D code

4.2.1 δf Monte-Carlo method

In this section, δf Monte-Carlo method adopted in numerical drift kinetic solver for arbitrary three-dimensional magnetic configuration, FORTEC-3D [45, 46], are discussed according to two weight scheme developed by Brunner, *et al.* δf Monte-Carlo method are widely used to solve drift kinetic equation and gyrokinetic equation in recent research. It is noted that δf represents the first order deviation from the equilibrium distribution function, or Maxwellian in the total distribution function, f_{a}. δf approach

to solve the drift kinetic equation has an advantage of requiring less numbers of particles compared to so-called full-f approach since it only solves δf part of the distribution function $f_{\rm a}$, which is of the order of $\delta f_{\rm a}/f_{\rm a} \sim \rho_{\rm a}/L \sim {\rm O}(\delta)$, where $\rho_{\rm a}$ denotes the Larmor radius of a particle and δ is the arbitrary ordering parameter of $\delta \ll 1$. In FORTEC-3D, to be applicable to general three-dimensional magnetic configurations, Boozer coordinates [54] are adopted, and the drift kinetic equation for a-th species distribution function $f_{\rm a}(\boldsymbol{R}, K, \mu; t)$ are described in $(\boldsymbol{R}, K, \mu; t)$ coordinates,

$$\frac{\partial f_{\rm a}}{\partial t} + \dot{\boldsymbol{R}} \cdot \nabla f_{\rm a} + \dot{K} \frac{\partial f_{\rm a}}{\partial K} = C_{\rm a}(f_{\rm a}), \tag{4.2}$$

where, $\boldsymbol{R}$ is the guiding center position vector in Boozer coordinates (Ψ, θ, ζ), and K and μ are the kinetic energy and the magnetic moment, respectively. It is noted that both parts of the distribution function are independent of gyro-angle variable, since in the drift kinetic equation, only gyro-independent part can be treated. It is also noted that Ψ, θ, ζ represent the toroidal magnetic flux, the poloidal angle, and the toroidal angle, respectively and the magnetic field $\boldsymbol{B}$ is represented as $\boldsymbol{B} = \nabla\Psi \times \nabla\theta + \iota \nabla\zeta \times \nabla\Psi$ in Boozer coordinates. As described later, in Boozer coordinates, only the strength of the magnetic field is required to solving the particle (drift) motion and it can be represented by the sum of its Fourier components as follows,

$$B(\Psi, \theta, \zeta) = \sum_{m,n} B(\Psi)_{mn} \cos(m\theta - n\zeta), \tag{4.3}$$

where, m, n are poloidal and toroidal mode number respectively. Particle distribution function is separated into two parts as,

$$f_{\rm a} = f_{0,{\rm a}}(\Psi, v) + \delta f_{\rm a}(\boldsymbol{R}, K, \mu, t). \tag{4.4}$$

Then one can obtain following linearized drift kinetic equation from eq.(4.2) using this ordering,

$$\frac{D f_{0,{\rm a}}}{Dt} = 0 \tag{4.5}$$

$$\frac{D \delta f_{\rm a}}{Dt} = -\left(\boldsymbol{v}_{\rm d} \cdot \nabla + \dot{K} \frac{\partial}{\partial K} \right) f_{\rm M,a} + C_{\rm FP}(f_{\rm M,a}). \tag{4.6}$$

It is noted that the operator D/Dt is defined by following equation

$$\frac{D}{Dt} \equiv \frac{\partial}{\partial t} + (\boldsymbol{v}_{\parallel} + \boldsymbol{v}_{\rm d}) \cdot \nabla + \dot{K} \frac{\partial}{\partial K} - C_{\rm TP}, \tag{4.7}$$

and denotes a time derivative along a particle trajectory [69], where $C_{\rm TP}$ and $C_{\rm FP}$ is a test particle and a field particle part of the linearized collision operator $C_{\rm a}$. Since we

assume that $\delta f_{\rm a}$ is of order δ, or $\delta f_{\rm a}/f_{\rm M,a} \ll 1$, the second order collision term, $C[\delta f, \delta f]$, is dropped in the linearized equation. These collision operators are explicitly written as,

$$C_{\rm TP}(h) \equiv C[h, f_{\rm M,a}] \tag{4.8}$$

$$C_{\rm FP}(h) \equiv C[f_{\rm M,a}, h], \tag{4.9}$$

where, $C[\cdot,\cdot]$ is given by the Landau collision operator [8] and h is an arbitrary distribution function. It is noted that the steady-state solution of (4.5) is a Maxwellian distribution, that is, $f_{0,\rm a} = f_{M,\rm a}$, where, $f_{M,\rm a} = n_{\rm a}\left(\frac{m}{2\pi T_{\rm a}}\right)^{\frac{3}{2}} \exp\left(-\frac{K}{T_{\rm a}}\right)$.

In δf Monte-Carlo method, the drift kinetic equation (4.6) for the first order distribution function δf is solved by following orbit trajectories of a large number of marker particles with proper collision operator. The guiding center equation of motion in Boozer coordinates are given as a Hamiltonian formulation in the reference [55, 57, 58]. Linearized collision term $C_{\rm a}(f_{\rm a})$ is defined as $C_{\rm a}(f_{\rm a}) \equiv \sum_{\rm b} C_{\rm a,b}[f_{\rm a}, f_{\rm b}]$. $\dot{\boldsymbol{R}}$ and K are obtained by following equation,

$$\dot{\boldsymbol{R}} = \boldsymbol{v}_{\parallel} + \boldsymbol{v}_{\rm d} \tag{4.10}$$

$$\dot{K} = e_{\rm a}\boldsymbol{v}_{\rm d} \cdot \boldsymbol{E}_{\rm r}, \tag{4.11}$$

where, $v_{\parallel} = \dot{\boldsymbol{R}} \cdot \boldsymbol{b}$ and $\boldsymbol{v}_{\rm d}$ is the drift velocity of the guiding center, and $\boldsymbol{b}$ is a unit vector tangential to magnetic field $\boldsymbol{B}$. $E_{\rm r}$ represents the radial electric field, where potential Φ is assumed to depend only on a magnetic surface label Ψ.

In FORTEC-3D, two kinds of weight, $w_{\rm i}, p_{\rm i}$ for each marker particle are introduced according to references [49] and [50], where subscript i denotes marker particle number in following way. δf is represented as the product of the *marker* particle distribution $g(\boldsymbol{R}, K, t)$ and the weight field $W(\boldsymbol{R}, K, t)$ as

$$\delta f(\boldsymbol{R}, K, \mu, t) = g(\boldsymbol{R}, K, \mu, t) W(\boldsymbol{R}, K, t). \tag{4.12}$$

Then one can obtain following equation for g,

$$\frac{Dg}{Dt} = 0. \tag{4.13}$$

In two weighting scheme, the second weight field of the marker particle distribution function $P(\boldsymbol{R}, K, t)$ is defined as,

$$f_{\rm M}(\boldsymbol{R}, K) = g(\boldsymbol{R}, K, \mu, t) P(\boldsymbol{R}, K, t). \tag{4.14}$$

The marker particle distribution function $F(\boldsymbol{R}, K, \mu, w, p, t)$ in the extended phase space $(\boldsymbol{R}, K, \mu, w, p)$ is introduced to numerically represent the N marker particles,

$$\begin{aligned} & F(\boldsymbol{R}, K, \mu, w, p) \\ = & \sum_{i=1}^{N} \delta(\boldsymbol{R} - \boldsymbol{R}_i(t))\delta(K - K_i(t))\delta(\mu - \mu_i(t))\delta(w - w_i(t))\delta(p - p_i(t)), \end{aligned} \tag{4.15}$$

where $(\boldsymbol{R}_i(t), K_i(t), \mu_i(t), w_i(t), p_i(t))$ denotes the i-th particle position, kinetic energy, magnetic moment, and weights at the time t, and $w_i(t)$ and $p_i(t)$ are given as $w_i(t) = W(\boldsymbol{R}_i(t), K_i(t), \mu_i(t), t)$ and $p_i(t) = P(\boldsymbol{R}_i(t), K_i(t), \mu_i(t), t)$, respectively. Using F, one can obtain following relations as,

$$g(\boldsymbol{R}, K, \mu, t) = \int dwdpF(\boldsymbol{R}, K, \mu, w, p) \tag{4.16}$$

$$f_{\mathrm{M}}(\boldsymbol{R}, K, t) = \int dwdppF(\boldsymbol{R}, K, \mu, w, p) \tag{4.17}$$

$$\delta f(\boldsymbol{R}, K, \mu, t) = \int dwdpwF(\boldsymbol{R}, K, \mu, w, p), \tag{4.18}$$

and these lead to the following numerically possible evaluation of the distribution function as;

$$g(\boldsymbol{R}, K, t) = \sum_{i=1}^{N} \delta(\boldsymbol{R} - \boldsymbol{R}_i(t))\delta(K - K_i(t))\delta(\mu - \mu_i(t)) \tag{4.19}$$

$$f_{\mathrm{M}}(\boldsymbol{R}, K, t) = \sum_{i=1}^{N} p_i(t)\delta(\boldsymbol{R} - \boldsymbol{R}_i(t))\delta(K - K_i(t))\delta(\mu - \mu_i(t)) \tag{4.20}$$

$$\delta f(\boldsymbol{R}, K, t) = \sum_{i=1}^{N} w_i(t)\delta(\boldsymbol{R} - \boldsymbol{R}_i(t))\delta(K - K_i(t))\delta(\mu - \mu_i(t)). \tag{4.21}$$

In summary, in δf Monte-Carlo method the trajectories of marker particles are followed in the extended phase space $(\boldsymbol{R}, K, \mu, w, p)$ to obtain $\delta f(\boldsymbol{R}, K, \mu, t)$, which is the solution of the first order linearized drift kinetic equation at time t.

Time evolution for w_{i} and p_{i} are described as following equation,

$$\dot{w}_{\mathrm{i}} = \frac{p_{\mathrm{i}}}{f_{\mathrm{M,a}}} \left(-\boldsymbol{v}_{\mathrm{d}} \cdot \nabla - \dot{K} \frac{\partial}{\partial K} + C_{\mathrm{FP}} \right) f_{\mathrm{M,a}} \tag{4.22}$$

$$\dot{p}_{\mathrm{i}} = \frac{p_{\mathrm{i}}}{f_{\mathrm{M,a}}} \left(\boldsymbol{v}_{\mathrm{d}} \cdot \nabla + \dot{K} \frac{\partial}{\partial K} \right) f_{\mathrm{M,a}} \tag{4.23}$$

Time evolution for each marker particle variables, $(\boldsymbol{R}, K, \mu, w, p)$ are followed and then δf after several time steps are simulated numerically by the summation of the whole

marker particle, namely;

$$\delta f = \sum_i w_{\rm i} g, \tag{4.24}$$

and the neoclassical particle flux $\Gamma_{\rm a}$ and energy flux $Q_{\rm a}$ are given as follows;

$$\Gamma_{\rm a} = \langle \int d^3v \dot{\Psi} \delta f \rangle \tag{4.25}$$

$$Q_{\rm a} = \langle \int d^3v \frac{1}{2} m_{\rm a} v^2 \dot{\Psi} \delta f \rangle, \tag{4.26}$$

where $\langle \cdot \rangle$ denotes a magnetic-surface averaged value. The flux is evaluated by using Ψ as the radial coordinate, thus, to obtain the physical particle and energy flux, $\Gamma_{\rm a}$ and $Q_{\rm a}$ must be divided by $\langle |\nabla \Psi| \rangle$, that is, $\Gamma_{\rm a} = \Gamma_{\rm a}/\langle |\nabla \Psi| \rangle$ and $Q_{\rm a} = Q_{\rm a}/\langle |\nabla \Psi| \rangle$.

4.2.2 Collision operator for unlike-particles

So far, FORTEC-3D has been applied only for ions, thus the test particle collision term does not involve unlike-particle (ion-electron) collisions because of large mass ratio of ion to electron. However, the electron neoclassical transport calculations, which are carried out in this thesis, require unlike-particle, or electron-ion collision term in addition to the like-particle (electron-electron) collision term. Thus a new test particle collision operator is added for FORTEC-3D for electron-ion collisions.

In FORTEC-3D for electrons, ion distribution function is assumed to be a local Maxwellian with average velocity $V_{\rm i} = 0$, then electron-ion collision term is written as follows [8];

$$\begin{aligned} C_{\rm ei} &= \nu_{\rm ei} L(f_{\rm e}) \\ &= \frac{\nu_{\rm ei}}{2} \frac{\partial}{\partial \lambda} \left(1 - \lambda^2\right) \frac{\partial \delta f}{\partial \lambda}, \end{aligned} \tag{4.27}$$

where, L represents a Lorentz (pitch angle scattering) operator and λ is a pitch angle of a particle defined as $\lambda \equiv v_{\parallel}/v$. $\nu_{\rm ei}$ is a collision frequency between electron and ion. Since ion is assumed to be a stationary local Maxwellian, only pitch angle collision between electron and ion is required. In FORTEC-3D pitch angel scattering represented above (4.27) is modeled by random change of a particle pitch angle in velocity space as follows [70];

$$\lambda_n = \lambda_{n-1} \left(1 - \nu_{\rm ei} \tau\right) \pm \left[\left(1 - \lambda_{n-1}^2\right) \nu_{\rm ei} \tau\right]^{\frac{1}{2}}, \tag{4.28}$$

where, τ is a simulation time step and subscript n represents a n-th time step in calculation time. It is noted that the sign of the second term in the right hand side

in equation (4.28) is randomly determined. Since simulation markers in FORTEC-3D are not mono-energy but are distributed in the velocity space (initially Maxwellian), some of them have very slow velocity, or large ν_{ei}. This results in the existence of particles which has collisionality of $\nu_{\mathrm{ei}}\tau > 1$ and collision operator above cannot be applied for such particles. To avoid this situation, pitch angle of such a slow particle in n-th step is determined by a random number of $[-1, 1]$ regardless of its pitch angle in $(n-1)$-th step. In this way, FORTEC-3D for electrons simulate not only small angle scattering but also large angle scattering for particles with slow velocities. It is noted that the very few particles are such slow particles, the collision operator for the slow particles influences little the results in practical FORTEC-3D simulations, that is, about 0.006 % of the total particles are affected by the such collision. In FORTEC-3D, Three constants of motion of total particle number, momentum, and energy are all conserved for like-particle (in this case, electron-electron) collisions with proper field particle operator, while they are not the case for unlike-particle (electron-ion) collisions described in this section, that is, momentum is not conserved for electron-ion collisions.

4.3 Comparison between FORTEC-3D and other numerical codes

In this subsection, difference among FORTEC-3D, GSRAKE, and DCOM/NNW is briefly reviewed. Although GSRAKE and DCOM/NNW calculate the neoclassical particle and heat flux as well as FORTEC-3D, there are some essential differences in GSRAKE and DCOM/NNW from FORTEC-3D due to the assumptions they adopt.

GSRAKE solves the ripple-averaged drift kinetic equation for both trapped particles and transit (passing) ones. It is noticed that the Fourier components of magnetic field B_{mn} with high-n ($|n| \geq 20$) are neglected in the ripple averaging procedure in GSRAKE. In addition to this, GSRAKE assumes that the typical particle drift velocity is small enough so that the deviation of particles from a certain magnetic surface during one bounce motion is very small for both trapped and passing particles, thus local treatment can be applied: $\Delta r/L \ll 1$ is assumed for plasma particles, where Δr and L denote the drift orbit width of a particle in a radial direction and typical scale length such as of density or temperature gradient. In other words, particle and heat diffusion due to collisions can be determined only by plasma parameters on a magnetic surface.

On the other hand, DCOM/NNW calculates the neoclassical particle and heat flux

based on the drift kinetic equation without the ripple-averaging procedure as is done in FORTEC-3D. It is also noted that DCOM/NNW adopts δf Monte-Carlo method to solve the drift kinetic equation and the full particle orbit is followed in DCOM/NNW calculation. And there is no limit on magnetic mode number in DCOM/NNW. DCOM/NNW just follows mono-energy particle trajectory and calculates the diffusion coefficient $D(K)$ from the particle deviation from a particular magnetic surface after several time steps as,

$$D(\Psi, K) = \frac{1}{2tN} \sum_{i}^{N} \left(\Psi_{\mathrm{j}}(t) - \Psi_{\mathrm{j},0}\right), \tag{4.29}$$

where N represents the number of particles, K is the kinetic energy of a particle, $\Psi_{\mathrm{j}}(t)$ is the j-th particle radial position at time t, and $\Psi_{\mathrm{j},0}$ is the initial position of that particle. It is noted that in DCOM/NNW practically energy-dependent diffusion coefficient $D(K)$ is evaluated as a function of normalized collision frequency $\nu^*_{\mathrm{bn}} \equiv \nu_{\mathrm{ab}}/(v/qR)$, namely, $D(\nu^*_{\mathrm{bn}})$ is calculated in DCOM/NNW, where ν_{ab} is a collision frequency between species a and b, q is a safety factor, and R is the major radius. The particle energy K, or the particle velocity v, is fixed at very low value and ν_{ab} is given as an input variable. The particle energy in DCOM/NNW is typically on the order of 10^{-3} eV to avoid the deviation of a particle from its initial magnetic surface. This use of ν_{ab} instead of the particle energy K enables DCOM/NNW to evaluate the diffusion coefficient from slow particles of which radial drifts are negligibly small in its δf Monte-Carlo method, that is, DCOM/NNW is also based on the local neoclassical theory. Then diffusion coefficient $D(\Psi)$ at a certain magnetic surface is given by integrating $D(\Psi, K)$ over energy, and this is implemented by integrating $D(\Psi, \nu_{\mathrm{ab}})$ over ν_{ab} in DCOM/NNW. It is also noticed that collision operator used in DCOM/NNW is only the pitch angle scattering as well as GSRAKE.

Contrary to these assumptions, in FORTEC-3D, the particles orbits with various energy are directly followed in entire plasma volume, and thus, the finite orbit width effects for neoclassical transport can be rigorously taken into account. In addition, exact expression for magnetic field can be used in FORTEC-3D and its collision operator for like-particle collision involves energy scattering term and field particle term which conserves total number of particles, momentum, and energy. The main differences among three codes are summarized in table 4.1.

	FORTEC-3D	GSRAKE	DCOM/NNW
particle orbit	full orbit	full orbit (low energy particles)	ripple-averaged eq.
coll. operator	full for C_{ee} PAS for C_{ei}	PAS	PAS
magnetic field	arbitrary	arbitrary	low n component

Table 4.1: Differences among FORTEC-3D, GSRAKE, and DCOM/NNW. PAS is an abbreviation for the pitch angle scattering.

4.4 FORTEC-3D results in moderate collisionality regime

Neoclassical particle and heat flux for electrons are calculated by using extended FORTEC-3D. In order to check the validity of our new FORTEC-3D, benchmark calculations are carried out with other codes, GSRAKE and DCOM/NNW, which have been widely used. In this section, we focus on the plasma in the moderate collisionality regime which is considered to be affected less by the finite orbit width effect.

4.4.1 Calculation conditions

Benchmark calculations are carried out for a moderate temperature ($T_e(0) = 1.0$ keV) plasma. Equilibrium magnetic field configuration of $B(0) = 3.0$ T and $R_{ax} = 3.60$ m is adopted for the benchmarking purpose. It is known that the neoclassical transport is reduced as the magnetic axis is shifted inward from standard configuration $R_{ax} = 3.75$ m in LHD (so called σ-optimization) [71]. This reduction of neoclassical transport results from the fact that in this σ-optimized LHD configuration, the radial excursion of particles from a magnetic surface is suppressed, thus it is considered that $R_{ax} = 3.6$ m configuration has a favorable character for benchmark calculation. As a result, the non-local effect or the deviation from a magnetic surface which is considered to be small in conventional neoclassical assumption such as GSRAKE and DCOM/NNW is relatively less significant in this configuration. Also, since the finite orbit width effect of electron or Δh (see eq.(4.1)) is considered to be negligible in such a low temperature plasma, the results are expected to agree among three numerical codes. It is noted the radial profile of radial electric field is given as an input parameter for all calculations performed in this chapter and it is independent of the time.

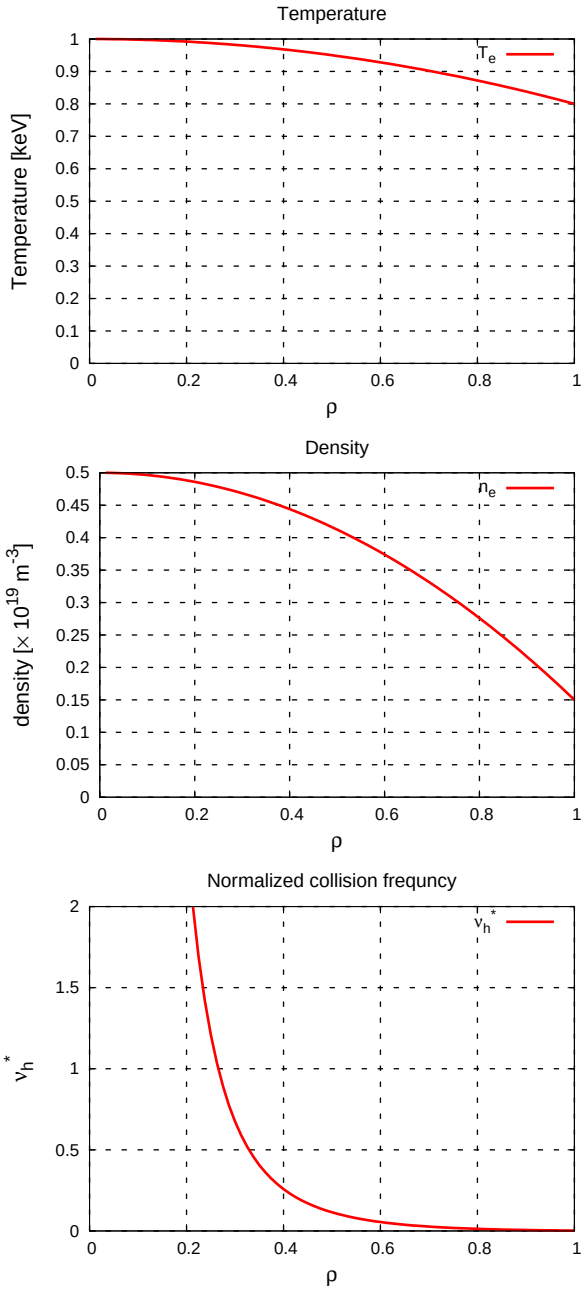

Figure 4.1: Plasma profile used in the benchmark calculation. The electron temperature (top), density (middle), and the resulting collisionality (bottom) are shown respectively. It is noted that $T_\mathrm{e} = T_\mathrm{i}$ and $n_\mathrm{e} = n_\mathrm{i}$ are assumed. The collisionality is shown as normalized value as $\nu_\mathrm{h}^* = \nu_\mathrm{ei} / \left[\epsilon_\mathrm{h}^{\frac{3}{2}} \left(v_\mathrm{th}/qR\right)\right]$, where ϵ_h denotes the helicity of the magnetic field.

For numerical results obtained by FORTEC-3D, 2,048,000,000 of marker particles are used to reduce the inevitable calculation noise from Monte-Carlo method. It is noted that sufficient number of marker particles are required to guarantee the results from δf Monte-Carlo method to reduce the calculation noise which is proportional to $1/\sqrt{N}$, where N is the total number of marker particles. It is also noted that $|\delta f_{\rm a}/f_{\rm M,a}| \ll 1$ needs to be satisfied in the whole calculation time. In the following calculations, the number of marker particles used here is confirmed to be enough to satisfy $|\delta f_{\rm a}/f_{\rm M,a}| \ll 1$. It is also noted that a time step, Δt, is chosen as adequately small to follow a typical marker particle orbit (e.g., a particle having the thermal velocity) precisely.

The radial profiles of the plasma parameters used in this calculation is shown in Fig. 4.1 It is noted that collision frequency is normalized by the value at the plateau-$1/\nu$ boundary which is defined in neoclassical theory in asymmetric devices, that is, $\nu_{\rm h}^* \equiv \nu/v_{\rm ei}/\left[\epsilon_{\rm h}(v_{\rm th}/qR)\right]$. It is noted that the normalized collision frequency represents the bounce frequency of helically-trapped particles [19]. The ion temperature and density are assumed to be the same as those of electron for simplicity; $T_{\rm e} = T_{\rm i}$ and $n_{\rm e} = n_{\rm i}$. The collisionality in this case is in the so-called $1/\nu$ regime for almost the entire plasma. Figure 4.2 shows a typical time evolution of the electron particle flux, $\Gamma_{\rm e}$ at $\rho = 0.5$. The simulation result reaches the steady state in a few electron-ion collision times. The electron energy flux, $Q_{\rm e}$, also reaches steady state at the same time in this simulation. In the remainder of this paper, all simulated values of the particle and energy flux are averaged over a finite interval in this steady state.

4.4.2 Magnetic mode number dependence

As already mentioned in the previous subsection, LHD $R_{\rm ax} = 3.60$ m configuration has a desirable character for the benchmark calculation among three codes. The magnetic configuration in terms of Fourier components (m, n) for LHD is obtained by using VMEC code [72], which calculates MHD equilibrium with a given plasma pressure and a current. The equilibrium is converted to Boozer coordinates. Although the magnetic field strength is expressed by many components of B_{mn}, most of them are negligibly small and considered to have no large contribution for the simulation results. Since the number of magnetic Fourier spectrum used in FORTEC-3D greatly affects the computational time, numerical results dependence on the number of magnetic mode needs to be investigated to effectively reduce the computational burden. It is noted

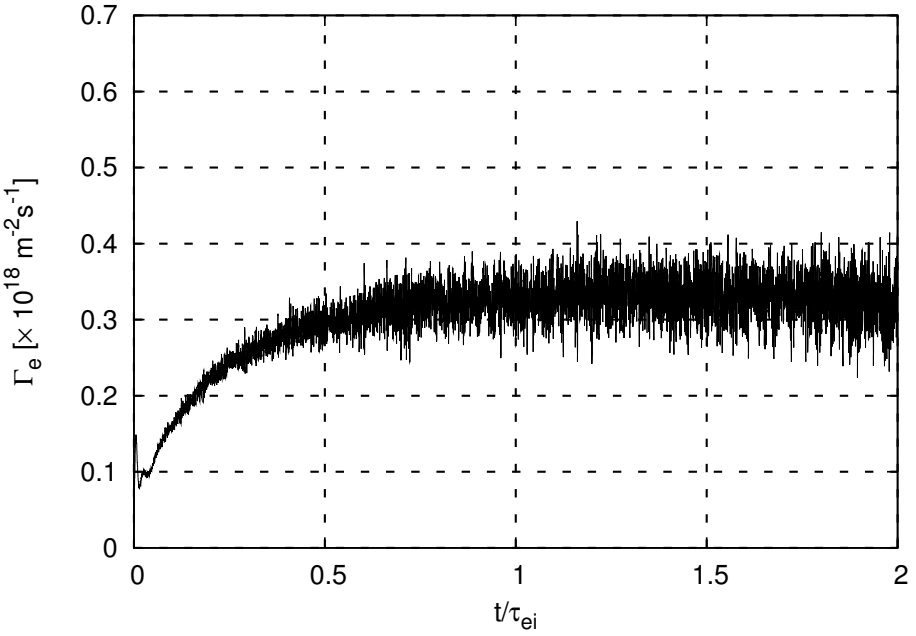

Figure 4.2: A typical time evolution of electron particle flux Γ_e at $\rho = 0.5$ calculated by FORTEC-3D simulation is shown. The time is normalized by the electron-ion collision time, τ_{ei}, at $\rho = 0.5$.

that the Fourier components used in GSRAKE is 11, namely, $m = 0, 1, 2$, and 3, and $n = -10, 0$, and 10 for each m except $m = 0$ are used.

To check the convergence, FORTEC-3D calculations are performed for the same plasma parameters with varying the number of Fourier modes, namely, 8, 12, and 16. The results are shown in Fig. 4.3. It is noted that in these calculations, the same calculation condition (particle number, plasma profiles, *etc.*) as that mentioned in the previous section are used and $E_r = 0$ kV/m in the entire plasma is adopted for simplicity. In Fig. 4.3, all the results are averaged over 3000 time steps for collision calculation, or $\Delta t = 0.3\ \tau_{ei}$ after reaching the steady state, where τ_{ei} is a collision time between electron and ion. As can be seen clearly in these figures, there is no significant discrepancy when the total mode number of 12 or 16 is adopted. These results show that the truncated higher components of magnetic field affect little the numerical results in FORTEC-3D. Thus, in the remainder of this thesis, for LHD $R_{ax} = 3.60$ m magnetic configuration, FORTEC-3D are carried out with either the magnetic mode number = 12, or, 16. Based on this fact, the limited mode number used in GSRAKE, which is one of the differences between FORTEC-3D and GSRAKE, is not the reason to explain the difference of Γ_e between these two codes shown in later section.

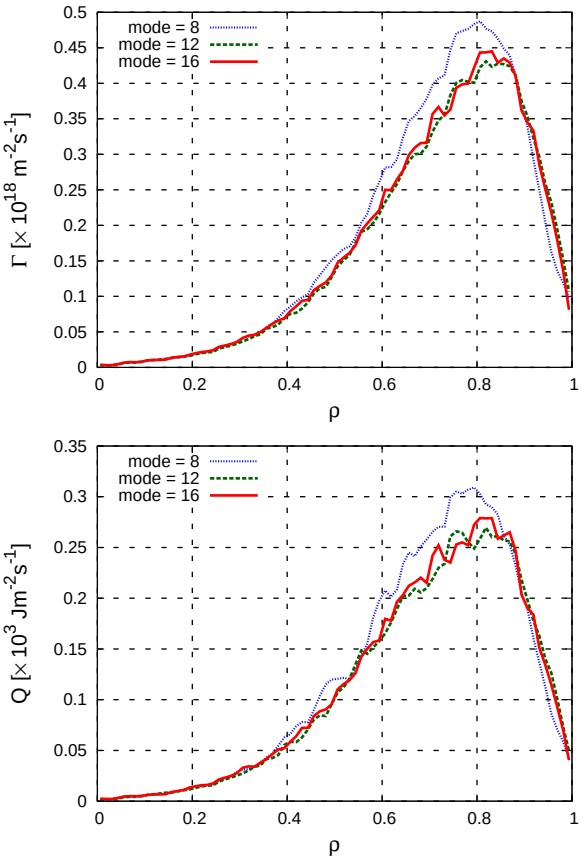

Figure 4.3: The dependence on the number of magnetic Fourier spectrum for the electron particle (top) and energy (bottom) flux in FORTEC-3D. For these calculations, $E_{\mathrm{r}} = 0$ is assumed through the entire plasma region.

4.4.3 Comparison among FORTEC-3D and local transport codes

Based on the discussion in the preceding sections, benchmark calculations have been performed for various E_r profiles to investigate the dependence of the particle and heat flux on E_r. It is noted that the E_r is given as either radially a linear or parabolic profile, that is, $E_r(\rho) = E_0\rho$, or $E_r(\rho) = E_0\rho + E_1\rho^2$ for simplicity, where E_0 and E_1 are given numerical constants, respectively.

Some of the calculation results are shown in Fig. 4.4. For each E_r profile, both the particle and heat flux reach the steady state, and plotted are the values averaged over 0.3 τ_{ei} in the steady state. All the cases are calculated by the time, $t/\tau_{ei} \simeq 2.0$. In this figure, E_r has a linear profile and $E_0 = 10$, 0, and -10 kV/m, respectively. The calculation results obtained by FORTEC-3D are compared with both GSRAKE and DCOM/NNW with corresponding E_r used in the FORTEC-3D calculation, see Fig. 4.4. It is clearly shown in these figures that the particle flux calculated by FORTEC-3D has a similar radial profile as those obtained by both GSRAKE and DCOM/NNW for the case of $E_0 = -10$ and 10 cases in the entire plasma region, although its numerical value is different to some extent. Also in the case of $E_0 = 0$, this similarity of radial profile of Γ_e can be seen in Fig. 4.4 except at the edge region of $\rho > 0.9$. The electron energy flux is also calculated by these codes and it shows a similar tendency as the particle flux.

To see this feature in detail, E_r dependence has also been investigated. The electron particle and energy flux with E_r on $\rho = 0.2$, 0.5 and 0.8 obtained by FORTEC-3D are shown by triangles in Fig. 4.5. Also plotted there are the results by GSRAKE and DCOM/NNW for the benchmarking purpose. It is noticed that at $\rho = 0.8$, both particle and energy flux obtained by GSRAKE and DCOM/NNW codes show a little peak around $E_r = 0$, while results from FORTEC-3D do not show it. This is the reason why the difference between FORTEC-3D and the other two codes increases especially at the outer region for a case of $E_0 = 0$ in Figure 4.4. However, in these figures, it is confirmed that FORTEC-3D for electrons reproduces the similar E_r dependence of the electron flux obtained by GSRAKE and DCOM/NNW at all surfaces in reasonable accuracy. Consequently, numerical results of FORTEC-3D for electrons show a reasonably good agreement with those obtained by GSRAKE and DCOM/NNW for a plasma with moderate temperature in LHD $R_{ax} = 3.60$ m configuration. We can thus conclude that these numerical resultss provide a sufficient basis for applying the

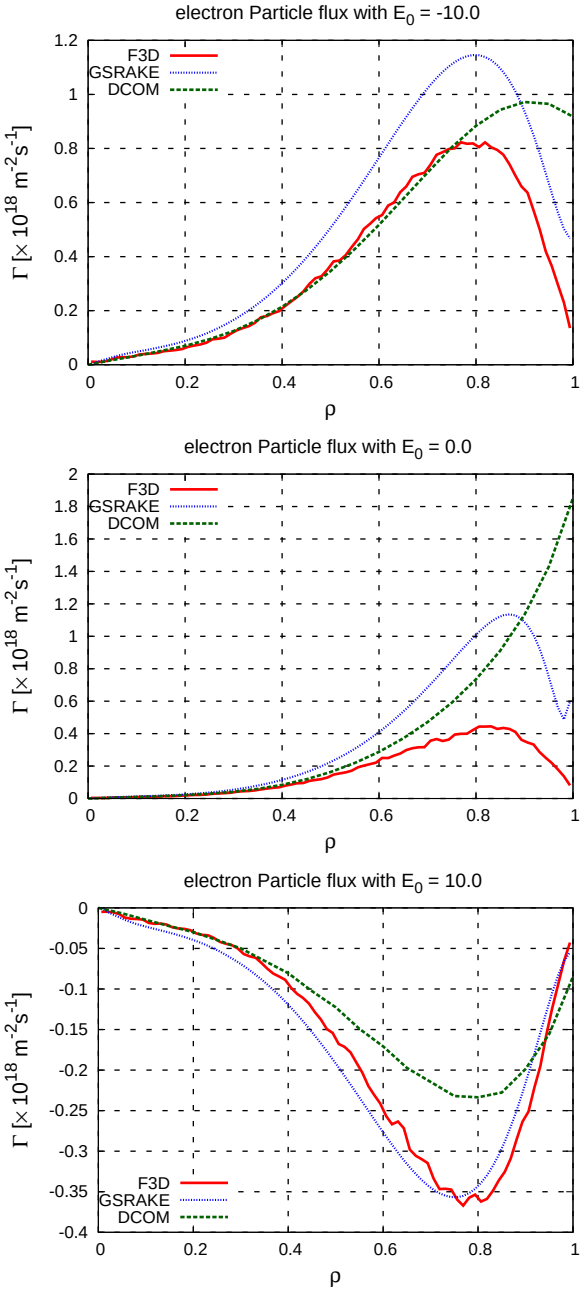

Figure 4.4: Radial profile of the electron particle flux calculated by FORTEC-3D (denoted by F3D, solid line), GSRAKE(dashed line), and DCOM/NNW(dotted line) for $E_0 = -10$ (top), 0 (center), and 10 (bottom) are shown respectively.

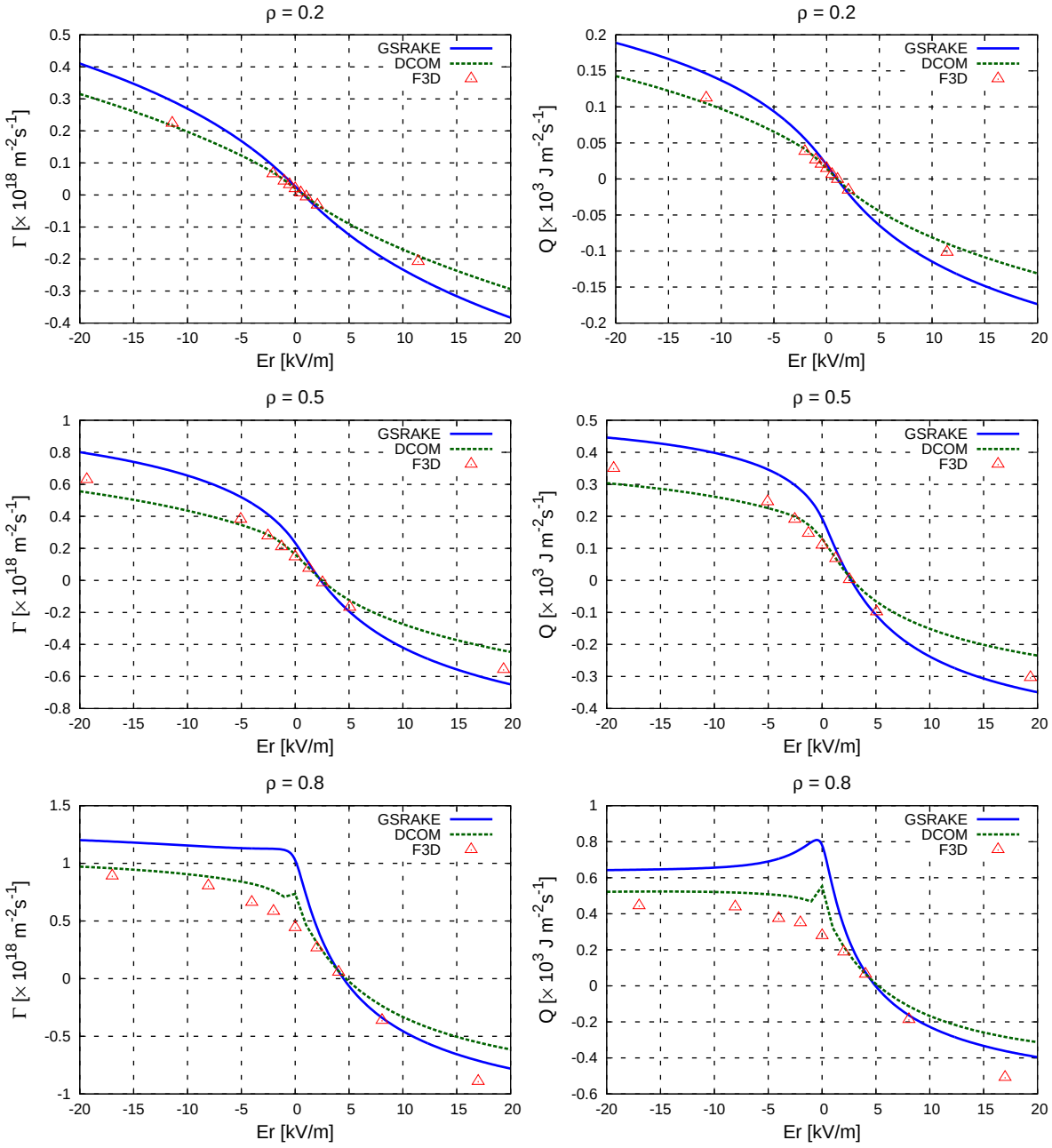

Figure 4.5: Electron particle (left) and energy flux (right) on various magnetic surfaces ($\rho = 0.2$, 0.5, and 0.8 from top to bottom) in the benchmark calculation by FORTEC-3D (F3D, triangles), GSRAKE (solid line), and DCOM/NNW (dashed line) is shown as a function of E_{r}.

δf Monte-Carlo method to solve the drift kinetic equation for electrons involving the non-local effect.

4.5 FORTEC-3D results in low collisionality regime

4.5.1 Two approaches for lowering collisionality

Since CERC plasmas in LHD or other helical devices have very high T_e and thus the low collision frequency with the steep T_e gradient, a rigorous neoclassical transport calculation including the electron finite orbit width effect is required to study their confinement property, especially to determine the ambipolar E_r. The electron particle and heat flux dependence on the radial electric field for plasmas in the low-collisionality regime is investigated by FORTEC-3D in this section. It is noted that both the high temperature and the low density result in the low collisionality and the finite orbit width effect arises from both the low collisionality and the high temperature. In this section, we perform simulations for two cases of plasmas, that is, FORTEC-3D for electrons are applied to lower density (case (1)) and higher T_e (case (2)), respectively, as examples for lowering collisionality compared to a case examined in a previous section.

Plasma profiles for these cases are shown in Fig. 4.6 simultaneously. Also in these figures, the normalized collisionality is used as in Fig. 4.1. These two plasmas are both well in the $1/\nu$ regime as shown in Fig. 4.6. It is noted that the calculations in this section are carried out with the total magnetic mode number of 12 in order to reduce computational time since a time step needs to be small enough in the low-collisionality regime. The values obtained in this simulation are averaged over 0.3 τ_{ei} after reaching the steady state. The radial electric field profiles are similar as used in the previous section. It is noted that the collisionality of these two cases is similar to each other, although the temperature and the density are quite different. Consequently, as discussed in Sec. 4.1, the typical orbit widths of trapped particles, $\Delta h \propto T_e/\nu_{ei} = n_e T_e^{5/2}$ for these two cases differ as follows. Δh at $\rho = 0.5$ is estimated as $\simeq 0.066$ cm for case (1) and 2.2 cm for case (2). It is considered that the case (1) corresponds to low collisionality case with the small radial deviation, while the case (2) with the larger radial drift width although it has a low collisionality similar to that of case (1). For the reference, the typical banana width of trapped ions in tokamak is estimated as $q\rho_i/\sqrt{\epsilon_t}$ [8]. It is noted that the ion temperature is the same as that of the electron for both cases and the banana width becomes $\simeq 0.626$ cm for case (1) and

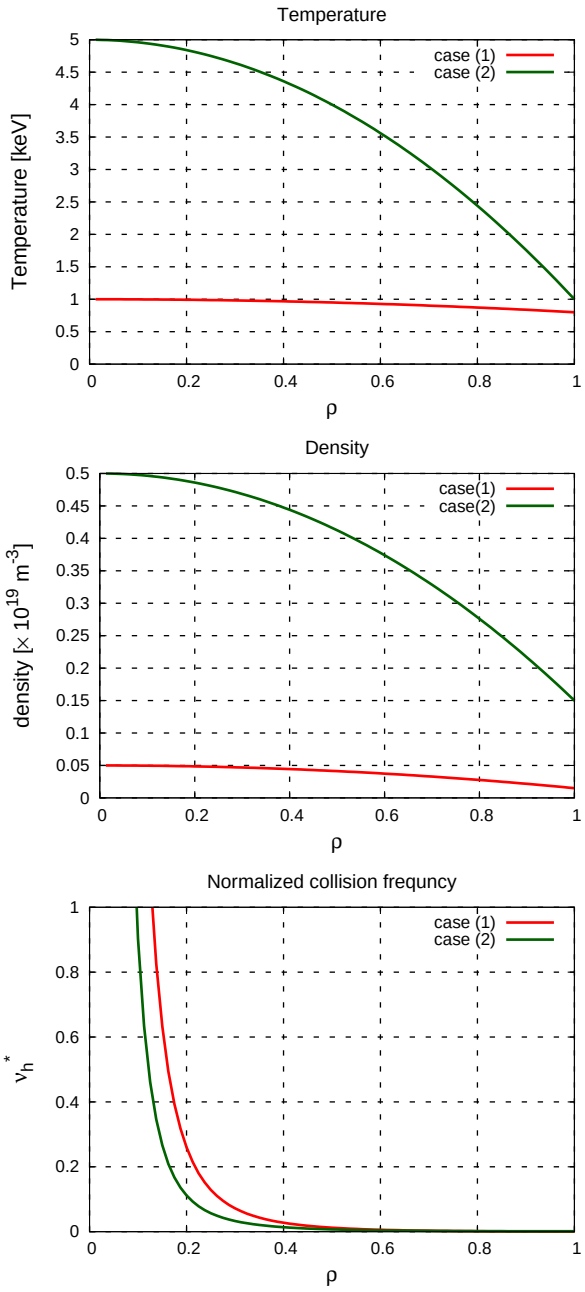

Figure 4.6: Plasma profiles used in the calculation for low collisionality plasmas. $T_{\rm e}(0) = 1.0$ keV and $n_{\rm e}(0) = 0.05 \times 10^{19}$ m^3 for case (1) (solid line), and $T_{\rm e}(0) = 5.0$ keV and $n_{\rm e}(0) = 0.5 \times 10^{19}$ m^{-3} for case (2) (dashed line), respectively. Temperature (top), density (middle), and collisionality (bottom) are shown. It is noted that $T_{\rm e} = T_{\rm i}$ and $n_{\rm e} = n_{\rm i}$ are assumed.

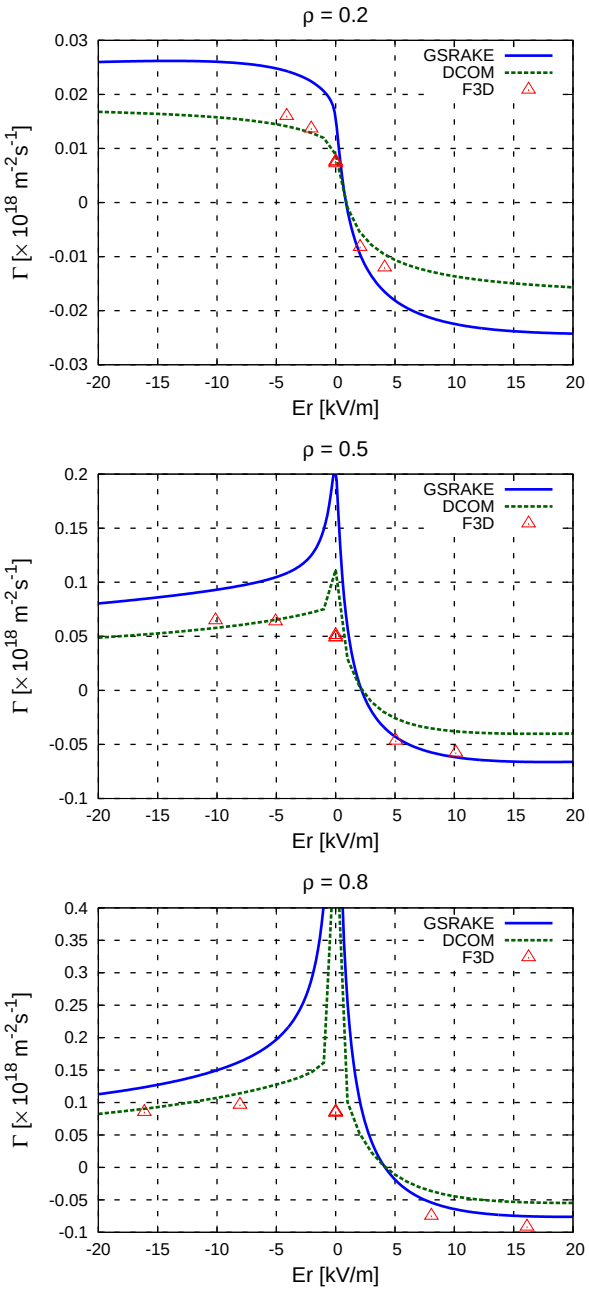

Figure 4.7: Electron particle flux on various magnetic surfaces ($\rho = 0.2$, 0.5, and 0.8 from top to bottom) for case (1) calculated by FORTEC-3D (F3D, triangles), GSRAKE (solid line), and DCOM/NNW (dashed line) are shown as a function of E_{r}.

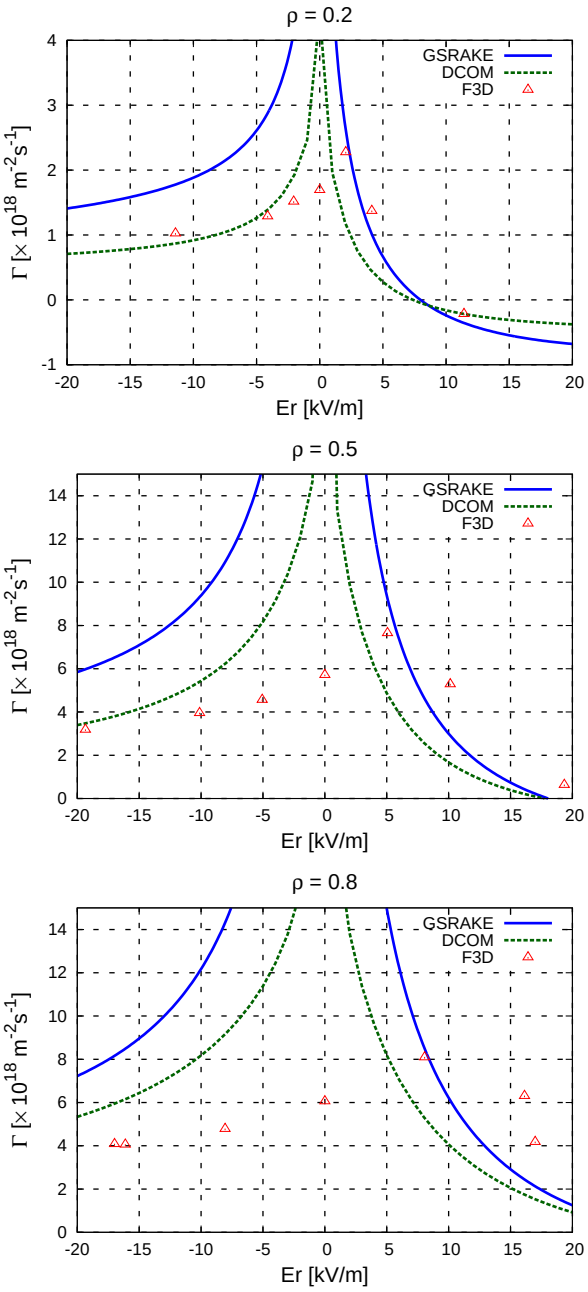

Figure 4.8: Electron particle flux on various magnetic surfaces ($\rho = 0.2$, 0.5, and 0.8 from top to bottom) for case (2) calculated by FORTEC-3D (F3D, triangles), GSRAKE (solid line), and DCOM/NNW (dashed line) are shown as a function of $E_{\rm r}$.

$\simeq 1.28$ cm for case (2). These two cases are both in the low-collisionality regime, so that the difference of the radial drift directly affects neoclassical transport. It is noted that the parameters of the case (2) plasma correspond to a typical CERC plasma, that is, the plasma with the high T_e and the low density.

4.5.2 Comparison among FORTEC-3D and local neoclassical transport codes

The evaluated electron particle flux are shown in Fig. 4.7 for case (1). The results for case (1) well reproduce the curve of the flux dependence on E_r, although the peaked Γ_e profile of GSRAKE and DCOM/NNW around $E_r = 0$ make it different from that obtained by FORTEC-3D, especially in plasma outer region (see $\rho = 0.8$ case of Fig. 4.7). This is the similar feature as in the benchmark calculation described in the previous section, that is, the flux value obtained by GSRAKE and DCOM/NNW has a maximum value at $E_r = 0$ in general, while FORTEC-3D results show no such a peak for these low temperature plasmas of $T_e(0) = 1.0$ keV. It is noted that the peaked particle flux at $E_r = 0$ in the local numerical codes reflects the fact that the poloidal resonance [64] occurs when $\boldsymbol{E} \times \boldsymbol{B}$ rotation vanishes at $E_r = 0$ since the poloidal rotation in local neoclassical theory is entirely due to the $\boldsymbol{E} \times \boldsymbol{B}$ drift. The reduction of the particle flux at the poloidal resonance seen in FORTEC-3D results is discussed later in this section. With this simulation, we confirm that this extended FORTEC-3D can calculate flux value for low collisional plasmas in reasonable agreement with that by GSRAKE and DCOM/NNW except for $E_r = 0$.

On the other hand, FORTEC-3D results for case (2) have a clear peak around small positive E_r as seen in Fig. 4.8. One also finds in Fig. 4.8 that the flux calculated by both GSRAKE and DCOM/NNW has a maximum value at $E_r = 0$. As a result, this makes qualitatively a significant difference in Γ_e between FORTEC-3D and the other two codes.

The reason why the flux obtained by FORTEC-3D has a peak at positive E_r is that it involves ∇B and curvature drift and takes poloidal resonance effect into account due to the balance between $\boldsymbol{E} \times \boldsymbol{B}$ drift and ∇B and curvature drift. In the local neoclassical theory, the poloidal precession resulting from ∇B and curvature drift is considered to be much smaller than that from $\boldsymbol{E} \times \boldsymbol{B}$ drift, namely $\omega_{\boldsymbol{E}\times\boldsymbol{B}} \gg \omega_B$ is assumed. Thus, as described above, the poloidal motion of particles arises from $\boldsymbol{E}\times\boldsymbol{B}$ drift dominantly, where $\omega_{\boldsymbol{E}\times\boldsymbol{B}}$, and ω_B denote the poloidal precession frequencies

through $\boldsymbol{E} \times \boldsymbol{B}$ drift and ∇B and curvature drift, respectively. The ripple-averaged drift kinetic equation which GSRAKE adopts includes the poloidal components of ∇B and curvature drift. However, the term corresponding to those drift is turned off in GSRAKE calculations. Also in DCOM/NNW, this effect is not completely taken into account since it uses particles of significantly small velocity. Therefore, the absence of the poloidal component of ∇B and curvature drift in both GSRAKE and DCOM/NNW leads the particle flux to have a peak at $E_\mathrm{r} = 0$. The ω_B term increases as T_e increases, however, the effect of the poloidal precession results in the shifted peak position in the electron neoclassical flux as shown in Fig. 4.8. Therefore, it is necessary of the effect to be included even for the electron neoclassical transport calculations as is done in FORTEC-3D.

The particle flux obtained by FORTEC-3D shows a clear reduction even when the poloidal resonance occurs as seen in Fig. 4.8. Γ_e for case (1) also shows no peak for any E_r in Fig. 4.7. It suggests that the electrons experience the collisionless detrapping arising from the particle transition from the helically trapped state to passing one due to the finite orbit width effect. This is understood as the following way: in the local neoclassical theory the peaked value of Γ_e at the poloidal resonance follows from the fact that the resonant (trapped) particles which cause the large neoclassical transport remain in the trapped state as long as the collision interrupts the trapped particles to be detrapped. If the finite orbit width effect exists, however, a helically-trapped particle can be move radially and the depth of the magnetic field ripple experienced by the trapped particle changes due to the radial motion of the particle. It leads to the change of the $\partial B/\partial r$ term appearing in the poloidal drift. As a result, the poloidal resonance of the particle breaks down and the particle changes into the passing state, that is, the collisionless detrapping occurs. It is considered that the large contribution to the neoclassical transport from the resonant particles, which is predicted in the local neoclassical theory, is reduced by the detrapping due to the radial drift.

The electron neoclassical flux given by FORTEC-3D indicates a relatively small value for all E_r cases at the outer surfaces. The population of trapped particles increases toward the outer region because of the larger magnetic field ripple there. It causes the increase in the neoclassical flux of local codes due to the absence of the collisionless detrapping. This fact indicates that non-local treatment for neoclassical transport without conventional assumptions is required even for electrons, since the radial excursion of a particle from the initial magnetic surface plays an important role. It enables ones to determine the particle flux accurately and then E_r by the ambipolar

condition for high electron temperature plasmas, e.g., CERC.

Consequently, it is shown that the non-local effect of electrons becomes important by the numerical results for low collisional and high T_e plasmas, where the radial deviation of helically trapped electrons from a certain magnetic surface increases, since the finite orbit width effect along with the poloidal motion of particles can result in a shifted peak in Γ_e at small positive E_r. It is noted that energy flux obtained by FORTEC-3D also show the same tendency as particle flux, that is, it has a peak around positive E_r not at $E_r = 0$, while that calculated by GSRAKE or DCOM/NNW has a peak at $E_r = 0$. It is concluded that the neoclassical transport for electrons needs to be calculated taking the finite orbit width effect into account for high T_e plasmas, since in such plasmas radial drift of helically trapped particle becomes larger so that non-locality of such a particle can contribute to the particle and energy flux.

4.6 Summary and discussion

In a CERC plasma, the ion temperature remains very low and it would not vary during the plasma discharge as well as ion particle flux. It becomes very important to calculate the electron particle flux accurately in order to determine the radial electric field and investigate its transition and/or bifurcation phenomenon observed in CERC plasma, since the electron particle flux plays an important role in determining whether the ion-root or the electron-root E_r is realized in the plasma. To determine the radial electric field self-consistently in high electron temperature plasmas, which is the motivation of this study, the ion particle flux as well as that of electron is required for ambipolar condition. However, simultaneous calculations of both electrons and ions by FORTEC-3D need much computational time, we here roughly estimate the ambipolar E_r and the resultant ambipolar particle flux from the steady-state ambipolar condition of $\Gamma_i^D = \Gamma_e^F$, where superscripts of D and F denotes the particle flux calculated by DCOM/NNW and FORTEC-3D, respectively.

As an example, we take the same plasma used in the previous section of the low collisionality regime (the plasma mentioned by case (2) in the low collisionality calculations), since it has the relatively high T_e ($T_e = 5$ keV) at the core and it is considered to be in the CERC-relevant parameter regime. The results are shown in Fig. 4.9 (a) for the ambipolar E_r. It is noted that the values shown by FORTEC-3D is obtained by $\Gamma_i^D = \Gamma_e^F$ while ones by DCOM is obtained by $\Gamma_i^D = \Gamma_e^D$. Multiple values of E_r are seen in this figure and they correspond to the electron root, unstable root, and ion root from

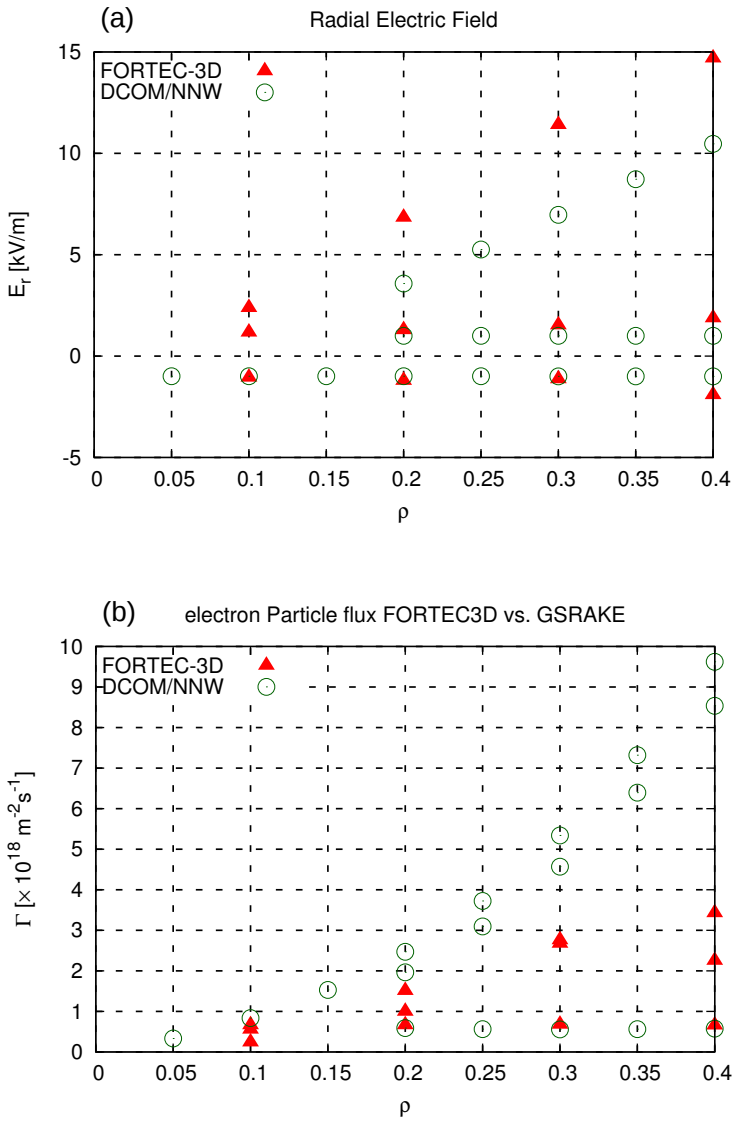

Figure 4.9: (a) The ambipolar E_{r} profile obtained from $\Gamma_{\mathrm{i}}^{\mathrm{D}} = \Gamma_{\mathrm{e}}^{\mathrm{F}}$ denoted by FORTEC-3D (red triangles) and $\Gamma_{\mathrm{i}}^{\mathrm{D}} = \Gamma_{\mathrm{e}}^{\mathrm{D}}$ denoted by DCOM/NNW (green circles) are shown respectively. (b) The ambipolar particle flux corresponding to the ambipolar E_{r} above is shown.

upper one to lower one, respectively. It is also noted that the existence of the electron-root E_r in this region shows the CERC-like character of this plasma parameter. While ion-root and unstable-root E_r is almost the same between E_r by FORTEC-3D and those by DCOM/NNW, electron-root E_r by FORTEC-3D shows larger values than those by DCOM/NNW. In addition, the electron-root E_r predicted at $\rho = 0.1$ in FORTEC-3D is not seen from the DCOM/NNW result. It indicates that the resultant ambipolar E_r including the electron drift is different from that calculated based on the local neoclassical theory. This results in the significant difference in the evaluation of the ambipolar E_r between local and non-local neoclassical transport calculations.

In Fig. 4.9 (b), the ambipolar particle flux is also shown. As in the Fig. 4.9 (a), the multiple values are obtained at some positions and they correspond to the valued of the ion-root, unstable-root, and electron-root ones respectively. On the contrary to the ambipolar E_r, the ion-root particle flux and unstable-root one show the difference between that by FORTEC-3D and by DCOM/NNW although the ion-root and unstable-root E_r is almost the same for both calculations. Since the ion-root and unstable-root E_r exists in the relatively small $|E_r|$ near $E_r = 0$ compared to the electron-root one and Γ_i^D changes sensitively around $E_r = 0$, the resultant ambipolar particle flux corresponding to ion root and unstable root is greatly affected by the slight difference of E_r between that obtained by FORTEC-3D and by DCOM/NNW. On the other hand, electron-root particle flux shows little difference in these calculations despite the difference of electron-root E_r between FORTEC-3D and DCOM/NNW. It reflects the fact that the particle flux does not vary as E_r changes at the larger $|E_r|$ where the electron-root E_r exists so that the electron-root particle flux calculated by FORTEC-3D and DCOM/NNW remains almost the same.

With these estimations above, it is suggested that the evaluation of the ambipolar E_r especially for the electron-root E_r requires to take electron drift into account since it expects an electron-root E_r which is not expected by the local neoclassical transport calculation when T_e is sufficiently high. Further application is needed to investigate the electron drift effect on the ambipolar condition and will be performed in the future.

As a summary, to evaluate the electron neoclassical transport rigorously, FORTEC-3D code has been extended to be applicable for electrons. In this extended FORTEC-3D code, the collision term involving electron-ion pitch angle scattering is introduced. This allows us to calculate the electron neoclassical particle and energy flux from the drift kinetic equation without assumptions made in the conventional neoclassical theory and numerical codes, namely, the finite orbit width effect rigorously for electrons

is included in FORTEC-3D.

It is shown that the particle and energy flux calculated by this extended FORTEC-3D for electrons depend not so much on the number of Fourier components of magnetic field of LHD $R_{\rm ax} = 3.6$ m configuration, if 12 or more Fourier components are used. This indicates that higher mode number spectra given by VMEC code have small effect on simulation results since most of those components have negligibly small value. Afterward, the benchmark calculations have been carried out using the extended FORTEC-3D code for electrons. The evaluated electron flux is compared to those obtained by GSRAKE and DCOM/NNW. It is noted that two codes calculate neoclassical particle and energy flux numerically under the assumptions of the local neoclassical theory, which neglect the radial drifts of particles from the initial magnetic surfaces. The results show reasonably a good agreement for a low temperature plasma with $T_{\rm e}(0) = 1.0$ keV for LHD $R_{\rm ax} = 3.60$ m magnetic configuration. This calculation condition corresponds to the situation that non-local treatment for neoclassical transport is not so important due to the low temperature and the LHD σ-optimized configuration. It is clearly shown that flux obtained by FORTEC-3D reproduces that by GSRAKE and DCOM/NNW with various radial electric fields on various magnetic surfaces. This provides a sufficient basis for the extended FORTEC-3D to be applicable to electrons properly.

Then FORTEC-3D calculations have been performed for lower collisional plasmas. For a low collisionality with low temperature plasma, the particle flux dependence on $E_{\rm r}$ by FORTEC-3D again agrees well with those obtained by GSRAKE and DCOM/NNW. With these calculations, it is verified that the numerical results of FORTEC-3D for electrons in low-collisionality regime unless the temperature becomes high. On the other hand, for the case of the low collisionality with higher temperature, e.g., $T_{\rm e} = 5.0$ keV at the core region, the calculation results show significant difference between FORTEC-3D code and the others, especially, for the small $E_{\rm r}$ cases. Neoclassical particle flux obtained by GSRAKE and DCOM/NNW has a maximum value at $E_{\rm r} = 0$ as in the previous calculations, while peak position of $\Gamma_{\rm e}$ from FORTEC-3D moves toward positive $E_{\rm r}$. It is considered that this change is attributed to the effect of poloidal drift which is determined by the balance between ∇B and the curvature drift and $\boldsymbol{E} \times \boldsymbol{B}$ one, since the effect of the former drift is not sufficiently taken into account in GSRAKE and DCOM/NNW calculations. Therefore, we can conclude that the finite orbit width effect and the poloidal motion of particles can result in a definite contribution to the neoclassical particle and energy flux in the high $T_{\rm e}$ plasma, where

a large radial drift of a helically-trapped particle exists.

It is suggested that the contribution of the helically-trapped particle to the particle flux is prevented due to the collisionless detrapping processes caused by the radial drift in high T_e plasmas. A detailed analysis for the effect of the particle detrapping on neoclassical transport particle flux remains the future task. To evaluate the finite orbit width effect of electrons in more detail, it is required to investigate which types of particles in helical devices contribute to neoclassical flux substantially since the finite orbit width depends on the particle orbit, which involves not only the helically trapped and the passing as discussed above but also other complicated states. The knowledge of the particle orbit may tell us a plausible way to improve the confinement property furthermore from the viewpoint of electrons and then the neoclassical ambipolar radial electric field. This will be also examined in the future.

Finally, we describe the practical application of FORTEC-3D expected to be performed for an experimental analysis for CERC plasmas. In the previous works, FORTEC-3D has calculated only the ion particle flux, Γ_i and determined E_r solving its time evolution equation by using E_r-Γ_e table obtained by GSRAKE. Now that FORTEC-3D can be applicable to electrons, we can calculate E_r as the solution of the initial value problem of the ambipolar condition. Whether the ambipolar E_r as obtained in this way is different from that obtained by the local neoclassical theory will be investigated in the practical applications of FORTEC-3D for the experimental CERC plasmas in the near future. In addition to that, since the balance between the electron heat flux and the electron heating is considered to be attributed to the formation of eITB in CERC plasmas, the discrepancies, or shifted peak in energy flux calculation between FORTEC-3D and the conventional numerical neoclassical transport codes is regarded as an important factor to investigate the formation of transport barrier.

Chapter 5

Application of FORTEC-3D to Experimental Analysis

5.1 Introduction

Recent years, Core Electron Root Confinement (CERC) plasmas have been obtained in several helical devices. These plasmas are characterized by their high electron temperature, steep T_e gradient called electron Internal Transport Barrier (eITB) in the core region. Especially, high $T_e \simeq 20$ keV is achieved in recent LHD experiments with electron cyclotron heating (ECH) [36]. In such high temperature with the steep T_e gradient and the low collisionality plasmas, helically-trapped electrons drift radially far from a certain magnetic surface. Thus, it is required to evaluate its neoclassical transport taking the electron drift into account. It is considered that the FOW effect of electrons in the high T_e plasmas affects its particle and energy transport significantly.

In addition to these features, it is observed in LHD experiments that the transition of the radial electric field from a weak negative value (ion root) to a strong positive one (electron root) occurs when a CERC plasma is formed. The radial electric field in helical devices is predominantly determined by the ambipolar condition which states that E_r arises to balance the particle flux of electron and ion, namely, the radial current due to the neoclassical radial transport vanishes at the steady state. Therefore, a self-consistent analysis of the radial electric field and the neoclassical particle and energy flux is the key issue in helical plasmas.

The neoclassical radial electric field has been so far analyzed by the conventional numerical codes such as GSRAKE, DCOM/NNW, *etc.*, which is based on the local

assumptions. While the ion particle flux with the finite orbit width effect and its influence on the E_r formation have been investigated intensively in recent years [47,73], the effect of electron drift has not been paid so much attention. However, since the electron particle flux is changed qualitatively by the electron FOW effect and the poloidal motion as seen in the previous chapters, it can in turn influence the radial electric field formation. Thus, taking the electron drift into account allows one to evaluate the ambipolar radial electric field more accurately.

This is the first time to examine the ambipolar radial electric field of the experimental plasma taking the electron FOW effect into account. In Section 5.2, we discuss the ambipolar condition and the electron finite orbit width effect on it. In this section, we describe two approaches to calculate the radial electric field using FORTEC-3D as the steady-state solution of the ambipolar condition. Numerical results are presented in Section 5.3. A CERC plasma with the relatively low $T_e \simeq 3.5$ keV [15] observed in LHD is examined by FORTEC-3D. The radial electric field calculated by these two ways and compared to the experimental observations and the local calculation results. The radial electric field for a non-CERC plasma is also examined in this section. Finally in Section 5.4 the discussion on the Maxwell's construction [64] and the diffusive term on the radial electric field are presented before summarizing the results in this section. The discussion does not yet involve a definitive conclusion but seems to pose a beneficial viewpoint to be considered in the further application of FORTEC-3D to CERC plasmas in the future.

5.2 Ambipolar condition

From the Poisson's equation and the continuity equation, the time evolution of the radial electric field is expressed as follows [46];

$$\epsilon_0 \frac{\partial E_r}{\partial t} = -J_r, \tag{5.1}$$

where ϵ_0 is the permittivity and J_r denotes the radial current. J_r is composed of the inductive current from the classical polarization and that from the neoclassical particle flux, thus, J_r is rewritten as,

$$J_r = \epsilon_0 \left(\frac{c^2}{v_A^2} \right) \frac{\partial E_r}{\partial t} + \sum_a Z_a \Gamma_a, \tag{5.2}$$

where c and v_A is the speed of light and Alfvén velocity, respectively, and Z_a and Γ_a is the charge and the particle flux of a-th species. It is noted that the first term on

the left hand side in Eq.(5.2) denotes the classical polarization current. By using this relation, one can obtain the equation for the time evolution of $E_{\rm r}$ as follows;

$$\epsilon_0 \epsilon_\perp \frac{\partial E_{\rm r}}{\partial t} = -e \left(\Gamma_{\rm i} - \Gamma_{\rm e} \right) . \tag{5.3}$$

In Eq.5.3, $\epsilon_\perp \equiv \left(1 + \frac{c^2}{v_{\rm A}^2} \right)$ is used, where we assume that the plasma is composed of only electron and hydrogen ion ($Z = 1$) for simplicity. When $E_{\rm r}$ reaches the steady state, it can be easily seen that $\Gamma_{\rm e} = \Gamma_{\rm i}$ is accomplished. It is immediately understood that the particle flux of ion and electron must be balanced to vanish the radial current at the steady state. It can be restated that the charge quasi-neutrality of the radial (neoclassical) current is accomplished by the radial electric field which is spontaneously formed. What is important is that the ambipolar condition is a constraint for a radially local neoclassical particle flux. The ambipolar radial electric field is determined locally at each magnetic surface by the ambipolar condition. A schematic view for the ambipolar condition is shown in Fig. 5.1. As seen in this figure, even if the ambipolar condition is satisfied only for the ion-root radial electric field in the local neoclassical transport theory, the multiple-root radial electric field can appear as the solution of the ambipolar condition taking the finite orbit width effect into account in the electron neoclassical transport calculation. Although it is not necessarily the case for any plasmas, the situation suggests the possibility that the finite orbit width effect on the electron neoclassical transport changes the ambipolar radial electric field through the ambipolar condition.

Simultaneous computation of $\Gamma_{\rm e}$ and Γi in a self-consistent manner with the time evolution of $E_{\rm r}$ requires huge computational time and memory, and it is impossible to implement such a calculation at this point. Thus, we refer to a $\Gamma_{\rm i} = \Gamma_{\rm i}(\rho, E_{\rm r})$ data base from a DCOM/NNW result as the ion particle flux in the following calculations to reduce the required computational resource. Although $\Gamma_{\rm i}$ calculated by DCOM/NNW does not sufficiently include the finite orbit width effect for ions, $T_{\rm i}$ in the CERC plasmas is generally low enough so far that it is considered that FOW effect for ions has little influence on $\Gamma_{\rm i}$. Following two options are examined to evaluate $E_{\rm r}$ at the steady state.

1. Evaluate $\Gamma_{\rm e}$ with the various *temporally-fixed* $E_{\rm r}$ by using FORTEC-3D, and then find the solution that satisfies $\Gamma_{\rm e} = \Gamma_{\rm i}$.

2. Evaluate $\Gamma_{\rm e}$ at each time step with solving eq.(5.3) with an initial condition of $E_{\rm r}$ and then steady state solutions of $E_{\rm r}$ and $\Gamma_{\rm e}$ are obtained at the same time.

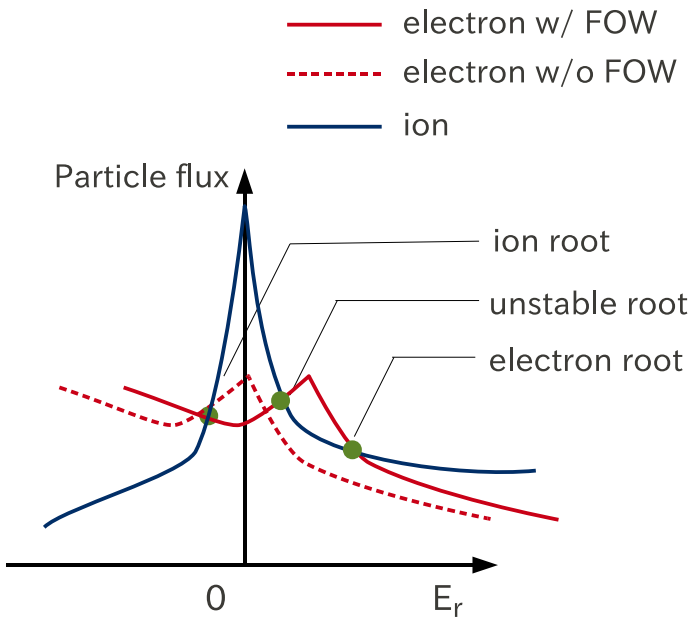

Figure 5.1: Schematic view of the ambipolar condition that satisfies $\Gamma_e = \Gamma_i$. Γ_e evaluated by taking the finite orbit width effect into account is shown by the solid red curve, while Γ_e without the finite orbit width effect is shown by the dashed red curve. Γ_i is shown by the solid blue line.

Simulation results of the ambipolar E_r in these two ways are compared to those obtained by experimental observations and the previous local numerical calculations.

5.3 Radial electric field analysis by FORTEC-3D

We apply FORTEC-3D to a CERC plasma for the first time to examine the radial electric field in the high T_e plasma with including the electron drift orbit. A relatively low electron temperature CERC plasma of $T_e \simeq 3.5$ keV [15] is chosen for some reasons. One is that the radial electric field of the plasma is observed experimentally. The second is that we have already benchmarked the electron neoclassical transport of FORTEC-3D for a plasma with the comparable electron temperature of $T_e = 5$ keV in Chapter 4. Since it is the first time to examine the radial electric field of the experimental

plasma including FOW effect of electron, it is appropriate to choose the plasma having the feature above. Another advantage of this choice of the low T_e CERC plasma is to reduce the computational burden since this enables one to choose the simulation time step as large as in the previous chapter.

Three kinds of simulation are implemented in this section. First, we apply FORTEC-3D to the CERC plasma and estimate the radial electric field with the temporally-fixed E_r: the procedure corresponds to the way referred to as (1) in Sec. 5.2. Second, the time evolution of the radial electric field is solved simultaneously with the electron particle flux by FORTEC-3D. This is the way of (2) in the previous section. We make comparison among FORTEC-3D, other local calculation results, and experimental observations for each case. Finally, we implement a FORTEC-3D simulation for a non-CERC plasma and find a time-dependent solution of the radial electric field.

5.3.1 Steady state ambipolar condition

In this subsection, we illustrate the simulation results of FORTEC-3D for the temporally-fixed radial electric field. This enables ones to estimate the steady-state ambipolar E_r without solving the time evolution of the radial electric field. To obtain the steady-state ambipolar E_r, we need to evaluate the electron particle flux as a function of the radial electric field at each magnetic surface.

The discharge of #32940 at $t = 2.0$ sec from the LHD experiment is picked up as an example and the parameters of the plasma are shown in Fig. 5.2. This is the typical CERC plasma profile since it has steep gradient of T_e and moderately high T_e in the plasma core. Fourier spectrum for the equilibrium magnetic configuration of LHD $R_{ax} = 3.75$ m and $\beta = 0.01$ % is obtained by VMEC code [72]. It is noted that 12 Fourier components of the magnetic field is used in the calculation.

The radial electric field profile used in FORTEC-3D calculations are shown in Fig. 5.3. FORTEC-3D is applied to the plasma shown in Fig. 5.2 with each fixed E_r profile. The calculated electron particle flux are shown in Fig. 5.4 at various radial positions. To investigate the ambipolar condition, Γ_i calculated by DCOM/NNW is shown in Fig. 5.4. Also Γ_e from DCOM/NNW is shown for the reference purpose in this figure. It is noted that Γ_e averaged over 0.3 τ_{ei} at the steady state obtained for each E_r is shown in this figure. It is found that the resultant Γ_e from FORTEC-3D calculations show the difference from that of DCOM/NNW especially in the core region of $\rho < 0.2$. The steady-state E_r is estimated using this figure with the ambipolar condition of $\Gamma_e = \Gamma_i$.

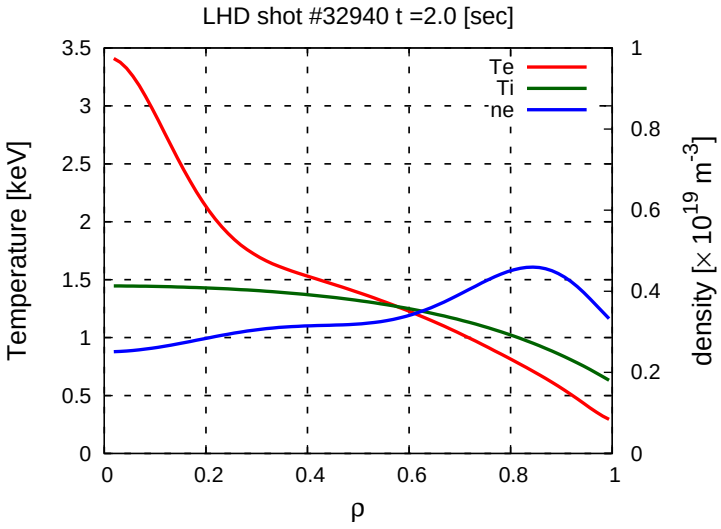

Figure 5.2: Plasma profiles of the CERC discharge in LHD (#32940 at $t = 2.0$ sec).

The radial profile of the ambipolar E_r is shown in Fig. 5.5. It is clearly shown that the estimated ambipolar E_r is almost the same as that of DCOM/NNW calculation over the whole plasma region. It is noted that the radial electric field of FORTEC-3D is estimated from only five values of Γ_e (see Fig. 5.4) so that it is just a very rough estimation. No clear difference of the ambipolar E_r between by FORTEC-3D and by DCOM/NNW is seen from this figure. This suggests that the electron drift has little effects on the resultant E_r at least for the plasma of $T_e \simeq 3.5$ keV, while it affects on the electron particle flux especially for the small radial electric field.

This is explained as follows. The electron particle flux is calculated for a fixed radial electric field. In this situation, the electron particle flux of FORTEC-3D can differ from that of DCOM/NNW at the relatively small radial electric field, namely, around $E_r \simeq 0$ as is shown in Chapter 4 (see Fig. 4.8). The difference arises from the finite orbit width effect and the poloidal motion of electrons, both of which are included in FORTEC-3D as the non-local effect. However, the effects decrease with the large radial electric field due to the large $\boldsymbol{E} \times \boldsymbol{B}$ drift and the electron particle flux is predominantly determined by the radial electric field. Thus, the FOW effect and the poloidal motion in FORTEC-3D does not influence on the electron particle flux for the large radial electric field. The electron-root E_r in a high T_e plasma in general has a large value, so that the non-locality has little effect on the electron particle flux in this case. The electron-root E_r determined by FORTEC-3D results in almost the same

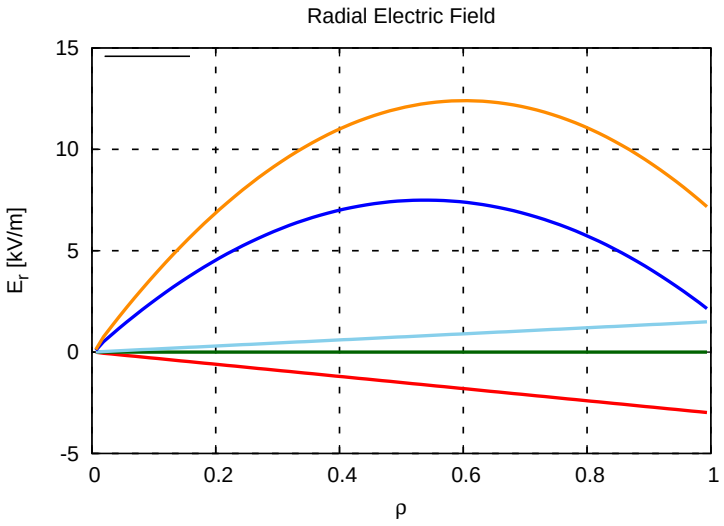

Figure 5.3: The radial electric field profiles used for the steady state analysis by FORTEC-3D calculation are shown. The electron particle flux is evaluated for each fixed $E_{\rm r}$ profile.

as that by DCOM/NNW. On the other hand, the ion-root and unstable-root radial electric field is located around $E_{\rm r} = 0$ and the ion particle flux which is calculated by DCOM/NNW has a strong peak around $E_{\rm r} \simeq 0$. The ion-root and unstable-root radial electric field, or the intersection of $\Gamma_{\rm e}$ and $\Gamma_{\rm i}$ is determined in accordance with the foot-point of the *ion* particle flux of DCOM/NNW. Even if we adopt either FORTEC-3D or DCOM/NNW as the electron particle flux, the resultant ambipolar ion-root and unstable-root $E_{\rm r}$ of FORTEC-3D and DCOM/NNW agree with each other due to the preponderance of the ion particle flux in determining them.

5.3.2 Time evolution of the radial electric field

FORTEC-3D can evaluate the time-dependent radial electric field with self-consistent calculation of the particle flux as a steady-state solution of Eq.5.3. So far, Satake *et al.* have performed such calculations with referring to a $E_{\rm r}$-$\Gamma_{\rm e}$ data base obtained by GSRAKE [45, 46, 73]. This makes it enable to evaluate the *ion* particle flux and the radial electric field.

In this thesis, however, we have to carry out the opposite procedure, that is, the *electron* particle flux and the radial electric field need to be evaluated using a $E_{\rm r}$-$\Gamma_{\rm i}$ data base. DCOM/NNW is adopted to make the data base since GSRAKE involves a

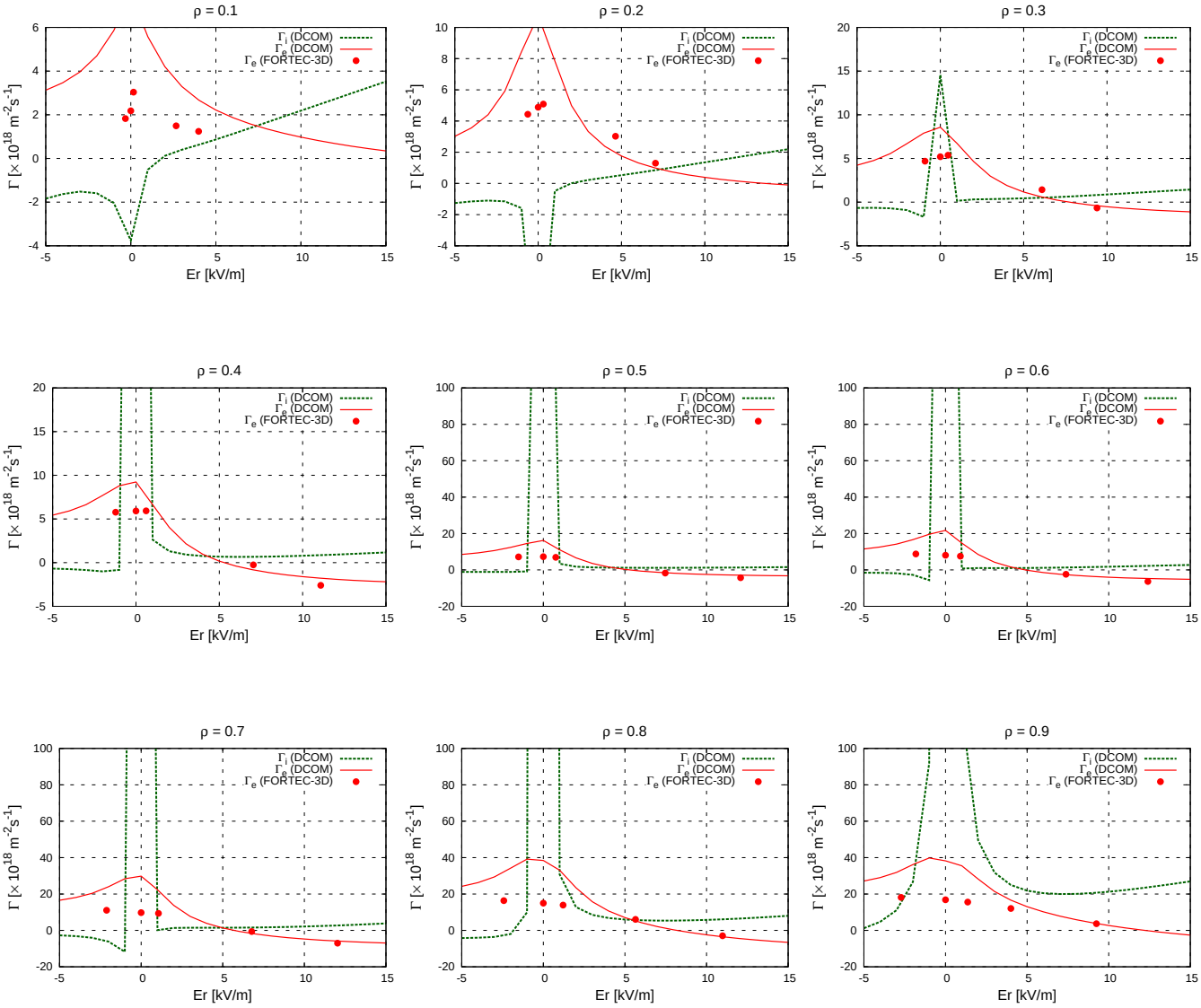

Figure 5.4: The Electron particle flux at the various radial positions obtained by FORTEC-3D with each E_r profile in Fig. 5.3. Also shown are Γ_i and Γ_e calculated by DCOM/NNW.

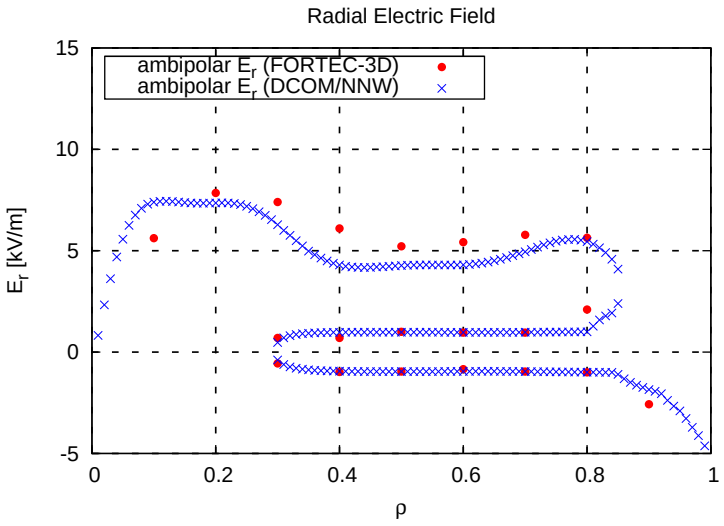

Figure 5.5: The ambipolar $E_{\rm r}$ estimated from $E_{\rm r}$-Γ tables obtained by the steady state calculation of FORTEC-3D (see Fig. 5.4).

significant difficulty in a calculation of the ion particle flux especially in the core region. The difficulty is discussed later in this section. To use the DCOM/NNW data base of $E_{\rm r}$-$\Gamma_{\rm i}$, we extend FORTEC-3D. Although DCOM/NNW calculates the ion particle flux based on the local assumptions which is inappropriate in high temperature plasmas as shown in the previous chapter, the ion temperature in a CERC plasma is generally low enough so far, thus the adoption of DCOM/NNW for the ion particle flux is justified due to the smallness of the ion FOW effect.

The number of test particles used is 20,480,000 and the time step of $\Delta t_{\rm c} = 10^{-4}\tau_{\rm ei}$ is adopted for the interval that the collision occurs for each marker particle, where $\tau_{\rm ei} = \nu_{\rm ei}^{-1}$ is the mean-free-time of electrons and $\nu_{\rm ei}$ is the collision frequency between electron and ion. The time step to solve the particle orbit, $\Delta t_{\rm o} = 10^{-2}\Delta t_{\rm c}$. The radial electric field is also calculated with the same time step as that of the particle orbit. It is noted that the time step of $\Delta t_{\rm o}$ is determined so that the typical orbit size of a marker particle is on the order of several 10^{-2} m, namely, $v_{\rm th}\Delta t_{\rm o} \sim 10^{-2}$ m.

Before applying FORTEC-3D to a CERC plasma, we illustrate the ambipolar $E_{\rm r}$ calculated by DCOM/NNW and GSRAKE as results of the local neoclassical calculation for the reference purpose. The ambipolar $E_{\rm r}$ and experimental observations are shown in Fig. 5.6. In Fig. 5.6 that experimental observations show a peaked profile in the plasma core while not peaked but flat profile is obtained by both DCOM/NNW and GSRAKE at $0.1 < \rho < 0.3$. The radial electric field obtained by DCOM/NNW

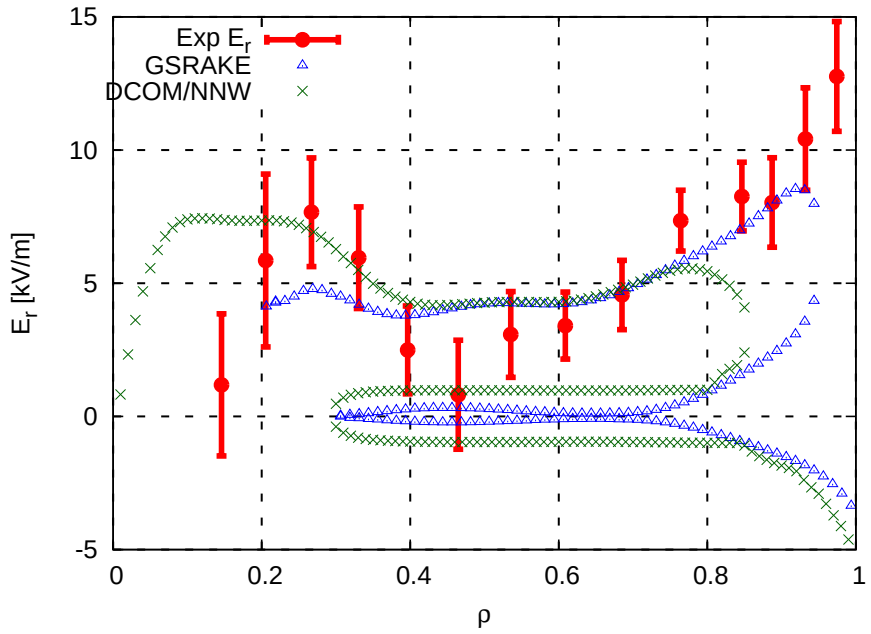

Figure 5.6: The steady-state ambipolar E_r obtained by GSRAKE, DCOM/NNW, and experimental observations.

results in the ion-root E_r in the plasma outer region while that calculated by GSRAKE shows the electron-root E_r at $\rho < 0.9$. It is noted that GSRAKE cannot obtain the ambipolar radial electric field in the core region of $\rho < 0.2$. This is because the poloidal Mach number for ions, $M_\mathrm{p,i} \equiv E_\mathrm{r}/B_\mathrm{p}v_\mathrm{th,i}$ exceeds unity, $M_\mathrm{p,i} > 1$, due to the largeness of the radial electric field and the smallness of the poloidal magnetic field, B_p. It violates the assumption of the drift ordering which assumes that the $\boldsymbol{E} \times \boldsymbol{B}$ drift is small enough. GSRAKE is based on the ripple-averaged drift kinetic equation involving the drift ordering, and thus, GSRAKE results in unphysical estimates for the ion particle and heat flux with such large radial electric field in the core region. This is the reason for which we cannot adopt GSRAKE results as the E_r-Γ_i data base in FORTEC-3D simulations.

The E_r-Γ_i data base obtained from DCOM/NNW for this plasma is shown in Fig. 5.7. It is noted that in DCOM/NNW calculation, $\beta = 0.0$ % is assumed. A clear peak around $E_\mathrm{r} = 0$ is seen in the whole plasma region of ρ due to the poloidal resonance and the large Γ_i also results in for the vast region of positive E_r at $\rho > 0.8$. FORTEC-3D calculates the neoclassical flux and the radial electric field for a given initial E_r profile using the data base. The initial E_r profiles used in the FORTEC-3D simulations are shown in Fig. 5.8. We use two initial profiles of E_r represented as $E_\mathrm{r}(\rho) = E_0\rho$ to

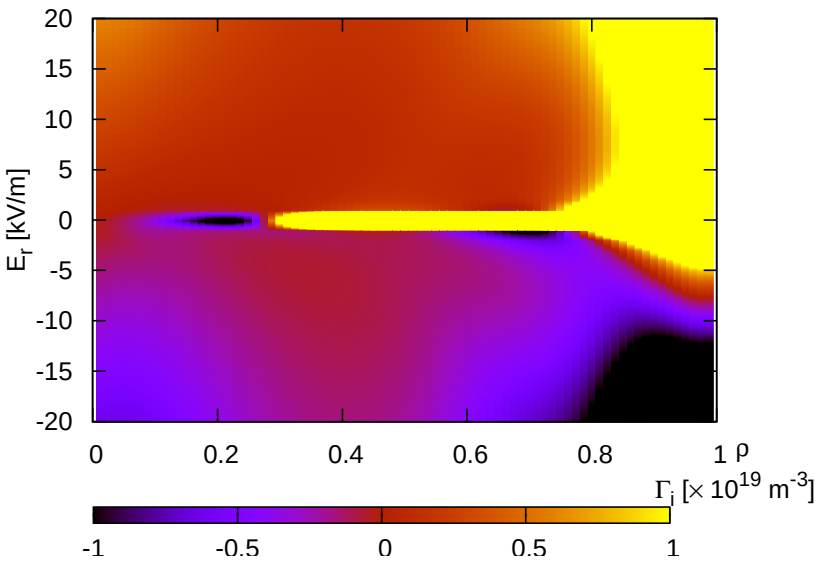

Figure 5.7: The E_r-Γ_i data base calculated by DCOM/NNW for the plasma profile of the LHD discharge #32940 $t = 2.0$ sec.

examine the initial value dependence of FORTEC-3D simulations. Hereafter, the case of $E_0 = 10$ and 20 are called case (1) and (2), respectively.

The time evolution of Γ_e and E_r for case (1) and (2) at the several magnetic surfaces, $\rho = 0.25$, 0.5, and 0.9 are shown in Figs. 5.9 and 5.10, respectively. This choice of the radial position corresponds to the core region of the peaked electron-root E_r, the intermediate region, and the edge region of ion-root one, respectively. It can be seen in these figures that the initial value of E_r does not affect the ambipolar E_r formation. It is also found in these figures that no geodesic acoustic mode (GAM) oscillation [73] occurs at every magnetic surface for both cases, although it has been observed in the previous FORTEC-3D simulation for ions. The electron particle flux balances the ion one after reaching the steady state at $t/\tau_{ei} \simeq 1.0$ for case (1) as shown in Fig. 5.9. The similar steady state is achieved for case (2) in Fig. 5.10. At the steady state, the radial current driven by the difference between the electron and ion particle flux, $\Gamma_i - \Gamma_e$, vanishes and then the ambipolar radial electric field is obtained. It is noted that an inevitable numerical noise of the electron particle flux resulting from Monte-Carlo method which uses the motion of a large number of marker particles and random collision processes to solve the drift kinetic equation exists. In the inner region of the plasma at $\rho = 0.25$ and $\rho = 0.5$, the radial electric field gradually changes to balance

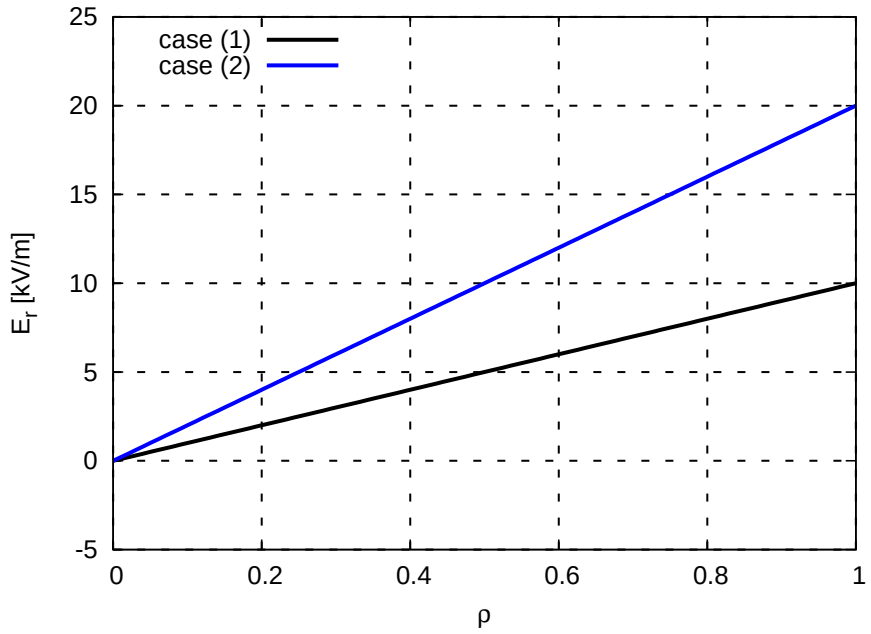

Figure 5.8: The initial radial electric field for case (1) and (2) used in the FORTEC-3D simulations.

the electron and ion particle flux and then reaches the steady state for both cases. In the outer region at $\rho = 0.9$, on the other hand, it drops rapidly to the ion-root E_r for both cases. This suggests that the interface around $\rho \simeq 0.75$ separates the behavior of E_r formation.

The radial profiles of E_r in steady state for case (1) and (2) are shown in Fig. 5.11(a) and (b). These are results both obtained by FORTEC-3D as steady-state solutions for the time evolution of the radial electric field. It is noted that E_r shown in Fig. 5.11(a) (case (1)) is averaged over 0.6 τ_{ei} at the steady state while that averaged over 0.4 τ_{ei} is shown for case (2) in Fig. 5.11(b). Error bars for E_r of FORTEC-3D results which are evaluated as its standard deviation from the averaged value at each radial position are also shown in these figures. One can see that the initial E_r profile does not much influence the steady-state E_r obtained by FORTEC-3D although the position of the interface where the electron-root E_r changes into the ion-root one varies a little.

At the intermediate region of $0.3 < \rho < 0.6$, the radial electric field and its shear obtained by FORTEC-3D show a relatively good agreement with the electron-root E_r by DCOM/NNW for both cases. However, E_r by FORTEC-3D differs largely from that by DCOM/NNW in the core of $\rho < 0.2$. The radial profile of Γ_e is shown in Fig. 5.12. It is shown in these figures that the difference of Γ_e becomes larger in the

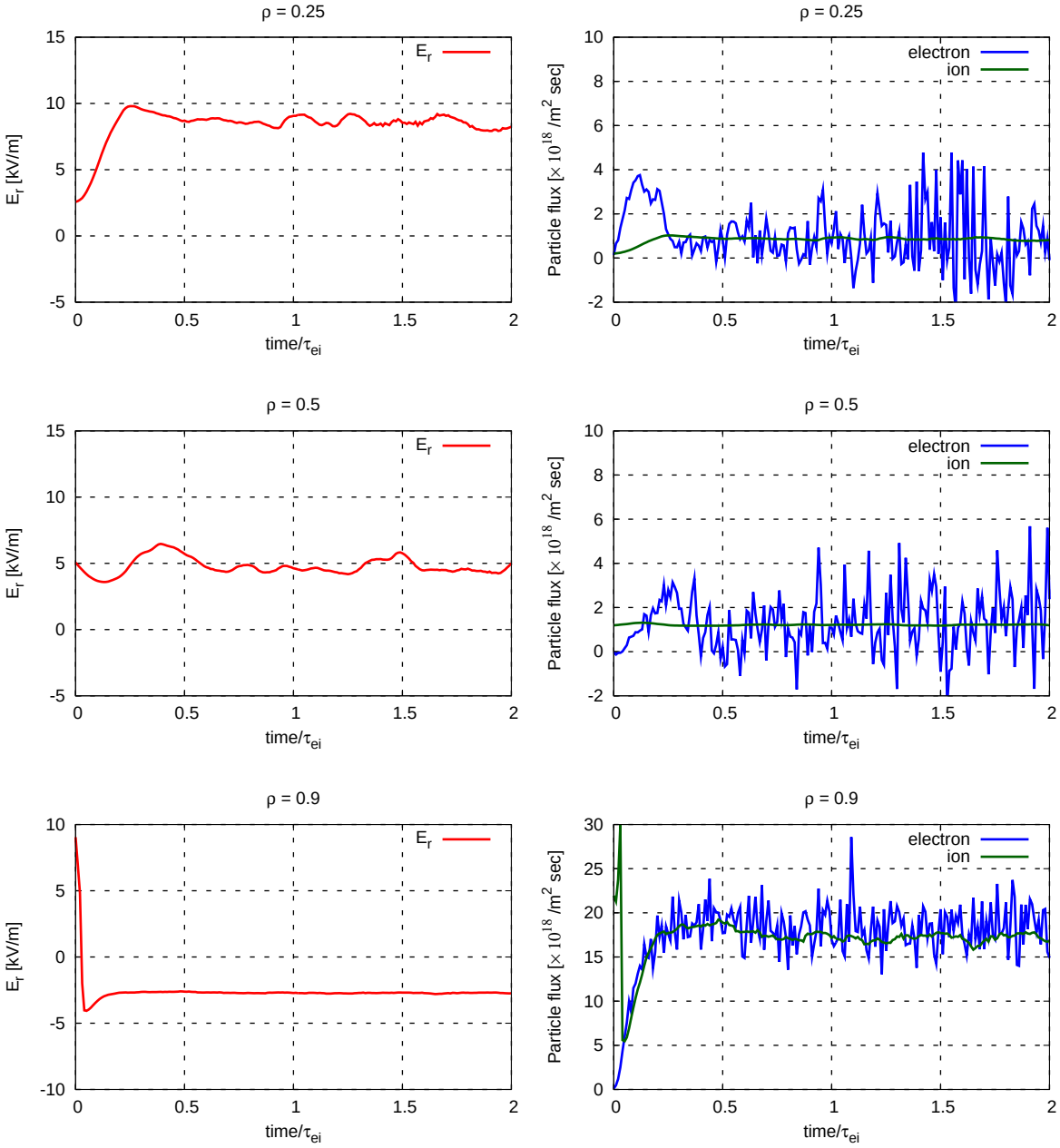

Figure 5.9: Time evolution of E_{r} and the electron particle flux for case (1) at various radial positions.

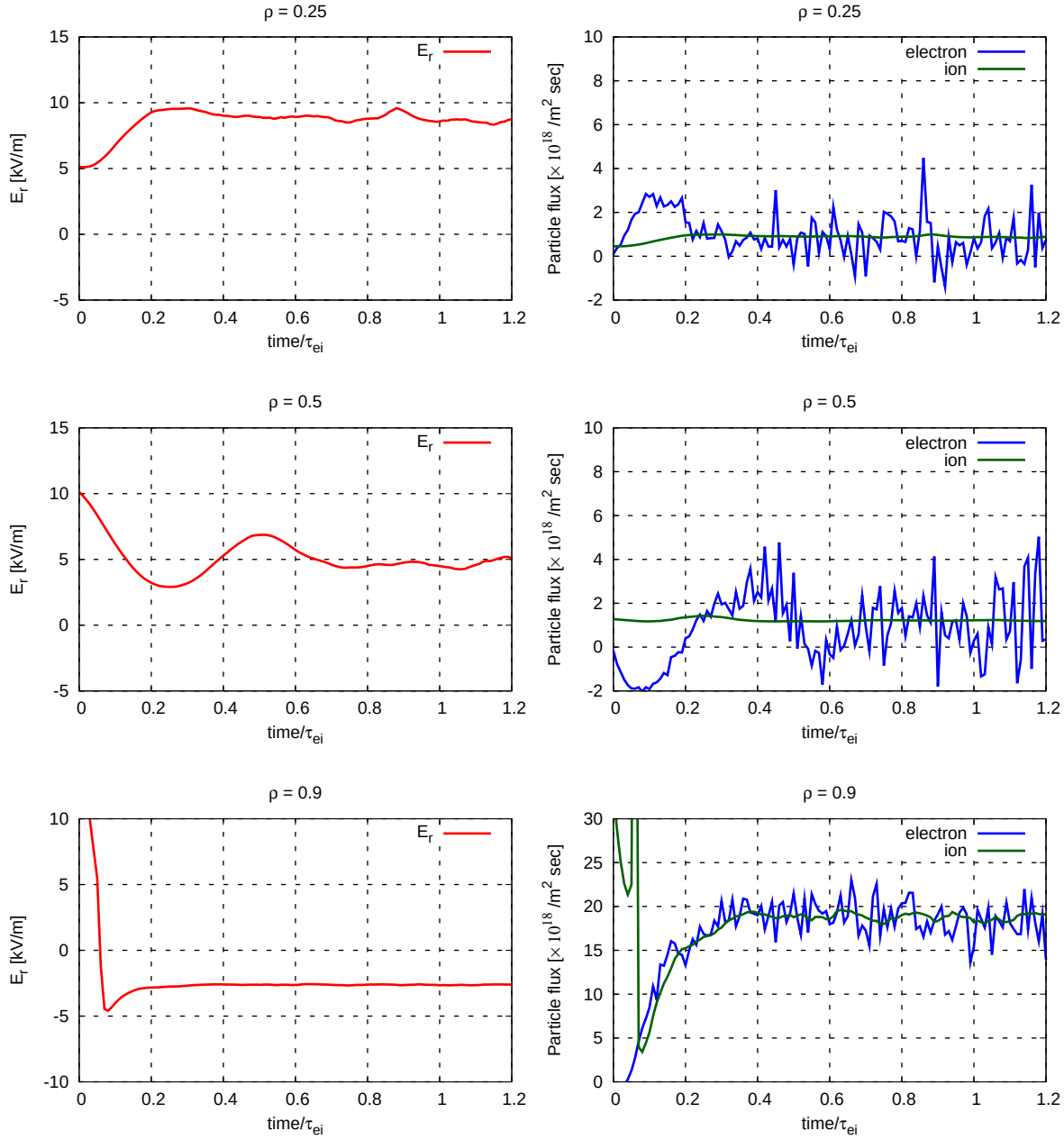

Figure 5.10: Time evolution of E_{r} and the electron particle flux for case (2) at various radial positions.

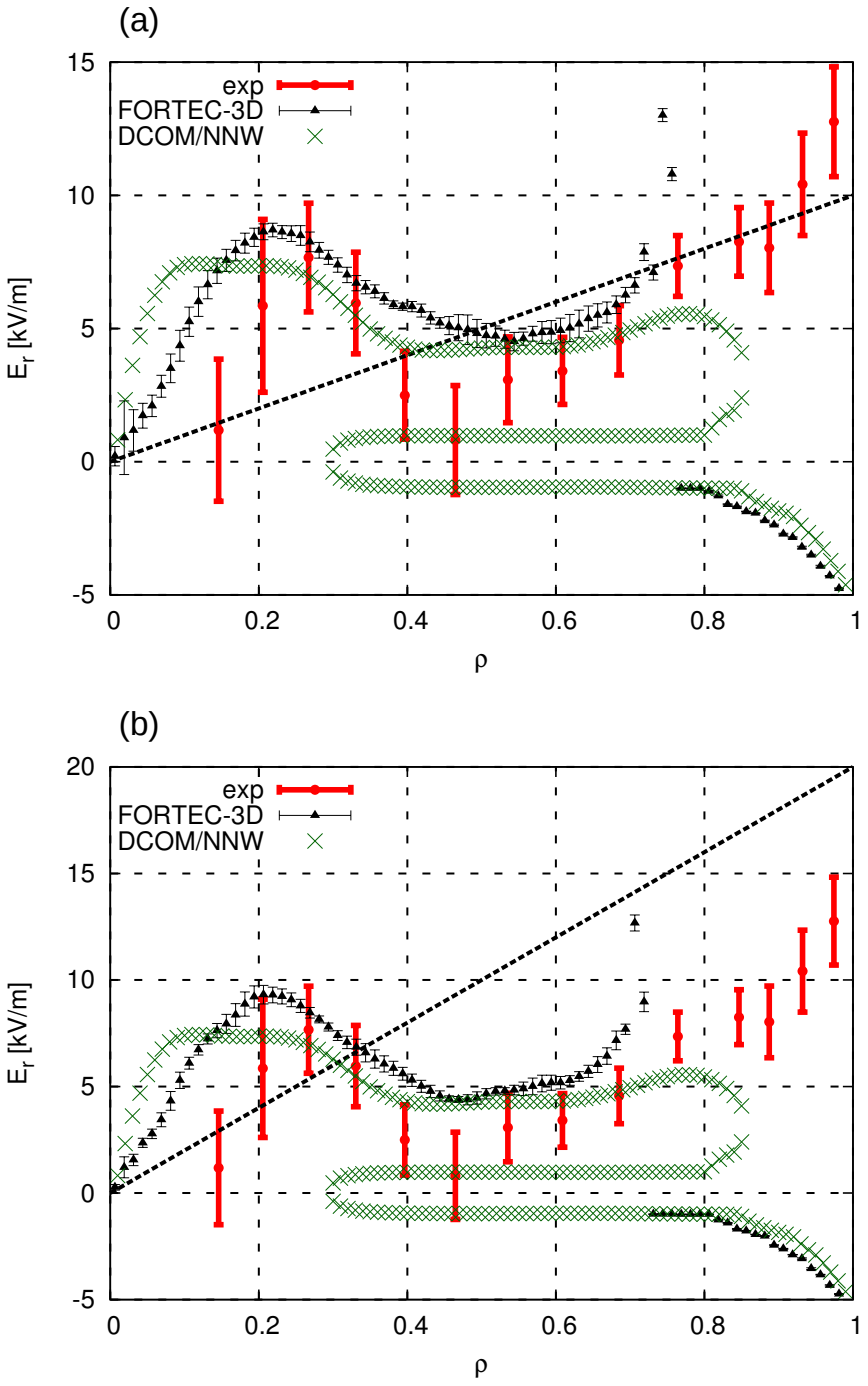

Figure 5.11: (a) The ambipolar E_r obtained by FORTEC-3D, DCOM/NNW, and experimental observations are shown for case (1) and (b) for case (2), respectively. Also shown by the dashed line is the initial profile of E_r for FORTEC-3D calculation.

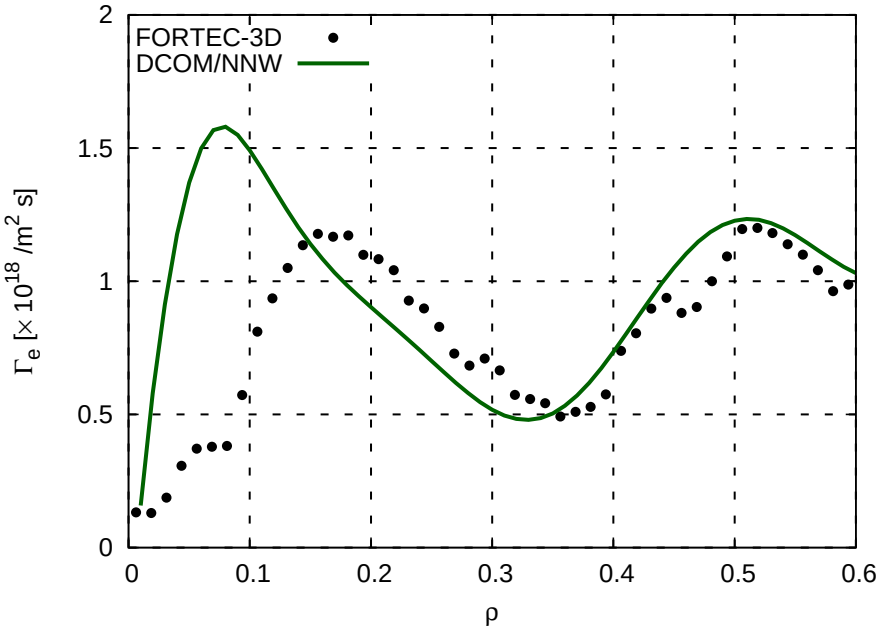

Figure 5.12: The radial profile of the electron particle flux obtained by FORTEC-3D and DCOM/NNW in the core region. It is noted that the DCOM/NWN results show the one corresponding to the electron-root E_r.

core region especially inside $\rho \simeq 0.15$ than that at the intermediate region of $\rho > 0.3$. The reason why the difference of Γ_e and E_r becomes larger in the core region than in the intermediate region is considered as follows. In CERC plasmas, a typical radial drift width becomes larger as the temperature increases, and the steep T_e gradient, or the small scale length of T_e arises in the core region. Thus the local assumption that the orbit width is small enough compared to the plasma scale length, would be inappropriate. Since ∇B and the curvature drifts, which are assumed to be small enough as the consequence of the local assumptions, become large as T_e increases, they change the neoclassical transport qualitatively through the particle poloidal precession and the collisionless detrapping as shown in Chapter 4. The FOW effect included in FORTEC-3D affects the neoclassical transport more in the core region where T_e of the CERC plasma is high and the steep T_e gradient forms. On the other hand, as stated above, DCOM/NNW evaluates the neoclassical transport flux based on the local assumptions. This suggests that the electron drift effect plays an important role in determining E_r in the core region.

In the edge region of $\rho > 0.75$, the ion-root E_r results in and it agrees well with the ion-root E_r obtained by DCOM/NNW in contrast to the experimental observation

of the electron-root E_r. One can find that the electron-root E_r cannot appear as the steady state solution of ambipolar condition, thus, this electron-root feature in the edge region may result from other physical mechanisms such as heating, charge exchange with neutral particles, *etc.*, which is not taken into account in both FORTEC-3D and DCOM/NNW. In addition to the physical reason above, the numerical boundary condition at $\rho = 1$ is accounted for the difference between FORTEC-3D and the experimental observations. It is noted that no diffusive terms on E_r except that arises numerically from Γ_e interpolation is included in FORTEC-3D simulation. It is inferred that the radial electric field rapidly increases at $\rho \simeq 0.75$ since the omission of diffusivity on E_r results in the numerical increase at the interface of the radial electric field bifurcation. Discussion on the diffusion term on E_r is presented in detail later in Sec. 5.4.

The parallel flow of poloidal and toroidal rotation may be also the reason of ion-root E_r in the edge region. In FORTEC-3D, although the poloidal and toroidal rotation which arise from the δf part of the particle distribution function are calculated, f_0, or the distribution function of the leading order is assumed to be the *stationary* Maxwellian. This means that no flow velocity which should be included in f_0 as the *shifted* Maxwellian is considered. Especially, the poloidal rotation which is the combination of the poloidal component of the $\boldsymbol{E} \times \boldsymbol{B}$ drift and the particle precession caused by the ∇B and the curvature drift may be significantly changed near the interface of the E_r bifurcation due to the smallness of E_r ($E_r = 0$ at the interface), so that the poloidal rotation may in turn affect the E_r formation. It is pointed out that the electron-root E_r appears at $\rho = 0.8$ as the result in the steady-state analysis performed in the previous subsection (see Fig. 5.5), while the bifurcation from the electron-root E_r to the ion-root one arises at more inner region in the time-dependent calculations, namely $\rho \simeq 0.75$ for case (1) and $\rho \simeq 0.7$ for case (2) as shown in Fig. 5.11.

5.3.3 Time dependent E_r analysis for a non-CERC plasma

The neoclassical transport and the ambipolar E_r is evaluated by FORTEC-3D for a non-CERC plasma. It is the same plasma (the discharge #32940) as in the previous subsection but at the different timing [15].

The parameter of this plasma is shown in Fig. 5.13. The main difference between this plasma and the CERC one shown in Fig. 5.2 is that the electron temperature in the core is much lower than the CERC one and no steep T_e gradient of eITB is formed. FORTEC-3D is applied to this plasma and the time-dependent E_r is evaluated as is

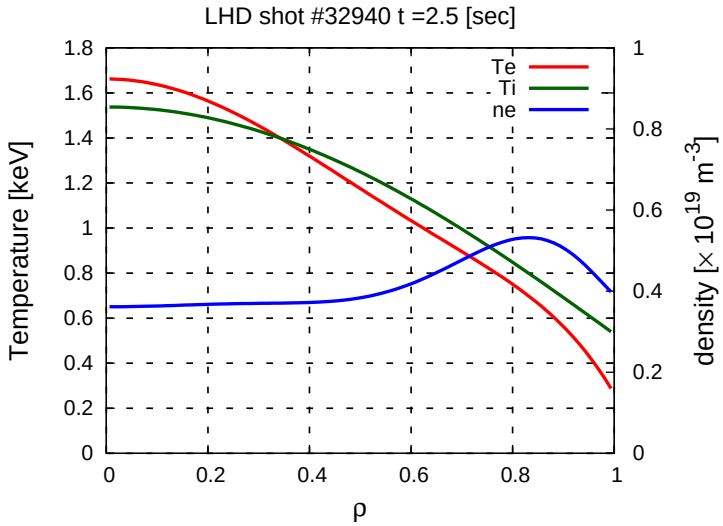

Figure 5.13: Plasma profiles of the non-CERC discharge in LHD (#32940 $t = 2.5$ sec).

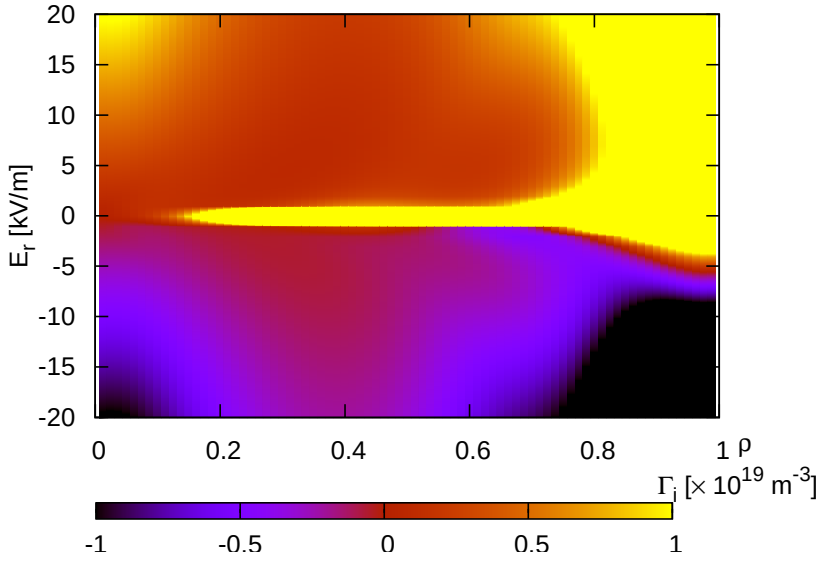

Figure 5.14: The E_r-Γ_i table calculated by DCOM/NNW for the plasma profile of LHD discharge #32940 $t = 2.5$ sec.

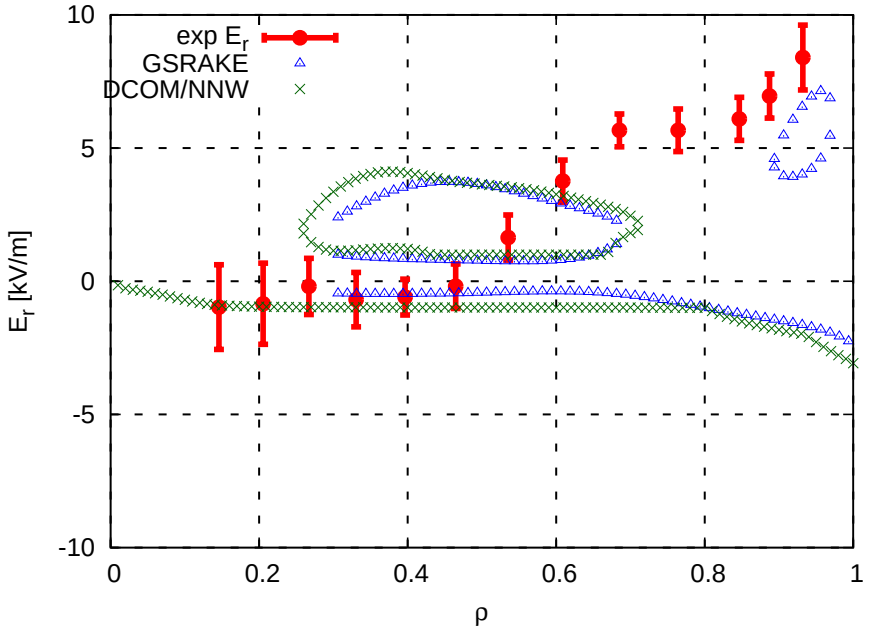

Figure 5.15: The steady-state ambipolar E_r obtained by GSRAKE, DCOM/NNW, and experimental observations.

done in the Section 5.3.2. The Γ_i-E_r data base used in this simulation is shown in Fig. 5.14. Also in this case, a clear peaked Γ_i appears as in the case of CERC plasma in Fig. 5.7. Other calculation conditions such as the number of employed particles, the number of Fourier spectrum, and the time step are the same as those in the previous subsection. It is noticed that a non-CERC plasma with the lower temperature and the smaller T_e gradient is expected to result in almost the same resultant E_r since electron non-local drift effect does not affect so much neoclassical transport in this parameter regime.

Results of the ambipolar E_r by GSRAKE and DCOM/NNW are shown in Fig. 5.15. In the inner region of $\rho < 0.5$, the ion-root E_r observed in the experiment is reproduced by both GSRAKE and DCOM/NNW. On the other hand, in the edge region of $\rho > 0.7$, DCOM/NNW results in only the ion-root E_r while GSRAKE has multiple roots at this region.

The ambipolar E_r obtained by FORTEC-3D is shown in Fig. 5.16. It is noted that the value is averaged over 0.4 τ_ei. Dashed line denotes the initial E_r profile used in this simulation. Only the ion-root E_r is obtained by FORTEC-3D over the whole plasma region, while DCOM/NNW results in the multiple roots at $0.3 < \rho < 0.7$. Although the ambipolar E_r does not agree with the electron-root E_r observed at $\rho > 0.6$, it

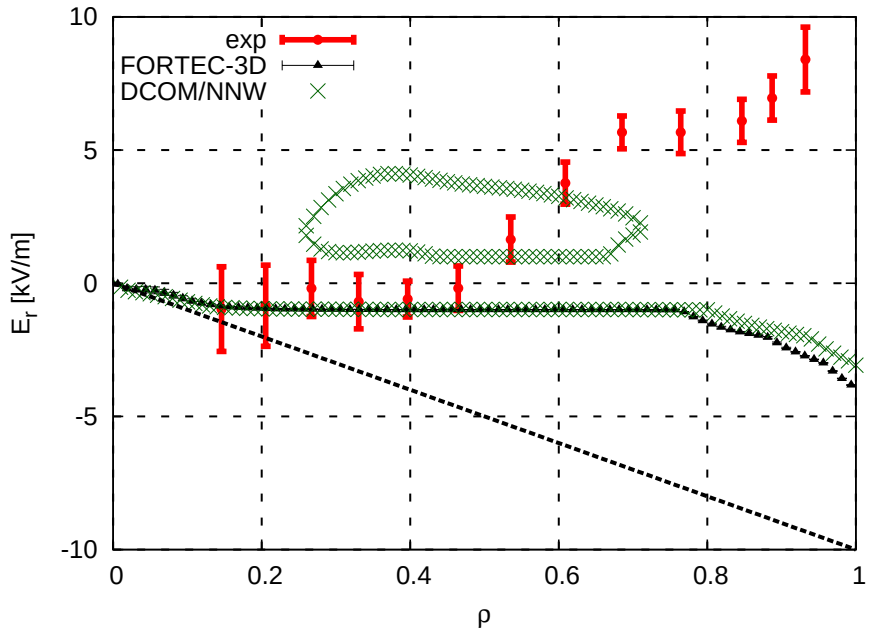

Figure 5.16: The steady-state ambipolar E_r obtained by FORTEC-3D, DCOM/NNW, and experimental observations are shown, respectively. Also shown by the dashed line is the initial profile of E_r used in the FORTEC-3D simulation.

agrees well with the DCOM/NNW results as expected. Thus we can conclude that the ambipolar E_r for a non-CERC plasma with the low electron temperature results in almost the same radial electric field as that obtained by the local numerical code.

5.4 Summary and discussion

5.4.1 Radial electric field diffusion

In this subsection, we discuss on the diffusivity on the radial electric field. It is beneficial to find a way to improve the numerical increase which observed at the interface in the steady-state E_r profile calculated by FORTEC-3D simulation.

FORTEC-3D only involves a numerical diffusion on the radial electric field and does not have any other physical diffusion terms. The diffusion term arises from the radial interpolation of the particle flux in FORTEC-3D which is performed in solving the time evolution of the radial electric field of Eq.5.3 [46]. This is accounted for as follows. FORTEC-3D calculates the particle flux at a radial position. Then, the particle flux at a different radial position by a half mesh size is interpolated from the particle flux

obtained above as the volume-averaged value. The time evolution of the radial electric field is solved with the interpolated volume-averaged particle flux at the radial position of the half mesh size. The interpolation procedure involves the numerical diffusion for the radial electric field and it stabilizes the result of the resultant radial electric field. It has been shown in the previous simulations for ions using FORTEC-3D that this numerical diffusion enables ones to calculate the ion particle flux and to obtain the stable radial electric field properly over the whole plasma region.

For electrons, however, E_{r} for case (1) rapidly increases at $\rho \simeq 0.75$ as shown in Fig. 5.11(a). The same rapid increase in E_{r} occurs for case (2) (see Fig. 5.11(b)). It poses a new problem for calculations of the electron particle flux and the radial electric field. A possible approach to solve the problem is to introduce an additional diffusivity on the radial electric field.

Some authors insist that the diffusive term, or the electric field diffusivity is necessary to solve the time evolution of the radial electric field including the bifurcation of the radial electric field [74, 75]. Introducing the electric field diffusivity modifies Eq.(5.3) as follows,

$$\epsilon_0 \epsilon_\perp \frac{\partial E_{\mathrm{r}}}{\partial t} = -e\left(\Gamma_{\mathrm{i}} - \Gamma_{\mathrm{e}}\right) + \frac{1}{r}\frac{\partial}{\partial r}\left(r D_{\mathrm{E}} \frac{\partial E_{\mathrm{r}}}{\partial r}\right), \tag{5.4}$$

where D_{E} denotes the electric field diffusivity. The diffusivity on the radial electric field works well to smoothly connect the interface region between the electron-root E_{r} in the core region and the ion-root one in the edge. It is considered as a possible reason that the omission of the diffusivity on E_{r} result in numerical divergence at the interface. The analytic estimation shows that that the width of the interface layer which connects electron root and ion root is proportional to $\sqrt{D_{\mathrm{E}}}$ [64], the inclusion of the diffusivity term D_{E} may improve the numerical increase in E_{r} at the interface. The time evolution of E_{r} introducing the diffusive term D_{E} will be performed in future work.

5.4.2 Maxwell's construction

Maxwell's construction is originally known in the thermal dynamics as the means to determine the phase boundary, or the critical point in the phase equilibrium state. Then Itoh, *et al.*, have pointed out that the position of the interface, or the boundary of the E_{r} bifurcation from electron (ion) root to ion (electron) root, is determined according to Maxwell's construction as in the thermal dynamics [64]. At the interface,

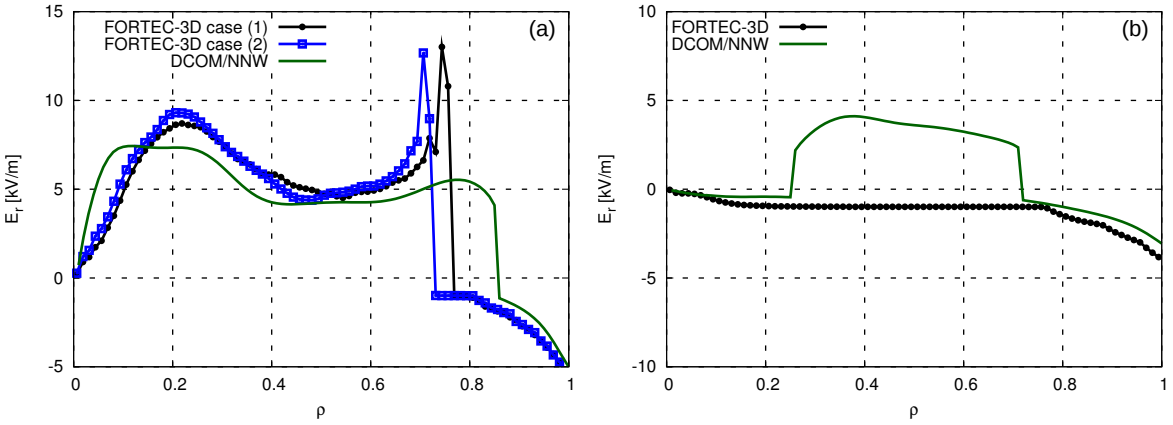

Figure 5.17: The ambipolar E_r determined by Maxwell's construction for the plasma of Figs. 5.2 ((a) CERC plasma) and 5.13 ((b) non-CERC plasma).

the radial electric field and the particle flux should satisfy the relation below;

$$\Delta\Phi(\rho) \equiv \int_{E_\mathrm{r}^\mathrm{i}}^{E_\mathrm{r}^\mathrm{e}} e\left(\Gamma_\mathrm{i}(\rho, E_\mathrm{r}) - \Gamma_\mathrm{e}(\rho, E_\mathrm{r})\right) dE_\mathrm{r} = 0, \tag{5.5}$$

where, E_r^i and E_r^e are the ion-root E_r and electron-root E_r, respectively. The integrand in Eq.(5.5) corresponds to the radial current and vanishes at the boundary of this integration.

The ambipolar E_r determined in this way for DCOM/NNW is shown in Fig. 5.17 with FORTEC-3D results. It is shown in the figure (a) that the position of the interface of the DCOM/NNW result locates outward than evaluated by FORTEC-3D simulations of case (1) and case (2) for the case of a CERC plasma. It seems to be natural of the interface position to be different between FORTEC-3D and DCOM/NNW since the particle flux of each code differs from each other due to the finite orbit width effect of the electron. This suggest that the position of the interface needs to be examined including the effect of the electron drift in addition to Maxwell's construction which involves the thermodynamically stable state of E_r in neoclassical transport theory since it is clearly affected by the dynamics of electrons which is not accurately included in DCOM/NNW. It is also noted that the position of the interface slightly changes depending on the initial profile of E_r. One can see in Fig. 5.17 (b) that while E_r bifurcation is expected in DCOM/NNW with Maxwell's construction, no such phenomenon is obtained by the FORTEC-3D simulation for a non-CERC plasma. It is considered that since the initial E_r profile is set to be ion root over the whole plasma region (see Fig. 5.16), the resultant E_r is determined according to the local minimum point located in the ion-root E_r which satisfies $\Gamma_\mathrm{e} = \Gamma_\mathrm{i}$.

Now we can calculate the radial electric field rigorously using FORTEC-3D, Maxwell's construction and its relation to the bifurcation phenomenon of the radial electric field is to be studied with the numerical simulation. The initial value dependence and the FOW effect on the interface position will be also investigated in the future work.

5.4.3 Summary

The radial electric field for CERC and non-CERC plasmas obtained in LHD is analyzed by FORTEC-3D. To investigate the ambipolar E_r expected in neoclassical transport theory with taking electron FOW effect into account, we implement the two different kinds of simulations as follows; (1) The electron particle flux is calculated by FORTEC-3D with the *temporally-fixed* E_r as is done in the Chapter 4, then estimate the ambipolar E_r which satisfies $\Gamma_e = \Gamma_i$. (2) The time-dependent radial electric field is simultaneously calculated with the electron particle flux as the steady-state solution with referring to a Γ_i data base from DCOM/NNW results. It is emphasized that this is the first time to investigate the radial electric field of a CERC plasma including the finite orbit width effect of electrons. One can obtain the neoclassical ambipolar E_r by FORTEC-3D with less assumptions compared to the local neoclassical calculations.

The steady state analysis of the ambipolar E_r for a CERC plasma shows that the resultant E_r is not affected so much by the electron drift effect although the electron particle flux is changed by the effect. This is understood as follows; the electron-root E_r has such large value that the the effect of the electron orbit on the electron neoclassical transport comes to be negligibly small compared to the large $\boldsymbol{E} \times \boldsymbol{B}$ drift. On the other hand, the ion-root and unstable-root E_r is located around $E_r = 0$ where a strong peak of Γ_i appears. The ion-root and unstable-root E_r, or the intersection of Γ_e and Γ_i is determined in accordance with the foot-point of Γ_i both for Γ_e of FORTEC-3D and that of DCOM/NNW due to the preponderance of the ion particle flux in the ambipolar condition.

Next, the radial electric field is obtained as the steady-state solution of time evolution of E_r. As a result, the difference of the particle flux and the radial electric field between FORTEC-3D and DCOM/NNW becomes large in the core region. It suggests that it is necessary to evaluate the neoclassical transport flux and the ambipolar E_r formation with the FOW effect of electrons since the principal difference between these codes is the additional FOW effect in FORTEC-3D. It has been found that the finite orbit width effect in tokamaks either reduce or increase neoclassical heat flux near the

magnetic axis depending on the plasma temperature profile [47]. In LHD, the finite orbit width effect is more complicated due to the features of the strong dependence on E_r and the particle orbit such as the collisionless detrapping as shown in Chapter 4, which are not seen in tokamak cases. Since it is difficult to treat such problems analytically, the direct simulation of the particle flux and the radial electric field with FOW effect taken into account is useful. The ion-root E_r is obtained by FORTEC-3D in the edge region as that by DCOM/NNW, which is in contrast to the experimental observation. More detailed analyses on the difference between the ambipolar radial electric field and the experimental observation will be carried out in the future.

Chapter 6

Conclusions

In this thesis, we focus on the neoclassical transport including the electron finite orbit width effect in high-temperature helical plasmas. The electron finite orbit width effect has been conventionally neglected in the local, or conventional neoclassical transport theory and/or calculation since the effect involves the radial deviation of electrons from a certain magnetic surface and the deviation is considered to be small enough compared to the plasma scale length. It is noted that the ∇B and the curvature drift of a particle is generally neglected in the local neoclassical theory for the consistency with the small radial drift. Although the finite orbit width effect for ion has been intensively and widely investigated in recent years, the assumption of the small finite orbit width effect of electron has been justified due to the small mass ratio, $\sqrt{m_{\mathrm{e}}/m_{\mathrm{i}}} \ll 1$. However, the effect comes to influence the neoclassical transport calculations as the electron temperature increases. This is caused by the large radial drift which the helically-trapped electrons have. We have explored directly the electron finite orbit width effect on neoclassical transport in the high electron temperature plasma by applying the Monte-Carlo based simulation code, FORTEC-3D to the electron species. It has been demonstrated that the finite orbit width effect qualitatively change the electron neoclassical particle and energy flux. The radial electric field (E_{r}) has been also evaluated by FORTEC-3D. It has been shown that the electron finite orbit width effect has made the radial electric field different from that by the local calculation especially in the core region. This is the first time to examine the radial electric field formation in the experimental plasma with the electron finite orbit width taken into account. It is emphasized that the direct numerical calculation of the neoclassical flux and the radial electric field with less assumptions is useful to investigate the finite orbit width effect in helical plasmas since it is too complicated to be treated analytically.

At first, we have studied the neoclassical transport property in high T_i plasmas obtained in LHD experiments. Neoclassical transport is caused by the collisions in plasmas and thus it is an inevitable minimum transport for torus plasmas. In helical plasmas, it increases in proportion to $1/\nu$ due to the presence of ripple-trapped particles, where ν is the collision frequency. To investigate the ambipolar radial electric field and the resultant neoclassical particle and energy flux in high T_i plasmas, the numerical neoclassical transport calculation code, GSRAKE, which solves the ripple-averaged drift kinetic equation based on the local assumptions, has been used.

It has been found that the weak negative, or the ion-root radial electric field exists in high T_i plasmas in which T_e is generally smaller than T_i. Then, we have explored the improved confinement for such high T_i plasmas varying the ion and electron temperature and density numerically. It has been aimed to investigate more favorable parameter from the viewpoint of reducing the neoclassical transport. These parameter survey calculations have showed that either the electron-root (large positive value) or multiple-root E_r is expected to exist even in the parameter regime of $T_\mathrm{i} \simeq T_\mathrm{e} \sim 10$ keV if $T_\mathrm{i} \simeq T_\mathrm{e}$ is numerically assumed. Since the electron-root E_r generally reduces the neoclassical transport particle and energy flux more effectively due to the large value of $|E_\mathrm{r}|$, the feature of the existence of the electron-root E_r in high T_i plasmas has the advantage to accomplish the improved confinement in LHD plasmas. Indeed, it has been demonstrated that the electron-root radial electric field reduces the neoclassical energy flux in high T_i plasmas. This has showed that the high electron temperature in an artificial concurrent combination with the high ion temperature would be preferable for the improved confinement in LHD; the electron-root scenario has been proposed.

Then, the favorable character of the high electron temperature has led us to reconsider the neoclassical transport in a high electron temperature helical plasma. An effort to achieve high T_e plasmas has been intensively made in LHD experiments and also in other helical devices. For example, the Core Electron-Root Confinement (CERC) plasma have been observed in many helical devices. This plasma is characterized by the high electron temperature and the steep T_e gradient in the core region called electron internal transport barrier (eITB). An transitional behavior of the radial electric field from the ion-root E_r to the electron-root E_r is observed experimentally in the CERC plasma.

The deviation from a magnetic surface of helically-trapped particles, Δh, is estimated as $\Delta h \propto T/\nu$. Thus, it increases as the electron temperature (the collisionality) increases (decreases). On the other hand, the plasma scale length of the CERC plasma

decreases because of the steep T_e gradient. This suggests that the local assumptions of the small radial drift of electrons may be inappropriate in the CERC plasma due to the feature of the high electron temperature and the steep T_e gradient. Thus, it is required to calculate the electron neoclassical transport more rigorously including the electron finite orbit width effect. We have investigated the electron finite orbit width effect on neoclassical transport calculations in this thesis. Main purposes and achievements of this thesis are as follows.

- It is demonstrated directly by the numerical calculation that the finite orbit width effect of electrons influences on the electron neoclassical transport. FORTEC-3D is extended to investigate the effect. The electron neoclassical particle and energy flux become qualitatively different from those of the local neoclassical calculation due to the poloidal resonance and the collisionless detrapping.

- The ambipolar radial electric field for experimental plasmas is analyzed by the extended FORTEC-3D using the *ion* particle flux data base obtained DCOM/NNW. Two different approaches are adopted to obtain the ambipolar E_r; one is the steady-state calculation with the *temporally-fixed* radial electric field, and the other is to solve the time evolution of the radial electric field with the electron particle flux and obtain the radial electric field as its steady-state solution.

For the first purpose, we have extended the numerical code, FORTEC-3D, to be applicable to electrons. FORTEC-3D originally calculates the ion neoclassical transport with taking ion FOW effect into account based on δf Monte-Carlo method. Three types of calculations to illustrate the electron finite orbit width effect on the electron neoclassical transport have been performed.

First, the benchmark simulations of FORTEC-3D have been carried out for plasmas in the relatively high collisionality regime to validate and verify numerical results obtained by FORTEC-3D for electrons. The numerical parameter has been chosen as low T_e ($T_e = 1$ keV in the core) since it has been considered that the FOW effect contributes little to the neoclassical transport. It has been demonstrated that the neoclassical flux dependence on the radial electric field by FORTEC-3D has reproduced similar results as those obtained by GSRAKE and DCOM/NNW, in which the electron finite orbit width effect is not considered. This has indicated that the numerical results of FORTEC-3D have offered the appropriate value of the electron neoclassical transport in the relatively high collisionality regime.

Next, FORTEC-3D has been applied to plasmas in lower collisionality regime with (1) the low T_e and the low density, and (2) the high T_e and the low density to investigate the electron finite orbit width effect in the low collisionality regime. It is noted that these two cases have the similar collisionality and both are in the $1/\nu$ regime.

For the case (1), it has been confirmed that the numerical results of the neoclassical particle flux dependence on E_r have showed an reasonable agreement with that calculated by GSRAKE and DCOM/NNW except for $E_r = 0$. The difference around $E_r = 0$ is accounted for by the reduction of the neoclassical transport caused by the particle detrapping due to the finite orbit width effect in FORTEC-3D.

The further qualitative change in the electron neoclassical transport has arisen for the case (2). The peak position has shifted from the $E_r = 0$ in the local calculations to the positive E_r in the FORTEC-3D results involving the finite orbit width effect due to the difference of the poloidal resonance. In the local calculation the poloidal resonance condition is satisfied at $E_r = 0$ since it neglects the ∇B and the curvature drift. On the other hand, the non-local treatment of FORTEC-3D includes these drift, so that the poloidal resonance condition is determined by the balance between these drift and the $\boldsymbol{E} \times \boldsymbol{B}$ drift. As a result, the poloidal resonance occurs at the finite positive radial electric field and the peak of the electron neoclassical transport is seen there. By the numerical results of these two cases, we can conclude that the electron finite orbit width effect indeed plays an important role in a rigorous calculation of the electron neoclassical transport in high T_e and low collisionality plasmas.

For the second purpose, we have examined the radial electric field formation in a LHD CERC plasma by using the extended FORTEC-3D. The neoclassical ambipolar E_r is determined by the ambipolar condition of $\Gamma_e = \Gamma_i$ in steady state. To implement the simulation, we have extended FORTEC0-3D to refer to DCOM/NNW calculation results of $\Gamma_i = \Gamma_i(\rho, E_r)$ as a ion particle flux data base.

First, the steady state ambipolar E_r has been estimated by using the numerical results of FORTEC-3D for the temporally-fixed E_r. With this approach, it has been found that the electron finite orbit width effect has took little effect on the radial electric field formation, although the electron particle flux has been different from that of the local calculation. Then, FORTEC-3D simulations have been carried out to solve the time evolution of the radial electric field. The ambipolar E_r has been obtained as the steady-state solution and compared to those observed in the experiment and obtained by the local calculation. The resultant radial electric field and the electron neoclassical flux have showed the different profile from those obtained by DCOM/NNW

calculation especially in the core, $\rho < 0.3$. This has suggested that the electron finite orbit width effect has influenced on the radial electric field formation. In the edge region, the ion-root E_{r} has been obtained by both FORTEC-3D and DCOM/NNW although the electron-root E_{r} has been observed in the experiment.

As concluding remarks, it is worth pointing out the future direction of this thesis. Since FORTEC-3D involves the precise information of particle motions in the phase space, it enables one to examine the non-local effect on the neoclassical transport in more detail. For example, investigating the populations of helically-trapped and passing particles will be beneficial to understand the complicated behavior of particles in helical plasmas such as the particle trapping/detrapping and the poloidal resonance. In addition, the cause of the difference between the ambipolar E_{r} of FORTEC-3D and the experimental observations remains unclear and it needs to be elucidated. This will be examined in further practical applications of FORTEC-3D to experimental plasmas. The parallel flow and source terms of the heating and the particle are also of importance in more close conditions to experiments. Especially, the effect of ECH will be required to be included in the FORTEC-3D calculation for a more detailed analysis of CERC plasmas, since it plays a key role to achieve the CERC plasmas in LHD. Another interesting topic is concerned with an transitional phenomenon of the radial electric field in a CERC plasma. The mechanism of the E_{r} transition and the CERC formation remains one of the important issues in transport studies. FORTEC-3D will be used to investigate the role of the neoclassical ambipolar radial electric field in the CERC formation.

Appendix A

Calculation of the Second Adiabatic Invariant

In the bounce-averaged drift kinetic equation (2.44), the bounce-averaged drift velocities of the guiding center are required. The second adiabatic invariant is useful to calculate these drifts, and it is given as [2, 44],

$$J_{\mathrm{r}} = J_{\mathrm{r}}(r,\theta) \equiv \oint m v_{\parallel} d\zeta, \tag{A.1}$$

for helically-trapped particles, and

$$J_{\pm} = J_{\pm}(r,\theta) \equiv \int_{0}^{\pm 2\pi/N} m v_{\parallel} d\zeta, \tag{A.2}$$

for passing particles, where $v_{\parallel}$ is the parallel velocity of the guiding center, ζ denotes the toroidal angle, and N is the number of the helical pitch. It is important that the second adiabatic invariant is conserved for the particle bounce motion. It is noted that the particle is assumed to move mainly along the toroidal direction within one helical period due to the small rotational transform. The integral over ζ in Eq. (A.1) reflects this assumption. The second adiabatic invariant is the function of r and θ, thus it describes the drift surface in the poloidal plane.

To calculate the drift velocities for helically-trapped particles, we focus on the helically-trapped particles below. The magnetic field is assumed to be the same as that used in Sec. 2.3. The Equation (A.1) is rewritten as,

$$J_{\mathrm{r}} = \sqrt{2m} \oint \left[\mathcal{E} - e\Phi - \mu B_0 (1 - \epsilon_{\mathrm{t}} \cos\theta - \epsilon_{\mathrm{h}} \cos(l\theta - N\zeta))\right]^{1/2} d\zeta, \tag{A.3}$$

where $\mathcal{E}$ and Φ are the particle total energy and the potential, respectively, μ is the magnetic moment. To obtain J_{r} explicitly, it is convenient to define the pitch angle

parameter k^2 as,

$$k^2 \equiv \frac{\mathcal{E} - e\Phi - \mu B_0(1 + \epsilon_{\rm t}\cos\theta - \epsilon_{\rm h})}{2\mu B_0 \epsilon_{\rm h}}. \tag{A.4}$$

For helically-trapped particles, $0 < k^2 < 1$ is satisfied, while $1 < k^2$ is satisfied for passing particles.

Using $k^2 = k^2(r, \theta, \mathcal{E}, \mu)$, Eq. (A.3) becomes

$$\begin{aligned} J_{\rm r} &= \sqrt{2m\epsilon_{\rm h}\mu B_0} \oint \sqrt{2k^2 + \cos(l\theta - N\zeta) - 1} d\zeta \\ &= 2\sqrt{m\epsilon_{\rm h}\mu B_0} \int_{\zeta_-}^{\zeta_+} \sqrt{k^2 - \sin^2\left(\frac{l\theta - N\zeta}{2}\right)}, \end{aligned} \tag{A.5}$$

where ζ_- and ζ_+ represent the bounce point in ζ and satisfy the relation,

$$k^2 = \sin^2\left(\frac{l\theta - N\zeta_\pm}{2}\right). \tag{A.6}$$

A new variable X defined as

$$k\sin X = \sin\left(-\frac{l\theta - N\zeta}{2}\right) \tag{A.7}$$

is introduced instead of ζ, where $\zeta_\pm$ correspond to $\pm\pi/2$. Using the new variable, one can obtain following equation,

$$\begin{aligned} J_{\rm r} &= \frac{16}{N}\sqrt{m\epsilon_{\rm h}\mu B_0} \int_0^{\pi/2} \frac{k^2(1 - \sin^2 X)}{\sqrt{1 - k^2\sin^2 X}} dX \\ &= \frac{16}{N}\sqrt{m\epsilon_{\rm h}\mu B_0} \left[E(k) - (1 - k^2)K(k)\right], \end{aligned} \tag{A.8}$$

where $K(k)$ and $E(k)$ are the complete elliptic integral of the first and the second kind, respectively.

The drift velocities are easily obtained from the second adiabatic invariant, $J_{\rm r}$. The poloidal and radial drift velocities are given by the following relations,

$$\dot{\theta} = \frac{1}{eBr}\frac{\partial J/\partial r}{\partial J/\partial \mathcal{E}} \tag{A.9}$$

$$\dot{r} = -\frac{1}{eBr}\frac{\partial J/\partial \theta}{\partial J/\partial \mathcal{E}}. \tag{A.10}$$

As a result,

$$\dot{\theta} = \omega_{\rm t}\cos\theta + \omega_{\rm h} + \omega_{\rm E} \tag{A.11}$$

$$\dot{r} = r\omega_{\rm t}\sin\theta \tag{A.12}$$

are obtained, where

$$\omega_{\mathrm{t}} = \epsilon_{\mathrm{t}} \frac{\mu B_0}{eBr^2} \tag{A.13}$$

$$\omega_{\mathrm{h}} = \frac{\partial \epsilon_{\mathrm{h}}}{\partial r} \frac{\mu B_0}{eBr} \left(\frac{2E(k)}{K(k)} - 1 \right) \tag{A.14}$$

$$\omega_{\mathrm{E}} = -\frac{E_{\mathrm{r}}}{Br}, \tag{A.15}$$

are used. The first term on the right hand side of $\dot{\theta}$ and $\dot{r}$ denotes the drift caused by the toroidicity of the magnetic field line. The second term and the third term in Eq. (A.11) represent the drifts arising from the helicity and $\boldsymbol{E} \times \boldsymbol{B}$ drift, respectively.

Bibliography

[1] J. Wesson, *Tokamaks*, 3rd Edition, Oxford University Press, Oxford, 2004.

[2] M. Wakatani, *Stellarator and Heliotron Devices*, Oxford University Press, Oxford, 1998.

[3] A. Iiyoshi, A. Komori, A. Ejiri, M. Emoto, H. Funaba, M. Goto, K. Ida, H. Idei, S. Inagaki, S. Kado, O. Kaneko, K. Kawahata, T. Kobuchi, S. Kubo, R. Kumazawa, S. Masuzaki, T. Minami, J. Miyazawa, T. Morisaki, S. Morita, S. Murakami, S. Muto, T. Mutoh, Y. Nagayama, Y. Nakamura, H. Nakanishi, K. Narihara, K. Nishimura, N. Noda, S. Ohdachi, N. Ohyabu, Y. Oka, M. Osakabe, T. Ozaki, B. Peterson, A. Sagara, S. Sakakibara, R. Sakamoto, H. Sasao, M. Sasao, K. Sato, M. Sato, T. Seki, T. Shimozuma, M. Shoji, H. Suzuki, Y. Takeiri, K. Tanaka, K. Toi, T. Tokuzawa, K. Tsumori, K. Tsuzuki, K. Watanabe, T. Watari, H. Yamada, I. Yamada, S. Yamaguchi, M. Yokoyama, R. Akiyama, H. Chikaraishi, K. Haba, S. Hamaguchi, M. Iima, S. Imagawa, N. Inoue, K. Iwamoto, S. Kitagawa, J. Kodaira, Y. Kubota, R. Maekawa, T. Mito, T. Nagasaka, A. Nishimura, C. Takahashi, K. Takahata, Y. Takita, H. Tamura, T. Tsuzuki, S. Yamada, K. Yamauchi, N. Yanagi, H. Yonezu, Y. Hamada, K. Matsuoka, K. Murai, K. Ohkubo, I. Ohtake, M. Okamoto, S. Satoh, T. Satow, S. Sudo, S. Tanahashi, K. Yamazaki, M. Fujiwara, O. Motojima, Nuclear Fusion **39**, 1245–1256 (1999).

[4] R. Balescu, *Transport Processes in Plasmas vol.1 Classical Transport*, North-Holland, Amsterdam, 1988.

[5] F. Hinton, R. Hazeltine, Reviews of Modern Physics **48**, 239–308 (1976).

[6] S. Hirshman, D. Sigmar, Nuclear Fusion **21**, 1079–1201 (1981).

[7] R. Balescu, *Transport Processes in Plasmas vol.2 Neoclassical Transport*, North-Holland, Amsterdam, 1988.

[8] P. Helander, D. J. Sigmar, *Collisional Transport in Magnetized Plasmas*, Cambridge University Press, Cambridge, 2002.

[9] R. Balescu, *Aspects of Anomalous Transport in Plasmas*, IOP Publishing, Bristol, 2005.

[10] W. Horton, Reviews of Modern Physics **71**, 735–778 (1999).

[11] P. H. Rutherford, E. A. Frieman, Physics of Fluids **11**, 569 (1968).

[12] T. M. Antonsen, B. Lane, Physics of Fluids **23**, 1205 (1980).

[13] D. Biskamp, E. Schwarz, A. Zeiler, A. Celani, J. F. Drake, Physics of Plasmas **6**, 751 (1999).

[14] J. W. Connor, H. R. Wilson, Plasma Physics and Controlled Fusion **36**, 719–795 (1994).

[15] K. Ida, T. Shimozuma, H. Funaba, K. Narihara, S. Kubo, S. Murakami, A. Wakasa, M. Yokoyama, Y. Takeiri, K. Watanabe, K. Tanaka, M. Yoshinuma, Y. Liang, N. Ohyabu, Physical Review Letters **91**, 085003 (2003).

[16] K. C. Shaing, Physics of Fluids **26**, 3315 (1983).

[17] D. A. Spong, Physics of Plasmas **12**, 056114 (2005).

[18] P. Helander, a. Simakov, Physical Review Letters **101**, 1–4 (2008).

[19] K. Ida, M. Yoshinuma, M. Yokoyama, S. Inagaki, N. Tamura, B. Peterson, T. Morisaki, S. Masuzaki, A. Komori, Y. Nagayama, K. Tanaka, K. Narihara, K. Watanabe, C. Beidler, L. experimental Group, Nuclear Fusion **45**, 391–398 (2005).

[20] A. Galeev, R. Sagdeev, H. Furth, M. Rosenbluth, Physical Review Letters **22**, 511–514 (1969).

[21] A. A. Galeev, R. Z. Sagdeev, *Reviews of Plasma Physics vol.7*, p. 257, Consultants Bureau, New York, 1979.

[22] A. Fujisawa, A. Shimizu, H. Nakano, S. Ohsima, K. Itoh, H. Iguchi, Y. Yoshimura, T. Minami, K. Nagaoka, C. Takahashi, M. Kojima, S. Nishimura, M. Isobe, C. Suzuki, T. Akiyama, Y. Nagashima, K. Ida, K. Toi, T. Ido, S.-I. Itoh, K. Matsuoka, S. Okamura, P. H. Diamond, Plasma Physics and Controlled Fusion **48**, S205–S212 (2006).

[23] M. Yokoyama, H. Maaßberg, C. D. Beidler, V. Tribaldos, K. Ida, T. Estrada, F. Castejon, A. Fujisawa, T. Minami, T. Shimozuma, Y. Takeiri, A. Dinklage, S. Murakami, H. Yamada, Nuclear Fusion **47**, 1213–1219 (2007).

[24] Seikichi Matsuoka, Masayuki Yokoyama, Kenichi Nagaoka, Yasuhiko Takeiri, Mikiro Yoshinuma, Katsumi Ida, Tetsuo Seki, Hisamichi Funaba, Sadayoshi Murakami, Atsushi Fukuyama, Nobuyoshi Ohyabu, Osamu Kaneko, The LHD Experimental Group, Plasma and Fusion Research **3**, S1056 (2008).

[25] K. Ida, Plasma Physics and Controlled Fusion **40**, 1429–1488 (1998).

[26] H. Sugama, T. H. Watanabe, M. Nunami, S. Nishimura, Plasma Physics and Controlled Fusion **53**, 024004 (2011).

[27] M. Kikuchi, Nuclear Fusion **30**, 265–276 (1990).

[28] M. Kikuchi, M. Azumi, S. Tsuji, K. Tani, H. Kubo, Nuclear Fusion **30**, 343–355 (1990).

[29] K. Ida, H. Yamada, H. Iguchi, K. Itoh, Physical Review Letters **67**, 58–61 (1991).

[30] F. Wagner, G. Becker, K. Behringer, D. Campbell, A. Eberhagen, W. Engelhardt, G. Fussmann, O. Gehre, J. Gernhardt, G. Gierke, G. Haas, M. Huang, F. Karger, M. Keilhacker, O. Klüber, M. Kornherr, K. Lackner, G. Lisitano, G. Lister, H. Mayer, D. Meisel, E. Müller, H. Murmann, H. Niedermeyer, W. Poschenrieder, H. Rapp, H. Röhr, F. Schneider, G. Siller, E. Speth, A. Stäbler, K. Steuer, G. Venus, O. Vollmer, Z. Yü, Physical Review Letters **49**, 1408–1412 (1982).

[31] S.-I. Itoh, K. Itoh, Nuclear Fusion **29**, 1031–1045 (1989).

[32] K. Shaing, Physical Review Letters **63**, 2369 – 2372 (1989).

[33] H. E. Mynick, A. H. Boozer, Physics of Plasmas **14**, 072507 (2007).

[34] H. Sugama, T.-H. Watanabe, Physics of Plasmas **16**, 056101 (2009).

[35] M. Yokoyama, H. Maaßberg, C. D. Beidler, V. Tribaldos, K. Ida, F. Castejon, T. Estrada, A. Fujisawa, T. Minami, T. Shimozuma, J. Herranz, S. Murakami, H. Yamada, Fusion Science and Technology **50**, 327–342 (2006).

[36] H. Takahashi, T. Shimozuma, S. Kubo, I. Yamada, S. Muto, M. Yokoyama, H. Tsuchiya, T. Ido, A. Shimizu, C. Suzuki, K. Ida, S. Matsuoka, S. Satake, K. Narihara, N. Tamura, Y. Yoshimura, H. Igami, H. Kasahara, Y. Tatematsu, T. Mutoh, T. L. E. Group, High Te, low collisional plasma confinement characteristics in LHD, in: IAEA Fusion Energy Conference 2010, pp. EXC/P8–15, Daejon, Korea (2010).

[37] H. Idei, K. Ida, H. Sanuki, H. Yamada, H. Iguchi, S. Kubo, R. Akiyama, H. Arimoto, M. Fujiwara, M. Hosokawa, K. Matsuoka, S. Morita, K. Nishimura, K. Ohkubo, S. Okamura, S. Sakakibara, C. Takahashi, Y. Takita, K. Tsumori, I. Yamada, Physical Review Letters **71**, 2220–2223 (1993).

[38] S. Toda, K. Itoh, Plasma Physics and Controlled Fusion **44**, 325–333 (2002).

[39] K. Itoh, S. Toda, A. Fujisawa, S.-I. Itoh, M. Yagi, A. Fukuyama, P. H. Diamond, K. Ida, Physics of Plasmas **14**, 020702 (2007).

[40] S. P. Hirshman, K. C. Shaing, W. I. van Rij, C. O. Beasley, E. C. Crume, Physics of Fluids **29**, 2951 (1986).

[41] W. I. van Rij, S. P. Hirshman, Physics of Fluids B: Plasma Physics **1**, 563 (1989).

[42] A. Wakasa, S. Murakami, M. Itagaki, S.-i. Oikawa, Japanese Journal of Applied Physics **46**, 1157–1167 (2007).

[43] A. Wakasa, S. Murakami, S.-i. Oikawa, Plasma and Fusion Research **3**, S1030–S1030 (2008).

[44] K. Miyamoto, *Plasma Physics for Nuclear Fusion*, MIT Press, Cambridge, 1980.

[45] S. Satake, M. Okamoto, N. Nakajima, H. Sugama, M. Yokoyama, Plasma and Fusion Research **1**, 002 (2006).

[46] S. Satake, R. Kanno, H. Sugama, Plasma and Fusion Research **3**, S1062–S1062 (2008).

[47] W. X. Wang, G. Rewoldt, W. M. Tang, F. L. Hinton, J. Manickam, L. E. Zakharov, R. B. White, S. Kaye, Physics of Plasmas **13**, 082501 (2006).

[48] R. A. Kolesnikov, W. X. Wang, F. L. Hinton, G. Rewoldt, W. M. Tang, Plasma Physics and Controlled Fusion **52**, 042002 (2010).

[49] S. Brunner, E. Valeo, J. A. Krommes, Physics of Plasmas **6**, 4504 (1999).

[50] W. Wang, N. Nakajima, M. Okamoto, S. Murakami, Journal of Plasma Fusion Research SERIES **2**, 250–254 (1999).

[51] C. D. Beidler, W. D. D'haeseleer, Plasma Physics and Controlled Fusion **37**, 463 (1995).

[52] C. D. Beidler, H. Maaßberg, Plasma Physics and Controlled **43**, 1131 (2001).

[53] R. D. Hazeltine, J. D. Meiss, *Plasmas Confinement*, Dover Publications, New York, 2003.

[54] A. H. Boozer, Physics of Fluids **24**, 1999 (1981).

[55] A. H. Boozer, Physics of Fluids **23**, 904 (1980).

[56] R. G. Littlejohn, Physics of Fluids **24**, 1730 (1981).

[57] R. G. Littlejohn, Journal of Plasma Physics **29**, 111–125 (1983).

[58] R. B. White, Physics of Fluids B: Plasma Physics **2**, 845 (1990).

[59] J. R. Cary, C. L. Hedrick, J. S. Tolliver, Physics of Fluids **31**, 1586 (1988).

[60] S. Satake, M. Okamoto, H. Sugama, Physics of Plasmas **9**, 3946 (2002).

[61] H. E. Mynick, Physics of Fluids **26**, 2609 (1983).

[62] K. C. Shaing, S. A. Hokin, Physics of Fluids **26**, 2136 (1983).

[63] L. Kovrizhnykh, Nuclear Fusion **24**, 851–936 (1984).

[64] K. Itoh, S.-I. Itoh, A. Fukuyama, *Transport and Structural Formation in Plasmas*, Institute of Physics Publishing, Bristol, 1999.

[65] K. Nagaoka, M. Yokoyama, Y. Takeiri, K. Ida, M. Yoshinuma, S. Matsuoka, H. Funaba, S. Morita, T. Mutoh, T. Seki, K. Ikeda, M. Osakabe, K. Tsumori, Y. Oka, O. Kaneko, The LHD Experimental Group, Plasma and Fusion Research **3**, S1013 (2008).

[66] M. Yokoyama, A. Wakasa, S. Murakami, K.-Y. Watanabe, S. Satake, S. Nishimura, H. Sugama, N. Nakajima, H. Funaba, Y. Nakamura, Fusion Science and Technology **58**, 269 (2010).

[67] J W Connor, Plasma Physics and Controlled Fusion **30**, 619 (1988).

[68] M. Yokoyama, K. Watanabe, Nuclear Fusion **45**, 1600–1607 (2005).

[69] Z. Lin, W. M. Tang, W. W. Lee, Physics of Plasmas **2**, 2975 (1995).

[70] A. H. Boozer, G. Kuo-Petravic, Physics of Fluids **24**, 851 (1981).

[71] S. Murakami, A. Wakasa, H. Maaßberg, C. Beidler, H. Yamada, K. Watanabe, L. E. Group, Nuclear Fusion **42**, L19–L22 (2002).

[72] S. P. Hirshman, O. Betancourt, Journal of Computational Physics **96**, 99–109 (1991).

[73] S. Satake, H. Sugama, T.-H. Watanabe, Nuclear Fusion **47**, 1258–1264 (2007).

[74] D. E. Hastings, Physics of Fluids **28**, 334 (1985).

[75] S. Toda, K. Itoh, Plasma Physics and Controlled Fusion **43**, 629 (2001).

List of Publication

- S. Matsuoka, S. Satake, M. Yokoyama, and A. Wakasa, *"Radial Electric Field Formation Including Electron Radial Drift for a Core Electron Confinement (CERC) Plasma in LHD"*, Plasma Fusion Res. **6**, 016 (2011)
- S. Matsuoka, S. Satake, M. Yokoyama, A. Wakasa, and S. Murakami, *"Neoclassical electron transport calculation by using δf Monte Carlo method "*, Physics of Plasmas **18**, 032511 (2011)
- S. Matsuoka, M. Yokoyama, K. Nagaoka, Y. Takeiri, M. Yoshinuma, K. Ida, T. Seki, H. Funaba, S. Murakami, A. Fukuyama, N. Ohyabu, O. Kaneko and the LHD Experimental Group, *"Neoclassical Transport Properties in High-Ion-Temperature Hydrogen Plasmas in the Large Helical Device (LHD) "*, Plasma Fusion Res. **3**, S1056 (2008)

List of Presentation

- S. Matsuoka, S. Satake, and M. Yokoyama, *"Effect of Electron Drift Orbit on Transport in Helical Plasmas"*, 66th Annual Meeting of Japan Physical Society (cancelled), Niigata Univ., Niigata, Japan, 25 - 28 March, 2011, 25pGW-2 (oral presentation)

- S. Matsuoka, S. Satake, M. Yokoyama, and A. Wakasa, *"Effects of electron drift orbit on neoclassical transport in Helical Plasmas"*, Kyoto Terrsa, Kyoto, Japan, 16th Numerical Experiment Tokamak Workshop, 14 - 15 March, 2010 (oral presentation)

- S. Matsuoka, S. Satake, M. Yokoyama, and A. Wakasa, *"Neoclassical Transport Calculation for High Electron Temperature Plasmas in LHD by δf Monte Carlo Method"*, 20th International Toki Conference, Ceratopia Toki, Toki, Japan, 7 - 10 December, 2010, P1-34 (poster presentation)

- S. Matsuoka, S. Satake, M. Yokoyama, A. Wakasa, and S. Murakami, *"Calculation of the Electron Neoclassical Transport by Using the δf Monte Carlo Method"*, Autumn Meeting of Japan Physical Society 2010, Osaka Prefecture Univ., Sakai, Japan, 23 -26 September, 2010, 24aQJ-8 (oral presentation)

- S. Matsuoka, S. Satake, M. Yokoyama, A. Wakasa and S. Murakami, *"Non-local Simulation for Electrons Neoclassical Transport by Using δf Monte Carlo Method"*, 4th Simulation Science Symposium, NIFS, Toki, Japan, 14 - 15 September, 2010, P-15 (poster presentation)

- S. Matsuoka, S. Satake, M. Yokoyama, and, A. Wakasa, *"Calculation of Electron Neoclassical Transport by Using Monte Carlo δf method"*, 8th Joint Conference for Nuclear Fusion Energy, Takayama Public Cultural Hall, Takayama, Japan, 10 - 11 June, 2010, 11B-31p (poster presentation)

- S. Matsuoka, S. Satake, M. Yokoyama, and A. Wakasa, *"Neoclassical Transport Calculation for Electrons by Using δf Monte Carlo Method"*, Kyodai-Kaikan, Kyoto, Japan, 15th Numerical Experiment Tokamak Workshop, 17 - 19 March, 2010, P-3 (poster presentation)

- S. Matsuoka, M. Yokoyama, H. Funaba, K. Ida, K. Nagaoka, H. Takahashi, T. Shimozuma, R. Sakamoto, N. Ohyabu, the LHD Experimental Group, *"Comprehensive Understandings on the Effects of Radial Electric Field on the Reduction of Neoclassical Diffusion in Improved Confinement in LHD"*, 17th International Stellarator/Heliotron Workshop 2009, Princeton Plasma Physics Laboratory, Princeton, USA, 12 - 16 October, 2009, P02-19 (poster presentation)

- S. Matsuoka, M. Yokoyama, K. Nagaoka, Y. Takeiri, M. Yoshinuma, K. Ida, H. Funaba, S. Murakami, A. Fukuyama, N. Ohyabu, O. Kaneko, and the LHD experimental Group, *"Neoclassical Transport Properties in High-Ion-Temperature Hydrogen Plasmas in the Large Helical Device (LHD)"*, 24th Annual Meeting of JSPF, Eglet Himeji, Himeji, Japan, 27 - 30 November, 2007, 27pB19P (poster presentation)

- S. Matsuoka, M. Yokoyama, K. Nagaoka, Y. Takeiri, M. Yoshinuma, K. Ida, T. Seki, H. Funaba, S. Murakami, A. Fukuyama, N. Ohyabu, O. Kaneko, and the LHD Experimental Group, *"Neoclassical Transport Properties in High-Ion-Temperature Plasmas in the Large Helical Devices (LHD)"*, 17th International Toki Conference and 16th International Stellarator/Heliotron Workshop 2007, Ceratopia Toki, Toki, Japan, 15 -19 October, 2007, P2-013 (poster presentation)